Quantitative bacterial physiology under antibiotic and protein-overexpression stress



-Inaugural-Dissertation-

zur Erlangung des Doktorgrades (Dr. rer. nat.)
der Mathematisch-Naturwissenschaftlichen Fakultät
der Universität zu Köln

vorgelegt von

Natawan Gadjisade

Köln 2026

Von der genannten Fakultät als Dissertation angenommen.
Jahr der Disputation: 2026

Abstract

Antibiotics inhibit bacterial growth by targeting essential cellular processes. Combining antibiotics can improve treatment and limit the emergence of resistance, but their combined effects are difficult to predict. Understanding these responses requires a quantitative description of bacterial physiology under antibiotic treatment and changing environments. Bacterial growth laws and resource-allocation models provide such frameworks by linking growth rate to resource allocation.

I examined to what extent these frameworks can explain the response of *Escherichia coli* across different perturbations and physiological states using quantitative proteomics, growth measurements, fluorescent reporters and mathematical models.

Whole-proteome measurements revealed distinct resource-allocation responses to different antibiotics. Translation inhibitors had different effects on ribosome abundance, while the transcription inhibitor rifampicin decreased ribosome abundance and increased RNA polymerase abundance. Incorporating these responses into the model helped clarify why combinations of transcription and translation inhibitors showed different interactions. Nutrient conditions altered single-drug susceptibility, while most interactions between translation inhibitors remained stable. The growth-law framework captured the direction but not the magnitude of susceptibility changes across nutrient conditions. During a glucose–lactose diauxic shift, promoter-reporter measurements reproduced some of the strongest changes observed by proteomics, but agreement across the full dataset was only moderate. The reporter measurements did not provide a direct quantitative measure of protein abundance. Protein overexpression revealed an additional constraint for membrane proteins, as the displacement of endogenous membrane proteins was linked to a strong growth defect.

Together, these results show that growth laws and resource-allocation models capture important patterns in bacterial growth, but their predictive power depends on the type of perturbation and the physiological state of the cell. Deviations from these patterns can reveal constraints not captured by simple models.

Zusammenfassung

Antibiotika hemmen bakterielles Wachstum, indem sie essenzielle zelluläre Prozesse angreifen. Die Kombination von Antibiotika kann die Behandlung verbessern und die Entstehung von Resistenzen begrenzen. Ihre kombinierten Wirkungen sind jedoch schwer vorherzusagen. Das Verständnis dieser Wechselwirkungen erfordert eine quantitative Beschreibung der bakteriellen Physiologie unter Antibiotikabehandlungen und veränderten Umweltbedingungen. Bakterielle Wachstumsgesetze und Modelle der Ressourcenallokation bieten geeignete Konzepte, indem sie Wachstumsrate und Ressourcenallokation verknüpfen.

Ich untersuchte, inwieweit diese Konzepte die Reaktion von *Escherichia coli* auf verschiedene Perturbationen und unterschiedliche physiologische Zustände erklären können. Hierfür verwendete ich quantitative Proteomik, Wachstumsmessungen, fluoreszierende Reporter und mathematische Modelle.

Messungen des gesamten Proteoms zeigten unterschiedliche Muster der Ressourcenallokation unter verschiedenen Antibiotika. Translationsinhibitoren hatten unterschiedliche Auswirkungen auf die Ribosomenabundanz, während der Transkriptionsinhibitor Rifampicin die Ribosomenabundanz verringerte und die Abundanz der RNA-Polymerase erhöhte. Die Einbeziehung dieser Muster in das Modell half zu erklären, warum Kombinationen aus Transkriptions- und Translationsinhibitoren unterschiedliche Wechselwirkungen zeigten. Die Nährstoffbedingungen veränderten die Empfindlichkeit gegenüber einzelnen Antibiotika, während die meisten Wechselwirkungen zwischen Translationsinhibitoren stabil blieben. Das auf Wachstumsgesetzen basierende Modell erfasste die Richtung, jedoch nicht das Ausmaß der Veränderungen der Empfindlichkeit zwischen den Nährstoffbedingungen. Während des diauxischen Wechsels von Glukose zu Laktose stimmten die Messungen mit Promotor-Reportern bei einigen der stärksten Veränderungen mit den Proteomikdaten überein. Die Übereinstimmung im gesamten Datensatz war jedoch nur moderat. Die Reportermessungen lieferten daher kein direktes quantitatives Maß für die Proteinabundanz. Die Proteinüberexpression zeigte eine zusätzliche Einschränkung für Membranproteine, da die Verdrängung endogener Membranproteine mit einem starken Wachstumsdefekt verbunden war.

Zusammen zeigen diese Ergebnisse, dass Wachstumsgesetze und Modelle der Ressourcenallokation wichtige Muster des bakteriellen Wachstums erfassen, deren Vorhersagekraft jedoch von der Art der Perturbation und dem physiologischen Zustand der Zelle abhängt. Abweichungen von diesen Mustern können auf zusätzliche Einschränkungen hinweisen, die von einfachen Modellen nicht erfasst werden.

Abbreviations

BAM	β-barrel assembly machinery
BIC	bicyclomycin
CHL	chloramphenicol
CRY	capreomycin
DNA	deoxyribonucleic acid
DOX	doxycycline
E. coli	*Escherichia coli*
EF	elongation factor
EF-G	elongation factor G
EF-Tu	elongation factor thermo-unstable
ERM	erythromycin
FUS	fusidic acid
GFP	green fluorescent protein
GLU	M9 glucose
GLUAA	M9 glucose supplemented with amino acids
IC_{50}	half-maximal inhibitory concentration
IPTG	isopropyl β-D-thiogalactoside
KSG	kasugamycin
LB	lysogeny broth
LCY	lincomycin
LI	Loewe interaction score
MAN	M9 mannose

MANAA	M9 mannose supplemented with amino acids
mRNA	messenger RNA
OD	optical density
ppGpp	guanosine tetraphosphate
pppGpp	guanosine pentaphosphate
PTC	peptidyl-transferase center
RIF	rifampicin
RNA	ribonucleic acid
RNAP	RNA polymerase
rRNA	ribosomal RNA
SRP	signal recognition particle
STR	streptomycin
TET	tetracycline
tRNA	transfer RNA

Contents

Abbreviations IV

1 Introduction 1

1.1 Balanced exponential growth . . . 2

1.2 Gene expression . . . 4

1.2.1 Transcription . . . 4

1.2.2 Translation . . . 7

1.2.3 Stringent response . . . 9

1.2.4 Coupling of transcription and translation . . . 9

1.3 Post-translational processing and membrane proteins . . . 10

1.4 Growth inhibition . . . 13

1.4.1 Transcription and translation inhibitors . . . 13

1.4.2 Drug combinations . . . 16

1.5 Resource allocation . . . 18

1.5.1 Growth laws and ribosome allocation . . . 19

1.5.2 Flux-balance model . . . 20

1.5.3 Molecular interpretation of translational capacity . . . 22

1.6 Growth law-based models of antibiotic action . . . 25

1.6.1 Mechanistic model of translation inhibition . . . 25

1.6.2 Model of interactions between translation inhibitors . . . 27

1.7 Aims . . . 28

2 A generalized growth law for translation- and transcription-targeting antibiotics captures drug interactions 30

2.1 Publication . . . 30

2.2 Contributions to the publication . . . 30

3 Drug interactions between translation inhibitors are largely conserved across nutrient conditions 80

3.1 Introduction . . . 80

3.2 Results **82**
3.2.1 Single-drug responses vary across nutrient conditions . . . 82
3.2.2 Most interactions remain stable across nutrient conditions 85
3.2.3 Biophysical model captures part of the measured drug interactions 87
3.3 Discussion **90**
3.4 Materials and Methods **91**
3.4.1 Experimental methods 91
3.4.2 Analysis 91

4 Comparison of GFP reporter dynamics and protein abundance during the diauxic shift **94**
4.1 Introduction **94**
4.2 Results **96**
4.2.1 Dataset characterization and responses during the diauxic shift 96
4.2.2 Temporal agreement between GFP reporter and protein abundance dynamics 100
4.2.3 GFP-derived pseudo mass fractions do not quantitatively reproduce protein mass fractions 103
4.3 Discussion **104**
4.4 Materials and Methods **105**
4.4.1 Experimental methods 105
4.4.2 Analysis 106

5 Ultrasensitive fitness costs arise from membrane proteome displacement under protein overexpression **109**
5.1 Publication **109**
5.2 Contributions to the publication **109**

6 Discussion and Outlook **110**
6.1 How general are bacterial growth laws under different perturbations? **111**
6.2 Can antibiotic interactions be predicted across physiological states? **112**
6.3 What limits the predictive power of resource-allocation models? **114**

A Supplementary Information **117**
A.1 Supplementary Information for chapter 2 . . . . . **117**
A.2 Supplementary Information for chapter 3 . . . . . **128**

List of Figures **133**

List of Tables **135**

Bibliography **137**

1 Introduction

Bacterial growth depends on how cells use their limited resources [1–3]. Nutrients must be taken up and converted into energy and cellular building blocks for protein synthesis, deoxyribonucleic acid (DNA) replication, membrane maintenance and other essential processes [4, 5]. Changes in nutrient availability, gene expression or the inhibition of cellular processes can therefore alter both growth and cellular composition [3, 5]. For example, cells can respond to inhibition by increasing the abundance of proteins associated with the affected process [6] or by allocating more resources to nutrient uptake and metabolism when nutrients are limited [1, 5].
Despite this complexity, some changes in bacterial physiology follow simple quantitative relationships [7, 8]. Two well-known growth laws link growth rate to ribosome abundance under changes in nutrient conditions and translation inhibition [1, 2]. These growth laws connect bacterial growth to the allocation of cellular resources. They have been established mainly for planktonically growing *Escherichia coli* (*E. coli*), the organism used throughout this thesis [2, 9].
The following sections provide the biological and quantitative background for this thesis. Balanced bacterial growth and the main processes of gene expression are described in sections 1.1 to 1.2. The mechanisms by which antibiotics inhibit bacterial growth and interact when combined are introduced in section 1.4. Section 1.5 then describes the connection between growth rate and cellular resource allocation, providing the basis for the growth-law models of antibiotic action discussed in section 1.6.

1.1 Balanced exponential growth

Bacterial growth describes the increase in the number and biomass of cells in a population. A central quantity is the number of cells, N. Direct cell counting is often impractical during continuous growth measurements. In liquid cultures, bacterial abundance can instead be estimated from the turbidity of the culture, which is usually measured as optical density (OD) [10, 11]. OD is calculated from the reduction in transmitted light, typically at a wavelength of 600 nm,

$$\mathrm{OD}_{600} = \log_{10}\left(\frac{I_0}{I}\right), \tag{1.1}$$

where I_0 and I are the incident and transmitted light intensities, respectively. Within an appropriate measurement range, OD_{600} is proportional to biomass. Therefore, it can be used as an accessible measure of bacterial abundance [10, 11]. Growth changes in a batch culture over the course of the experiment. After inoculation, cells first adapt to the new environment during the lag phase, with little or no increase in cell number. They then grow and divide exponentially. Eventually, nutrients become limiting, growth slows and the culture reaches the stationary phase [12]. These phases are illustrated in fig. 1.1.
If cells grow and divide at a constant average rate, their number follows

$$N(t) = N_0 e^{\lambda(t-t_0)}, \tag{1.2}$$

where $N(t)$ is the number of cells at time t, N_0 is the number of cells at a reference time t_0 and λ is the exponential growth rate. The corresponding doubling time is

$$T_\mathrm{d} = \frac{\ln 2}{\lambda}. \tag{1.3}$$

The time at which a culture reaches the stationary phase depends on both the amount and type of nutrients available. Media that support a higher final biomass can often sustain exponential growth longer. Repeated dilution into fresh medium, while cells are still dividing, extends this phase by preventing nutrient depletion (fig. 1.1).

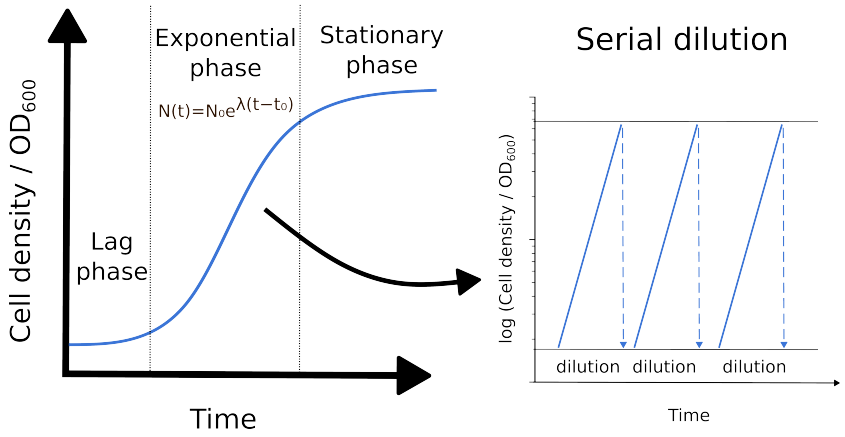


Figure 1.1: **Bacterial growth in batch culture and during serial dilution.** In batch culture, cells pass through lag, exponential and stationary phases. Repeated dilution into fresh medium before nutrients become limiting maintains exponential growth over an extended period.

The population enters *balanced growth* under constant environmental conditions. In this state, the main cellular components increase at the same average rate, while the overall population composition remains constant [13–15].
The same rate λ also describes the increase in total cellular biomass,

$$\frac{\mathrm{d}M}{\mathrm{d}t} = \lambda M, \tag{1.4}$$

where M denotes the total biomass.
Growth conditions affect more than the rate of population growth [16, 17]. For instance, classical studies showed that properties such as cell size, DNA content and ribosome abundance systematically vary with growth rate [7, 8, 15]. Some of these relationships are similar across different nutrient conditions [3–5]. Cells growing at comparable rates can therefore exhibit similar properties, even when the available nutrients differ [7, 16]. These relationships between growth rate and cellular composition form the basis of the bacterial growth laws discussed in section 1.5.

1.2 Gene expression

Cells do not have a fixed composition [17, 18]. Instead, they adapt to their environment by altering the production and abundance of cellular components [1, 5]. Gene expression plays a central role in this adjustment [4, 19].
For protein-coding genes, the information stored in DNA is expressed in two steps. RNA polymerase (RNAP) first transcribes the DNA sequence into messenger RNA (mRNA). Ribosomes then use the mRNA as a template to produce a protein. This flow of information from DNA via ribonucleic acid (RNA) into protein is known as the central dogma of molecular biology [20].

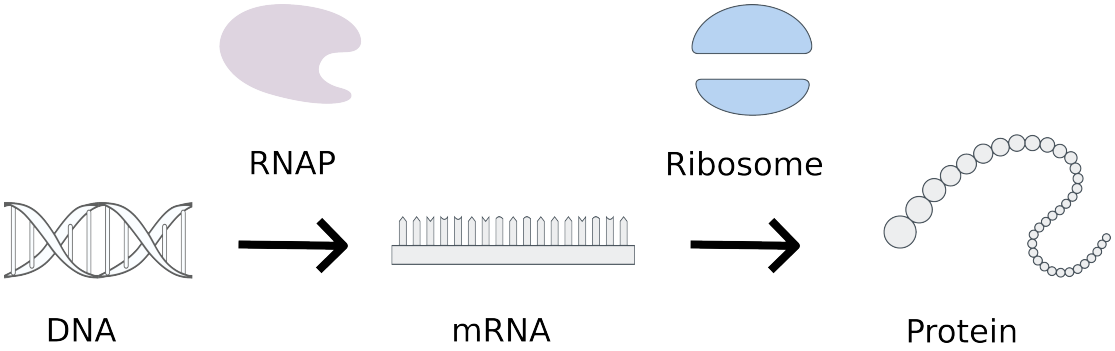


Figure 1.2: **Schematic of gene expression in bacteria.** RNAP transcribes DNA into mRNA. Ribosomes then translate the mRNA sequence into protein.

Transcription and translation rely on different building blocks and cellular machines [19, 21]. Transcription uses nucleotides and is carried out by RNAP, whereas translation uses amino acids and depends on ribosomes. Changes in the supply of these building blocks or in the activity of RNAP and ribosomes can therefore affect gene expression across the cell [22, 23].
Both transcription and translation pass through initiation, elongation and termination, after which their components are recycled. The molecular details differ, but the two processes are closely connected. Their coordination is necessary for efficient protein production and cellular growth [24–26]. The following sections introduce transcription and translation in more detail and describe how they are regulated in bacterial cells.

1.2.1 Transcription

Transcription is performed by RNAP, consisting of the subunits $\alpha_2\beta\beta'\omega$. This core enzyme alone cannot efficiently identify where transcription should begin. Therefore, it binds a sigma factor (σ), forming the RNAP holoenzyme. The sigma

factor guides RNAP to promoter regions, where the DNA opens locally and RNA synthesis starts [27].
Different sigma factors direct RNAP to different groups of genes. The primary sigma factor, σ^{70}, controls many genes needed during normal growth. Other sigma factors become more important when the environment changes. For example, σ^{38} contributes to the response to stress and entry into the stationary phase [27]. Changing the sigma factor allows the cell to redirect RNAP and adjust which genes are transcribed.
After initiation, RNAP moves along the DNA template and extends the RNA in the $5' \rightarrow 3'$ direction. This movement is not always continuous. RNAP can pause or stall and several factors help control these events. NusA and NusG influence pausing, elongation and termination [28], while GreA and GreB can help a stalled RNAP resume transcription [29, 30]. Pausing can also be part of normal gene regulation and may help coordinate transcription with translation [28].
RNAP activity also changes with the physiological state of the cell [31, 32]. During the stringent response, the alarmone guanosine tetraphosphate (ppGpp) and the transcription factor DksA alter transcription and reduce the production of growth-related RNAs, as discussed in section 1.2.3 [33].
Transcription ends when RNAP releases the RNA transcript. This can happen through intrinsic termination, in which the newly produced RNA forms a secondary structure that destabilizes the transcription complex. Alternatively, termination can be driven by the ATP-dependent helicase Rho [34, 35].
Rho-dependent termination also links transcription to translation. In bacteria, ribosomes can begin translating an mRNA while it is still being transcribed. A ribosome that closely follows RNAP covers part of the newly produced RNA and limits access by Rho. If the ribosome falls behind, longer regions of the mRNA remain exposed and premature termination becomes more likely [26, 28, 36].
RNAP and the leading ribosome can also be connected more directly through NusG. One part of NusG binds RNAP, while another can interact with the ribosomal protein NusE [37]. This provides one possible physical link between transcription and translation. Their coordination is discussed further in section 1.2.4.

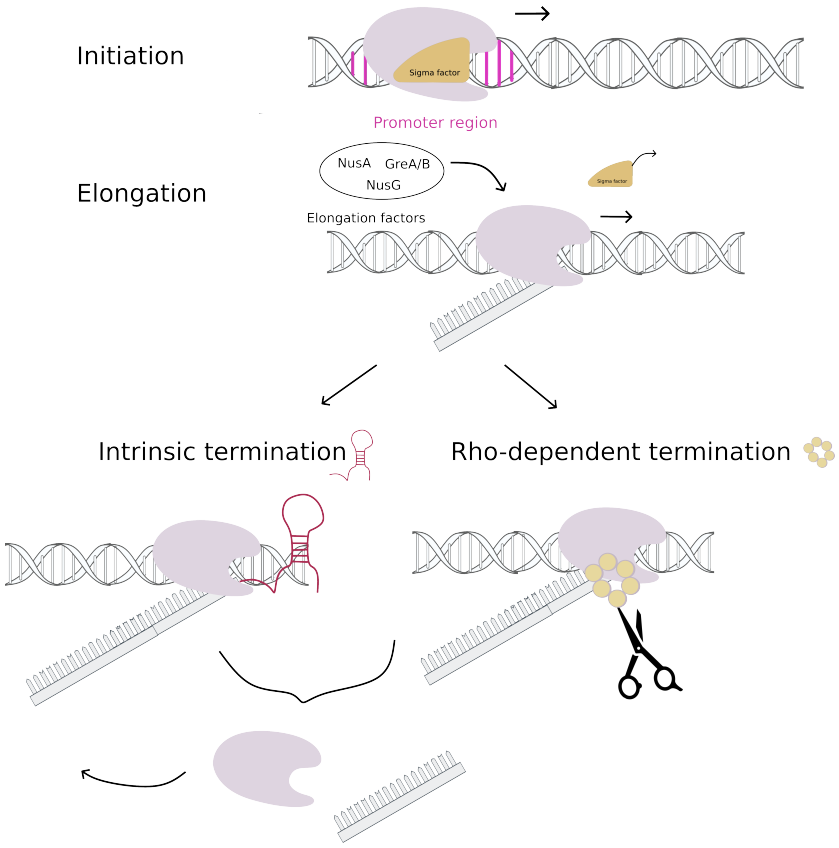


Figure 1.3: **Schematic of bacterial transcription.** During initiation, a sigma factor directs RNAP to the promoter region. After initiation, RNAP elongates the RNA transcript with the help of transcription factors such as NusA, NusG, GreA and GreB. Transcription ends either by intrinsic termination through formation of an RNA hairpin or by Rho-dependent termination, after which RNAP and the RNA transcript are released.

1.2.2 Translation

Translation converts the nucleotide sequence of mRNA into the amino acid sequence of a protein. Protein synthesis is carried out by ribosomes, large ribonucleoprotein complexes. The *E. coli* ribosome consists of a small 30S and a large 50S subunit, both of which are complexes of ribosomal RNA (rRNA) and ribosomal proteins. The 30S subunit contains the 16S rRNA, whereas the 50S subunit contains the 23S and 5S rRNA. Together, the two subunits contain 54 ribosomal proteins [25, 38, 39]. To start translation, an initiation complex must first be formed. This begins with binding of the 30S subunit to the mRNA and recognition of the start codon. In many bacterial mRNAs, start codon recognition is facilitated by base pairing between the Shine-Dalgarno sequence in the mRNA and a complementary sequence in the 16S rRNA [40]. Initiation factors promote the selection of the correct start codon and assembly of the initiation complex. The joining of the 50S subunit then produces the translationally active 70S ribosome, accompanied by conformational changes required for protein synthesis [25]. Protein synthesis proceeds through repeated cycles of incorporation of amino acids into a growing polypeptide chain. Elongation factor thermo-unstable (EF-Tu) delivers aminoacyl-transfer RNA (tRNA) to the ribosome, while elongation factor G (EF-G) promotes the translocation of the ribosome along the mRNA after peptide bond formation [25]. Peptide bonds are formed in the peptidyl-transferase center of the 50S subunit, resulting in the synthesis of polypeptides [41]. The translation elongation rate, together with the abundance of ribosomes, determines the cellular protein synthesis capacity and strongly influences bacterial growth [4, 38, 42, 43]. This relationship is discussed further in section 1.5.3.
Translation continues until a stop codon enters the ribosome and is recognized by release factors, leading to the release of the completed polypeptide and subsequent recycling of the ribosomal subunits [25, 44]. Because ribosome biogenesis and translation consume large amounts of amino acids, nucleotides and energy [4, 5], protein synthesis represents one of the main demands on the bacterial cell [3, 45].

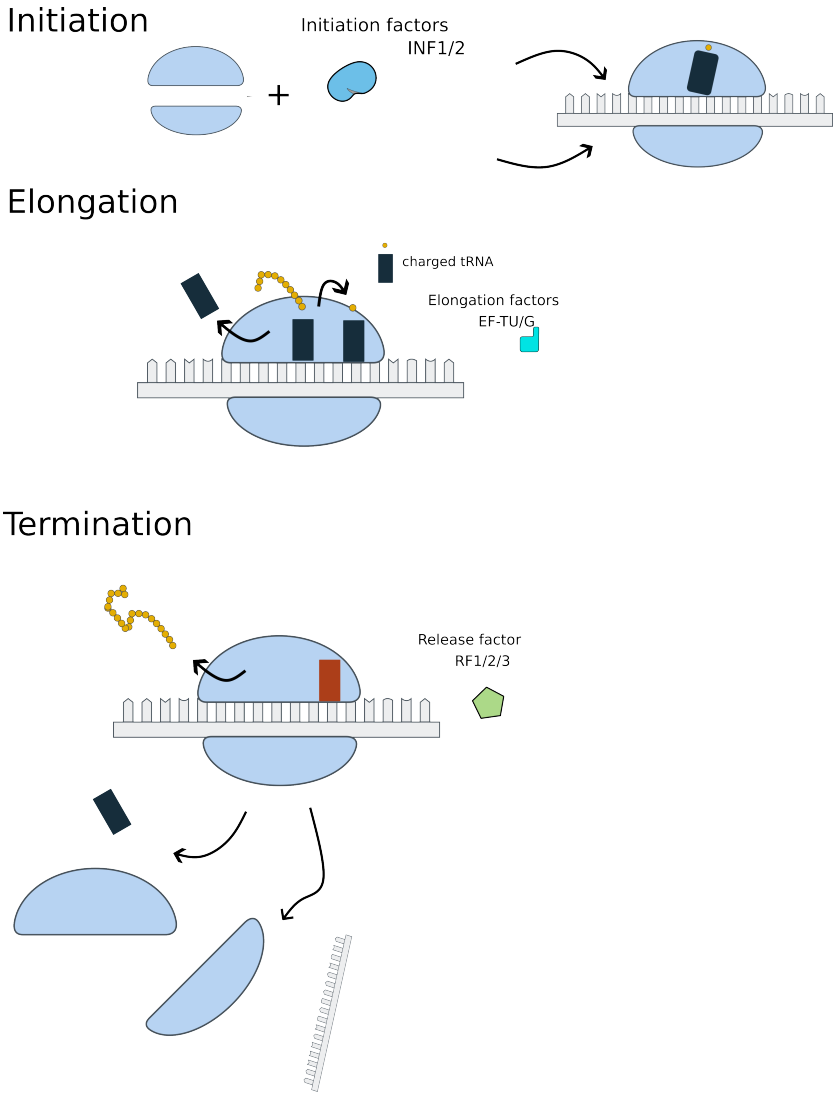


Figure 1.4: **Schematic of bacterial translation.** To initiate translation, the 30S ribosomal subunit binds the mRNA together with initiation factors, followed by joining of the 50S subunit to form the 70S ribosome. During elongation, aminoacyl-tRNAs deliver amino acids to the ribosome and the polypeptide chain is extended. At a stop codon, release factors terminate translation and release the completed protein, followed by recycling of the ribosomal subunits.

1.2.3 Stringent response

In nutrient-poor environments, bacterial cells have to adjust their physiology to the reduced availability of nutrients. The stringent response is an important part of this adaptation. Its main signaling molecules are ppGpp and guanosine pentaphosphate (pppGpp), which are together referred to as (p)ppGpp [31–33].
Translation proceeds efficiently when amino acids are abundant and most tRNAs are charged. During amino acid limitation, charged tRNAs become scarce and uncharged tRNAs accumulate. If an uncharged tRNA enters the A-site of a translating ribosome, the enzyme RelA is activated and starts to produce (p)ppGpp. SpoT also controls the cellular level of (p)ppGpp. It degrades (p)ppGpp and keeps its concentration low under nutrient-rich growth. Under nutrient limitations other than amino acid starvation, SpoT can instead contribute to (p)ppGpp production [31–33].
As (p)ppGpp accumulates, the transcriptional program changes [31, 32]. Together with the transcription factor DksA, (p)ppGpp acts on RNAP and strongly reduces transcription of rRNA genes [33]. The cell produces fewer ribosomes and reallocates resources toward functions needed under nutrient limitation, including upregulation of amino acid biosynthesis [24, 43].
The stringent response connects amino acid availability and translation with ribosome production, transcription and growth [43, 46].

1.2.4 Coupling of transcription and translation

Bacteria lack a nucleus, so transcription and translation occur in the same cellular compartment. Ribosomes start translating mRNA before RNAP has finished producing the transcript. Once the ribosome-binding site and start codon have been transcribed, a ribosome binds to the nascent transcript and initiates translation [24, 28].
A leading ribosome may then follow RNAP as transcription proceeds along the gene. Once the ribosome-binding site becomes available again, additional ribosomes bind to the transcript. Several ribosomes can therefore translate the same mRNA while it is still being transcribed [24, 28].
Translation also affects transcription. By covering the newly synthesized mRNA, the leading ribosome limits regions accessible to Rho and thereby reduces premature Rho-dependent termination. Ribosome movement along the transcript also influences RNA folding and transcriptional pausing [24, 28].
In some cases, RNAP and the leading ribosome interact directly. Structural studies have identified complexes in which the two machines are connected by the nascent mRNA [47, 48]. NusG may provide an additional physical link by binding RNAP with one domain and the ribosomal protein NusE with the other [37].

Such direct contact is not required for coordination. Transcription and translation can remain coordinated even when RNAP and the leading ribosome are separated along the mRNA [48, 49]. Coupling therefore includes both physical interactions between the two machines and broader coordination through the shared transcript. As a consequence, inhibition of transcription affects protein synthesis [22], while changes in translation influence transcriptional elongation and termination [28, 36].

1.3 Post-translational processing and membrane proteins

Translation produces a polypeptide chain, but this chain is not always functional immediately. It first has to fold into the correct three-dimensional structure. Some proteins fold without assistance while others rely on molecular chaperones to prevent misfolding and aggregation [50, 51]. If folding fails, the protein may be refolded or degraded by the cellular protein quality control system [50, 51].
For soluble proteins, folding usually takes place in the aqueous environment of the cytoplasm. Membrane proteins present a different problem because they contain hydrophobic regions that cannot remain exposed in the cytoplasm for long without risking aggregation. These regions have to be brought to a membrane and inserted into the lipid bilayer [52, 53]. Membrane protein production places additional demands on the cell compared with the production of most soluble proteins. This makes membrane proteins especially relevant to the protein overexpression project in chapter 5.

Proteins within bacterial membranes perform many important tasks, including nutrient uptake, respiration, signal transduction, ion transport and antibiotic efflux [52]. A substantial fraction of the proteins encoded by the *E. coli* genome are associated with membranes [53].
Membrane-spanning regions are usually hydrophobic. Many inner membrane proteins contain transmembrane α-helices, whereas β-barrel structures are characteristic of many outer membrane proteins [53, 54].

Membrane protein targeting and insertion

Proteins with transmembrane α-helices are predominantly located in the inner membrane and contain one or several membrane-spanning helices. Other parts of the protein extend into the cytoplasm or the periplasm [55]. Prolonged exposure of these hydrophobic helices in the cytoplasm increases the risk of aggregation. Their synthesis is therefore closely linked to transport to the membrane and insertion into the lipid bilayer [52, 53].
Targeting often begins while the protein is still being translated. As a transmembrane helix emerges from the ribosome, signal recognition particle (SRP) recognizes the nascent protein and brings the ribosome–nascent chain complex to the membrane through the receptor FtsY [52, 53]. Insertion is usually mediated by the SecYEG translocon, often with assistance from YidC [52, 56]. For some proteins, YidC serves as the main insertion pathway [53, 54].
By contrast, β-barrel proteins follow a different route. They are mainly found in the outer membrane, where their transmembrane β-strands form a closed barrel. This structure is common among porins [54]. After synthesis in the cytoplasm, β-barrel proteins are transported across the inner membrane and through the periplasm. The β-barrel assembly machinery (BAM) complex promotes their folding and insertion into the outer membrane [54].

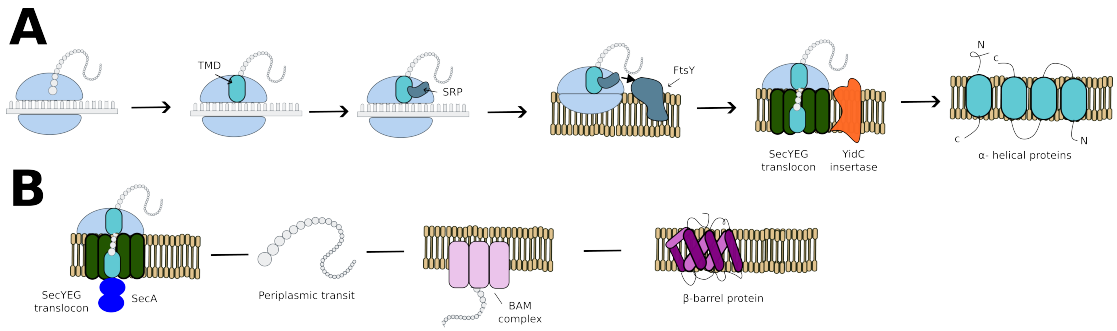


Figure 1.5: **Schematic of bacterial membrane protein biogenesis.** (A) α-helical inner membrane proteins are targeted to the membrane by the SRP–FtsY pathway and inserted through SecYEG, often with the help of YidC. (B) β-barrel proteins cross the inner membrane and are then folded and inserted into the outer membrane by the BAM complex.

Physiological burden of membrane protein overexpression

Membrane proteins are important in both biotechnology and medicine. This group includes transporters, receptors and many proteins involved in antibiotic resistance [57, 58]. Studying their structure or function often requires expression levels far above their natural abundance [59, 60].
High-level expression of membrane proteins often places a severe burden on the cell. Growth may be strongly reduced even when the resulting protein yield remains low [59, 60]. Part of this burden is shared with soluble proteins because transcription and translation consume cellular resources. Membrane proteins impose additional demands through their targeting, insertion by specialized machinery and accommodation within the available membrane space.
The capacity of the SecYEG translocon has been proposed as one possible bottleneck [59]. However, this may not be the only limit. Other parts of membrane biogenesis or the available membrane space itself may also become limiting. Which of these constraints ultimately restricts membrane protein production is still unclear.

1.4 Growth inhibition

In addition to protein overexpression, bacterial growth can be inhibited by antibiotics that target essential processes, including transcription and translation [39, 61, 62]. Inhibition can be quantified through its effect on the exponential growth rate λ. Increasing antibiotic concentrations typically lead to a gradual reduction in growth. The relationship between antibiotic concentration and growth is described by a dose–response curve [62, 63]. Growth rates are normalized to the growth rate in the absence of antibiotics, λ_0. The resulting dose–response curve is fitted using a Hill function

$$\frac{\lambda}{\lambda_0} = \frac{1}{1 + \left(\frac{a_{\mathrm{ex}}}{\mathrm{IC}_{50}}\right)^n}, \tag{1.5}$$

where a_{ex} is the external antibiotic concentration, IC_{50} is the concentration that reduces growth by 50% and n is the Hill coefficient describing the steepness of the dose–response curve.

1.4.1 Transcription and translation inhibitors

Transcription and translation inhibitors disrupt gene expression at different stages. Transcription inhibitors target RNAP or factors involved in RNA synthesis, whereas translation inhibitors interfere with ribosome function and protein synthesis [39, 61]. Transcription inhibitors reduce the synthesis of mRNA and thereby indirectly limit protein production. The best-characterized example is rifampicin, which binds to the β subunit of bacterial RNAP and prevents productive transcription initiation [61, 64]. As a consequence, the synthesis of new transcripts is strongly reduced. Bicyclomycin affects transcription through a different mechanism. It inhibits the transcription termination factor Rho and thereby disrupts Rho-dependent termination [65, 66]. Because resistance can emerge rapidly through mutations in the RNAP β subunit, rifampicin is commonly used as part of combination therapies [67–69].
Translation inhibitors directly reduce protein synthesis by interfering with ribosome function. They constitute a large and well-characterized class of antibiotics [38, 39]. Depending on the compound, inhibition can occur at different stages of the translation cycle, including initiation, aminoacyl-tRNA accommodation, peptide bond formation, translocation, translational fidelity, or progression of nascent polypeptides through the ribosomal exit tunnel [38, 39, 70]. Both transcription and translation inhibitors perturb cellular resource allocation and growth [3, 62]. In particular, partial inhibition of ribosome activity can trigger compensatory changes in ribosome synthesis and proteome composition [1, 5, 42]. Such physio-

logical adaptations form the basis of growth-law models describing the relationship between gene expression, resource allocation and bacterial growth. The antibiotics investigated in this thesis are summarized in Table 1.1.

Table 1.1: Antibiotics investigated in this thesis and their primary targets. Adapted from [71].

Antibiotic	**Abbrev.**	**Target/mechanism**	**Mechanism of action**
Rifampicin	RIF	Transcription initiation	Binds the β subunit of RNAP and blocks extension of nascent RNA beyond a few nucleotides, preventing productive transcription [61, 64].
Chloramphenicol	CHL	Peptide bond formation	Binds near the peptidyl-transferase center (PTC) of the 50S subunit and overlaps with the aminoacyl moiety of A-site tRNA, thereby inhibiting peptide bond formation [38, 39, 72].
Erythromycin	ERM	Nascent chain elongation	Binds within the peptide exit tunnel of the 50S subunit and causes context-dependent inhibition of nascent chain elongation [39, 73, 74].
Kasugamycin	KSG	Translation initiation	Destabilizes initiator tRNA binding and inhibits formation of the canonical translation initiation complex [38, 39, 75].
Lincomycin	LCY	Peptide bond formation	Binds near the peptidyl-transferase center of the 50S subunit and interferes with peptide bond formation [39].
Streptomycin	STR	Decoding fidelity	Perturbs decoding on the 30S subunit, promotes translational errors and affects tRNA accommodation [38, 39, 76].
Tetracycline	TET	Aminoacyl-tRNA accommodation	Prevents binding of aminoacyl-tRNA to the ribosomal A-site [38, 39, 77].
Doxycycline	DOX	Aminoacyl-tRNA accommodation	Tetracycline-class antibiotic that inhibits aminoacyl-tRNA binding to the ribosomal A-site [39].
Capreomycin	CRY	Translocation	Binds at the interface between the ribosomal subunits and stabilizes the 70S ribosome in a pre-translocation state, thereby inhibiting translocation [78].
Fusidic acid	FUS	Translocation and ribosome recycling	Prevents the dissociation of EF-G from the ribosome, thereby inhibiting elongation and reducing the rate of ribosome recycling [79].

1.4.2 Drug combinations

To enhance treatment efficacy and reduce resistance, antibiotics are often studied and used in combination rather than as single compounds [68, 69, 80]. Large-scale interaction studies have shown that the outcome of antibiotic combinations depends strongly on both the drug targets and the bacterial species [80–82]. Drug interactions are commonly measured using checkerboard assays where growth is quantified across a two-dimensional concentration gradient of two drugs [83–85]. They are quantified by comparing the experimentally observed effect of a drug combination with an expected effect calculated from the responses to the individual drugs [69, 80, 82]. A drug combination is synergistic when it inhibits growth more than expected and antagonistic when it inhibits growth less than expected. A particularly strong form of antagonism is suppression, in which the combined inhibitory effect is weaker than that of at least one of the drugs alone [82, 86]. An interaction is additive when the observed effect matches the expected effect.
The expected response depends on the reference model defining additivity [69, 87]. In this thesis, drug interactions are quantified using Loewe additivity, which is based on the principle that a drug combined with itself should be additive and treats two additive drugs as substitutes for one another [71, 88]. Concentration pairs producing the same growth rate form lines of constant growth, called isoboles. Under Loewe additivity, these isoboles are linear [69, 87]. Isoboles bending toward lower drug concentrations indicate synergy, while those bending toward higher concentrations indicate antagonism [71, 88], as shown in fig. 1.6.
For a fixed relative growth level y, the Loewe-additive isobole is defined as

$$\frac{a_1}{\mathrm{IC}_y^{(1)}} + \frac{a_2}{\mathrm{IC}_y^{(2)}} = 1, \tag{1.6}$$

where a_1 and a_2 are the concentrations of the two drugs and $\mathrm{IC}_y^{(i)}$ is the concentration of drug i that alone produces the same relative growth level y. To summarize drug interactions across the complete dose–response surface, we used the Loewe interaction score (LI). This score compares the total volume under the measured growth surface with the volume under the corresponding Loewe-additive surface [71, 88].

$$\mathrm{LI} = \log\left(\frac{\iint y_{\mathrm{obs}}(a_1, a_2)\,\mathrm{d}a_1\,\mathrm{d}a_2}{\iint y_{\mathrm{Loewe}}(a_1, a_2)\,\mathrm{d}a_1\,\mathrm{d}a_2}\right), \tag{1.7}$$

where y_{obs} is the measured normalized growth surface and y_{Loewe} is the corresponding Loewe-additive surface. Thus, $\mathrm{LI} < 0$ indicates synergy, $\mathrm{LI} = 0$ additivity and $\mathrm{LI} > 0$ antagonism.

Because the LI integrates over the complete dose–response surface, it provides an overall measure of interaction strength. The interaction may vary across the concentration range and local synergistic and antagonistic deviations can partly cancel when calculating the overall LI [71, 88].

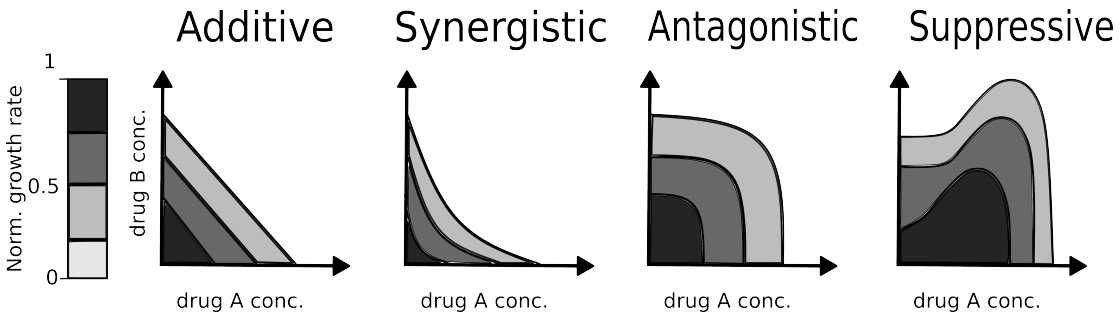


Figure 1.6: **Drug interactions defined by Loewe additivity.** Additive interactions have linear isoboles, while synergy and antagonism bend them toward lower and higher concentrations, respectively. In suppressive interactions, one drug partially counteracts the effect of the other. Different shades indicate different growth levels. Adapted from [69].

Systematic studies of antibiotic pairs have shown that interaction patterns depend on drug targets [82, 86], bacterial species [81] and physiological state [69, 80]. Interactions between translation inhibitors depend on the affected steps of translation, antibiotic transport and ribosome binding [71, 88].
Because drug-combination effects are difficult to predict and systematic testing becomes increasingly demanding as the number of combinations grows, predictive models are needed. This motivates the use of coarse-grained models to predict drug interactions and understand their mechanisms [69, 71, 88].

1.5 Resource allocation

Gene expression is described at different levels. Molecular approaches focus on individual processes such as transcription, translation and their regulation. At a coarser-grained level, the cell is instead described using quantities such as growth rate and proteome allocation [1, 3–5].
Cellular growth corresponds to the accumulation of biomass, as described by eq. (1.4). Biomass production requires protein synthesis and therefore depends on how the available cellular resources are distributed between different functions [4, 5]. Since the total protein in the cell is limited, growth is a resource-allocation problem [1, 3, 45].
It is common to describe this allocation by dividing the proteome into coarse-grained sectors [1, 8, 45]. Instead of following thousands of proteins individually, proteins with similar responses are grouped into sectors [3–5, 89]. The relative mass of each sector is described by the proteome fraction

$$\phi_i = \frac{M_i}{M_{\text{prot}}}, \tag{1.8}$$

where M_i is the protein mass of sector i and M_{prot} is the total cellular protein mass. Depending on the sector and growth condition, this fraction can increase, decrease, or remain approximately constant with growth rate.
The response of an individual protein is not necessarily fixed across all conditions. Proteins may change their growth-rate dependence with the environment or physiological state [3, 5, 89, 90]. The sector description should be understood as a coarse-grained representation of groups of proteins rather than as a strict classification of each protein.
In the simplest description, the proteome is divided into three sectors [1, 3, 5, 45]. The ribosomal sector ϕ_R increases with growth rate under improving nutrient conditions. The nutrient-processing sector ϕ_P, which contains proteins involved in nutrient uptake and metabolism, generally decreases. A third sector, ϕ_Q, remains approximately constant over the investigated growth conditions (fig. 1.7).

Since these sectors together make up the cellular proteome, they are constrained by

$$\phi_R + \phi_P + \phi_Q = 1. \tag{1.9}$$

This is commonly referred to as the proteome budget constraint [1, 8, 45]. An increase in one sector must be compensated for by a decrease elsewhere [3, 5, 91]. The ribosomal sector is particularly important because ribosomes provide the capacity for protein synthesis. A classical observation in bacterial physiology is that ribosome abundance increases with growth rate when nutrient conditions improve [7, 16, 17, 92]. This relationship forms the first bacterial growth law [1, 2, 8].

1.5.1 Growth laws and ribosome allocation

The relation between ribosome abundance and growth rate depends on how growth is changed. Nutrient limitation and translation inhibition, for example, can lead to similar growth rates but very different ribosome concentrations [1, 3, 5, 62]. Overexpression of unnecessary proteins provides a third type of perturbation. These responses are summarized in fig. 1.7.
When growth is varied by changing nutrient quality, the ribosomal proteome fraction increases approximately linearly with growth rate:

$$\phi_{\mathrm{R}} = \phi_{\mathrm{R}}^{\mathrm{min}} + \frac{\lambda}{\kappa_{\mathrm{t}}}, \tag{1.10}$$

where $\phi_{\mathrm{R}}^{\mathrm{min}}$ represents the fraction of ribosomes that does not directly contribute to growth and κ_{t} is the translational capacity [1, 2, 8].
Translation inhibition gives a different response [42, 62]. When growth is reduced by ribosome-targeting antibiotics, cells produce additional ribosomes even though their growth rate decreases [1, 2, 5].

Under these conditions, the ribosomal proteome fraction follows

$$\phi_{\mathrm{R}} = \phi_{\mathrm{R}}^{\max} - \frac{\lambda}{\nu}, \tag{1.11}$$

where $\phi_{\mathrm{R}}^{\max}$ is the maximal ribosomal proteome fraction. The parameter ν describes the nutritional capacity and depends on the nutrient condition [1, 2, 8, 62]. Reducing growth through nutrient limitation and reducing growth through translation inhibition move the ribosomal proteome fraction in opposite directions.
Growth also decreases when cellular resources are used to produce proteins that are not required for growth. These proteins occupy part of the limited proteome and are represented by an additional sector ϕ_{U},

$$\phi_{\mathrm{U}} + \phi_{\mathrm{R}} + \phi_{\mathrm{P}} + \phi_{\mathrm{Q}} = 1. \tag{1.12}$$

Increasing ϕ_{U} leaves less proteome available for ribosome production, nutrient processing, or both. Growth decreases approximately linearly with the fraction allocated to unnecessary proteins [1, 45].

$$\lambda(\phi_{\mathrm{U}}) = \lambda_0 \left(1 - \frac{\phi_{\mathrm{U}}}{\phi_{\mathrm{U}}^{\max}}\right), \tag{1.13}$$

where λ_0 is the growth rate without unnecessary protein expression and $\phi_{\mathrm{U}}^{\max}$ is the maximum proteome fraction that can be allocated to this sector [1, 45].
These three perturbations show that growth rate alone does not specify how the cellular proteome is organized [3–5]. A slowly growing cell under nutrient limitation is not in the same physiological state as a slowly growing cell under translation inhibition. Still, the different responses are consistent with the same limited proteome budget [45, 91].
The growth laws introduce two parameters that describe different parts of this resource-allocation problem: the translational capacity κ_{t} and the nutritional capacity ν. Their relation becomes clearer by considering the balance between nutrient processing and protein synthesis.

1.5.2 Flux-balance model

A simple flux-balance model connects nutrient processing with protein synthesis [1, 8, 45]. The nutrient-processing sector supplies amino acids and other precursors needed for biomass formation. The rate of this process is set by the nutritional capacity ν. The ribosomal sector consumes these precursors for protein synthesis, with a rate determined by the translational capacity κ_{t}.
During balanced growth, production and consumption of these precursors have to match. This gives

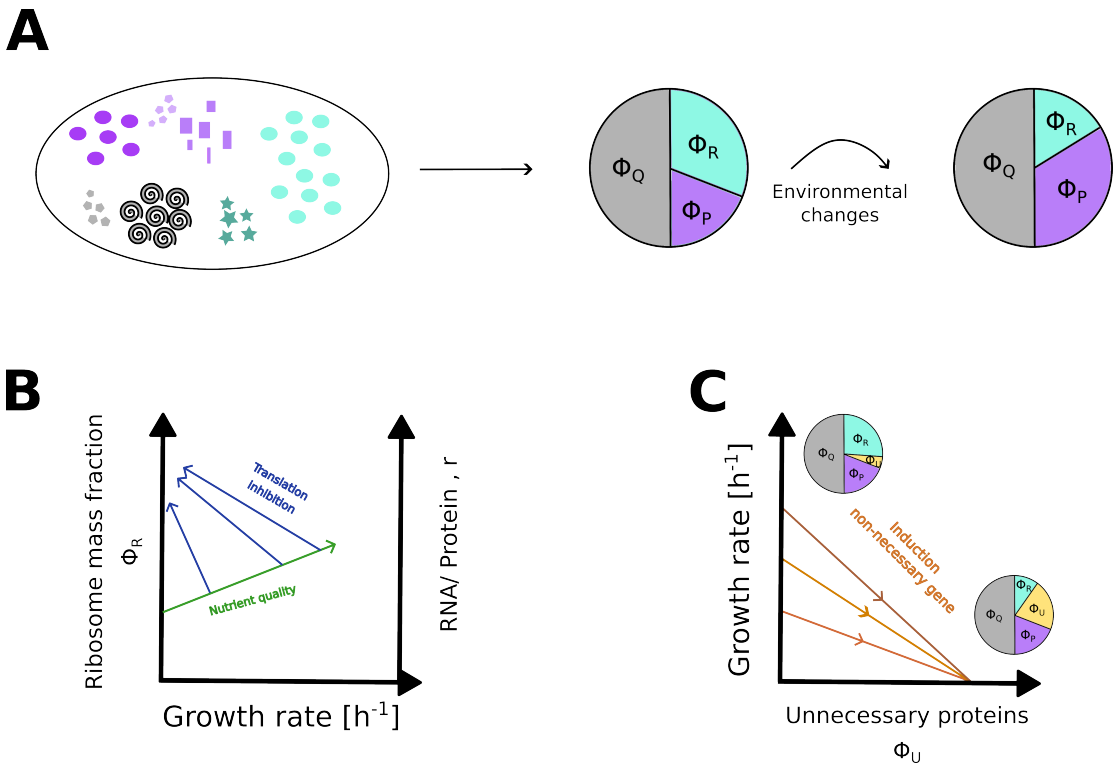


Figure 1.7: **Proteome partitioning and ribosome-centered bacterial growth laws.** (A) Proteome partitioning into ribosomal (ϕ_R, turquoise), nutrient-processing (ϕ_P, purple) and approximately growth-independent (ϕ_Q, gray) sectors. With decreasing nutrient quality, ϕ_R decreases while ϕ_P increases. (B) Ribosome abundance increases with growth rate under changes in nutrient quality but also increases when growth is reduced by translation inhibition. (C) Overexpression introduces an additional sector ϕ_U, reducing the proteome available for growth-related functions and decreasing growth. Adapted from [2, 8].

$$\nu \left(\phi_{\mathrm{P}} - \phi_{\mathrm{P}}^{\mathrm{min}} \right) = \kappa_{\mathrm{t}} \left(\phi_{\mathrm{R}} - \phi_{\mathrm{R}}^{\mathrm{min}} \right). \tag{1.14}$$

Together with the proteome budget, this relation describes the trade-off between nutrient processing and ribosome allocation. More proteome invested in one part of the system leaves less available for the other [1, 3, 5].
At this level, both parameters are still phenomenological. In particular, the model does not specify which molecular processes determine κ_{t}.

1.5.3 Molecular interpretation of translational capacity

The translational capacity κ_{t} can be connected more directly to the molecular processes of protein synthesis. Ribosome abundance alone is not enough to determine the total protein production rate. It also matters how fast ribosomes elongate proteins and how many of them are actively translating [4, 42, 43].
Expressing the active ribosome pool as a fraction f_{a} of the total ribosome population gives

$$\lambda = \epsilon_{\mathrm{R}} \phi_{\mathrm{R}} f_{\mathrm{a}}, \tag{1.15}$$

where $\epsilon_{\mathrm{R}} = \epsilon / L_{\mathrm{R}}$, ϵ is the peptide elongation rate, and L_{R} denotes the amino-acid content of a ribosome [42]. Comparison with the ribosome growth law eq. (1.10) then gives

$$\kappa_{\mathrm{t}} \sim \epsilon_{\mathrm{R}} f_{\mathrm{a}}, \tag{1.16}$$

showing that translational capacity depends on both the elongation rate and the active ribosome fraction [8, 42, 43].
The relative importance of these two quantities depends on how growth is perturbed. Under nutrient limitation, the translational elongation rate decreases as growth slows, while the fraction of active ribosomes also decreases, particularly at very slow growth [42]. Limited amino-acid availability reduces the pool of charged tRNAs and ribosomes spend more time waiting for aminoacyl-tRNAs [43]. At the same time, uncharged tRNAs activate RelA and increase ppGpp synthesis, shifting cellular resources toward amino-acid biosynthesis and away from ribosome production [26, 31–33].
Translation inhibitors produce a different physiological state. Chloramphenicol, tetracycline and erythromycin act through different molecular mechanisms (table 1.1), but each removes a fraction of the ribosome population from productive translation [42, 62]. The elongation rate of the remaining active ribosomes can stay relatively high. Growth reduction is mainly associated with a decrease in f_{a} rather than a substantial decrease in ϵ.
This also changes the cellular response. When translation is inhibited, amino-acid consumption decreases and charged tRNAs accumulate [42, 43]. RelA activity and ppGpp levels decrease, while ribosome synthesis increases [22, 31, 32]. The cell compensates for the lower fraction of active ribosomes by producing more ribosomes. This provides a molecular explanation for the increase in ribosome abundance described by the second growth law [1, 43, 62].
Not every translation inhibitor affects translational capacity in the same way. Fusidic acid primarily reduces elongation by inhibiting EF-G-mediated translocation [42, 79]. Mupirocin instead limits the supply of charged tRNAs and activates the stringent response [31–33, 93]. In summary, translation inhibition can reduce growth through various molecular pathways (fig. 1.8). Nutrient limitation and translation inhibition can produce similar growth rates while acting on different parts of the translation machinery. The growth laws describe the resulting changes in ribosome allocation, but they do not connect these changes to the concentration or binding properties of an antibiotic. To do this, antibiotic transport and ribosome binding have to be included explicitly [62].

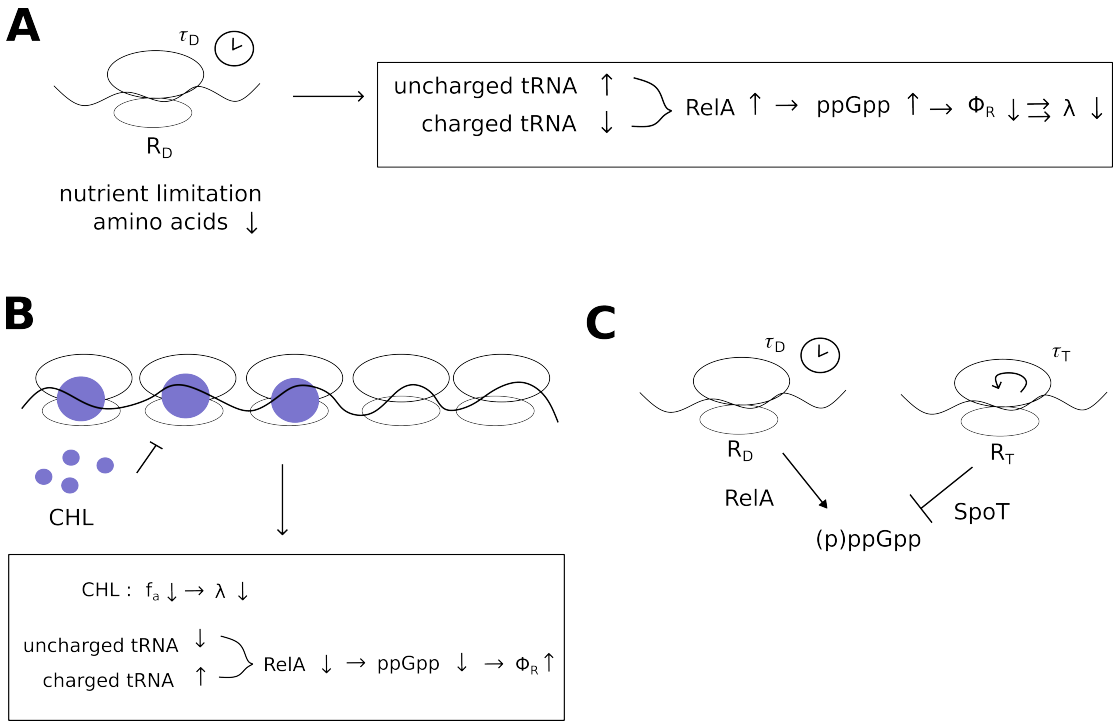


Figure 1.8: **Molecular mechanisms underlying changes in translational capacity.** (A) Nutrient limitation reduces tRNA charging, activates RelA and ppGpp synthesis and decreases ribosome production, while limited charged-tRNA availability slows peptide elongation. (B) Translation inhibition by chloramphenicol (CHL) primarily reduces the active ribosome fraction f_a. Reduced amino-acid consumption increases tRNA charging, lowers ppGpp levels and stimulates ribosome synthesis, resulting in an increased ribosomal proteome fraction ϕ_R. (C) RelA and SpoT couple the translational state of ribosomes to ppGpp homeostasis and ribosome synthesis. Reduced growth can result from either decreased elongation rate or a reduced fraction of active ribosomes. Adapted from [26, 33, 42, 94].

1.6 Growth law-based models of antibiotic action

1.6.1 Mechanistic model of translation inhibition

The mechanistic model used in this thesis links the growth law response to translation inhibition with antibiotic transport and binding to ribosomes [62]. Antibiotics enter and leave the cell and bind to ribosomes, reducing the pool available for translation. Ribosome synthesis changes according to the growth laws described above. The model therefore links antibiotic binding to the cell's physiological response [1, 62].

Different transport and binding properties produce different dose–response curves. Some translation inhibitors show a steep, threshold-like decrease in growth, while others inhibit growth more gradually [62]. These response regimes are characterized by the dimensionless parameter $\alpha = \lambda_0^*/\lambda_0$, where λ_0 is the drug-free growth rate and λ_0^* is a drug-specific reversibility scale determined by antibiotic transport, ribosome binding and translational capacity [62]. Small values of α give steep responses, whereas larger values give more gradual inhibition.

A second drug-specific quantity, IC_{50}^*, defines the characteristic antibiotic concentration scale. It depends on the available ribosome pool, antibiotic influx and the reversibility scale [62, 71, 88]. The observed IC_{50} depends on both IC_{50}^* and α. Therefore, changes in the drug-free growth rate can alter both the shape of the dose–response curve and antibiotic susceptibility.

These predictions are relevant for comparing single-drug responses across different nutrient conditions [62]. The steady-state solution of the model is used in section 3.2.1.

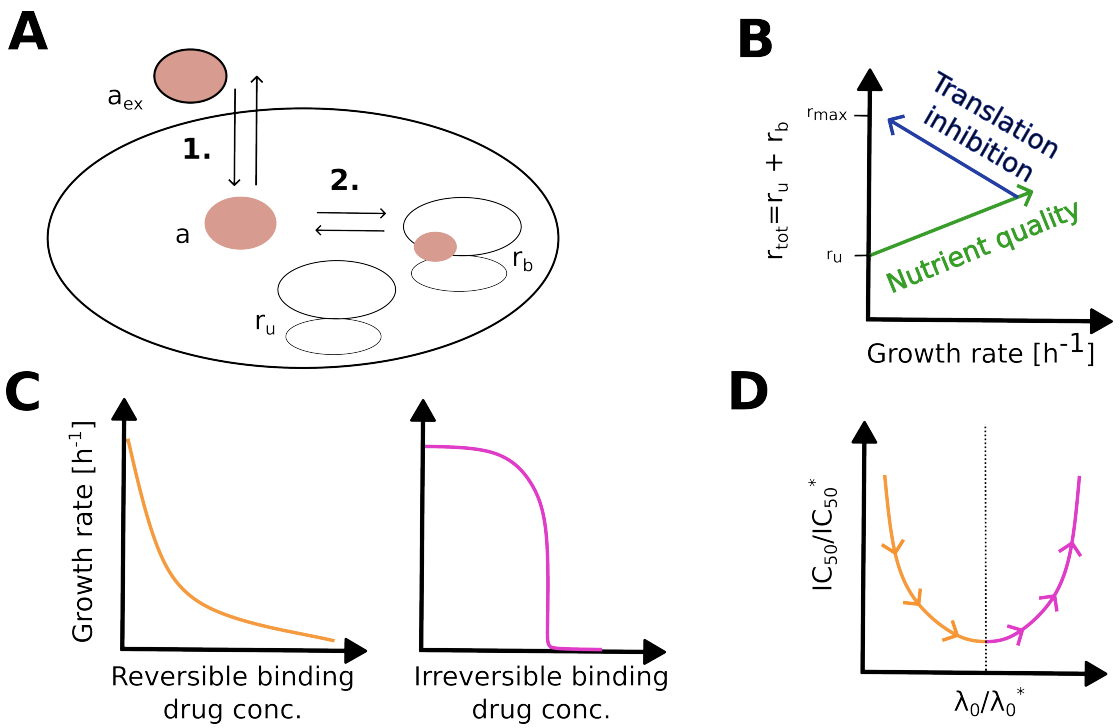


Figure 1.9: **Growth law-based model of translation inhibition.** (A) Antibiotics enter the cell and bind to ribosomes, reducing the pool available for protein synthesis. (B) Antibiotic transport and ribosome binding are coupled to the growth law response of ribosome synthesis. (C) Different effective reversibility regimes result in gradual or steep dose–response curves. (D) Changes in the drug-free growth rate can alter susceptibility and give rise to the predicted relation between drug-free growth rate and IC_{50}. Adapted from [62].

1.6.2 Model of interactions between translation inhibitors

The single-drug model was later extended to combinations of two translation inhibitors [71, 88]. The model uses the properties of the individual dose–response curves to predict the combined response [71, 88]. In addition, it takes into account how the two antibiotics bind to the ribosome. For each drug, IC_{50} sets the concentration scale and α describes the shape of the single-drug response. The two-drug model then distinguishes between different binding situations. Two antibiotics can compete for binding, preventing both from occupying the same ribosome. In that case, if one drug occupies the ribosome, the second drug cannot bind to the same ribosome and therefore does not produce an additional inhibitory effect. Alternatively, both drugs can bind independently, allowing a double-bound ribosome to form [71, 88]. Competitive binding leads to linear isoboles and an additive interaction according to the Loewe definition. If both drugs (A and B) can bind at the same time, the response also depends on α_A and α_B. Drug pairs with small α values and thus steep single-drug responses tend to show antagonism. For larger values of α, the interaction can become additive or synergistic [69, 71, 88]. This gives the interaction phase diagram shown in fig. 1.10.
The model can be used to compare interaction behavior with the properties of the two individual drugs. In particular, it allows testing whether changes in the single-drug responses under different nutrient conditions are also reflected in the corresponding drug interaction. The model is applied to the measured two-dimensional growth responses in chapter 3.

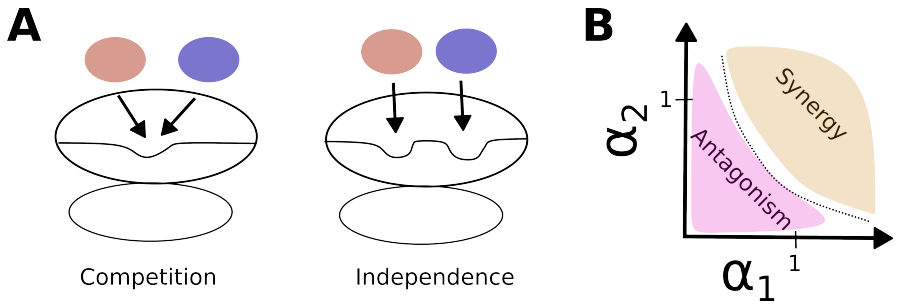


Figure 1.10: **Prediction of interactions between two translation inhibitors.** (A) Schematic of competitive and independent ribosome binding. (B) Predicted interaction regimes for independent binding for α_1 and α_2. Adapted from [71, 88].

1.7 Aims

Bacterial growth laws and resource-allocation models describe several physiological responses using a few quantitative relationships. However, it remains unclear how broadly these relationships apply when the targeted cellular process, growth environment or type of perturbation changes. This thesis examined the predictive capacity of existing coarse-grained models, whether these models require extensions and which additional physiological constraints are important. I addressed these questions through four related aims.

Aim 1: Extending growth law-based models to translation and transcription inhibition. Growth law-based models have mainly been used to describe responses to translation inhibition. It remained unclear whether the same principles could also be applied to transcription inhibition. I measured growth and proteome allocation under antibiotics targeting translation or transcription, both alone and in combination. The goal was to extend the growth law framework to combinations of transcription and translation inhibitors and determine whether it could explain the resulting drug interactions.

Aim 2: Testing how nutrient conditions shape antibiotic susceptibility and drug interactions. Antibiotic susceptibility depends on the cell's physiological state. I characterized translation inhibitors under different nutrient conditions that support different growth rates and quantified drug interactions across these conditions. The purpose was to determine how well the framework describes changes in single-drug susceptibility and dose–response shape. I also tested whether changes in individual drug responses alter antibiotic interactions and whether these interactions can be predicted from single-drug measurements.

Aim 3: Comparing GFP reporter dynamics with protein abundance. Green fluorescent protein (GFP) reporter libraries provide a scalable way to track changes in gene expression, while proteomics measures protein abundance directly. The two measurements do not necessarily agree. I compared genome-wide GFP reporter signals with proteomic measurements during the diauxic shift. The aim was to determine how closely reporter signals reflect changes in protein abundance and to identify systematic differences between the two approaches.

Aim 4: Investigating the cost of protein overexpression. Protein overexpression provides another way to perturb the allocation of cellular resources. As part of a collaborative project, I contributed to experiments measuring the fitness costs caused by overexpression of different proteins. A particular focus was placed on membrane proteins and on whether their overexpression introduces constraints beyond the general cost of protein production. The objective was to identify the physiological processes that limit growth during protein overexpression.

2 A generalized growth law for translation- and transcription-targeting antibiotics captures drug interactions

2.1 Publication

The work titled *A generalized growth law for translation- and transcription-targeting antibiotics captures drug interactions* is available as a preprint on bioRxiv [95].

2.2 Contributions to the publication

Matteo Mori, Tobias Bollenbach and I contributed to the study. All experiments and analyses were conducted by me. Matteo Mori helped establish the analysis pipeline for quantitative proteomics. Tobias Bollenbach, Matteo Mori and I wrote the manuscript.

bioRxiv preprint doi: https://doi.org/10.64898/2026.08.21.746212; this version posted August 24, 2026. The copyright holder for this preprint (which was not certified by peer review) is the author/funder, who has granted bioRxiv a license to display the preprint in perpetuity. It is made available under a CC-BY-NC-ND 4.0 International license.

A generalized growth law for translation- and transcription-targeting antibiotics captures drug interactions

Natawan Gadjisade[1], Matteo Mori[2], and Tobias Bollenbach[1,3,‡]

1. Institute for Biological Physics, University of Cologne, 50931 Cologne, Germany
2. Department of Physics, University of California at San Diego, La Jolla, CA, USA
3. Center for Data and Simulation Science, University of Cologne, 50931 Cologne, Germany

‡ Correspondence: t.bollenbach@uni-koeln.de

Abstract

Bacterial growth laws quantitatively connect intracellular resource allocation to growth rate, enabling accurate predictions of physiology and antibiotic responses. Yet these laws have been rigorously tested for only a handful of perturbations. Here, we show that the growth law linking ribosome levels to growth rate under translation-inhibiting antibiotics is not universal, but rather depends on the antibiotic's mechanism of action. Quantitative proteomics across finely resolved one- and two-dimensional antibiotic gradients showed that inhibitors of translocation elongation or peptide bond formation elicit the canonical rise in ribosome levels, consistent with the growth law. By contrast, antibiotics disrupting translation initiation or fidelity produced distinct responses without ribosome upregulation. The transcription inhibitor rifampicin even reduced ribosome abundance. Combining antibiotics with divergent ribosome responses revealed a generalized growth law, in which the individual responses to perturbations superimpose. Embedding this law in a mathematical model explains distinct drug interaction patterns observed between rifampicin and different translation inhibitors. A low-dimensional structure pervades the entire proteome, enabling prediction of responses to drug pairs based on single-drug measurements. Together, these findings broaden the scope of bacterial growth laws and provide new principles for predicting responses to antibiotic combinations.

Introduction

The controlled perturbation of cell physiology using antibiotics has revealed core principles of bacterial systems biology. Bacterial growth laws link exponential growth rate to ribosome concentration, providing a key ingredient for building predictive frameworks for antibiotic responses[1–4]. The ribosome concentration increases linearly with growth rate when nutrient conditions improve, a core principle expressed in the *first growth law*[4–8]. However, under translation inhibition, the ribosome concentration increases linearly as the growth rate is decreased, with a slope that depends on the nutrient environment (*second growth law*)[5].

bioRxiv preprint doi: https://doi.org/10.64898/2026.08.21.746212; this version posted August 24, 2026. The copyright holder for this preprint (which was not certified by peer review) is the author/funder, who has granted bioRxiv a license to display the preprint in perpetuity. It is made available under a CC-BY-NC-ND 4.0 International license.

Remarkably, both relationships are believed to be largely independent of molecular detail, holding across diverse ways of altering nutrient conditions and inhibiting translation. Thus, growth laws have the potential to bridge the gap between physiology and phenotypic plasticity, serving as empirical laws in biology, much like Ohm's law or the ideal gas law in physics[5,6].

However, it is unclear how broadly growth laws apply, given that they have mostly been investigated using a limited number of perturbations in *Escherichia coli* laboratory strains[5,9,10]. Translation proceeds through multiple steps, and different translation inhibitors target distinct stages[11,12]. Yet the second growth law has only been rigorously validated for a handful of translation inhibitors—including chloramphenicol, tetracycline, and erythromycin—using the RNA-to-total-protein ratio (RNA/protein) as a proxy for ribosome content[5,9,13]. Recent advances in mass-spectrometry now allow direct quantification of protein abundances[14,15]. Proteomics has revealed how bacteria adjust their proteome allocation beyond the ribosome[16]. Under translation inhibition, for instance, ribosomal protein levels rise, while levels of other proteins, such as enzymes involved in carbon metabolism, fall[14,15]. For chloramphenicol, proteomics data closely align with RNA/protein-based measurements of ribosome levels, and thus with the second growth law[5,9,15]. Therefore, a systematic proteomic comparison across mechanistically distinct translation inhibitors would help assess the generality of the second growth law.

This issue is important for mathematical models based on bacterial growth laws, which can accurately describe bacterial responses to antibiotics[1,9,17]. These models have successfully predicted the dependence of antibiotic susceptibility on nutrient conditions and the shape of the dose-response curve, which relates growth rate to antibiotic concentration[1,17]. The latter enables the inference of binding parameters of translation inhibitors without direct measurement[1]. Notably, bistable regimes, in which bacteria either grow or fail to grow depending on prior history, have been predicted and experimentally validated in different contexts[17–19]. All of these successes are based on one premise: translation inhibitors reduce the number of active ribosomes, prompting the cell to compensate by increasing ribosome synthesis according to the second growth law[1,5,9].

A closely related mathematical model has been used to predict drug interactions between translation inhibitors[2,3]. Synergistic or antagonistic drug interactions occur when the combined effect of two antibiotics on growth is stronger or weaker than expected based on an additive reference, respectively[20–25]. Antagonistic interactions are common among translation inhibitors because bottlenecks at different stages of translation can partially compensate for one another[2]. Conversely, purely additive interactions are often observed for translation inhibitors with similar modes of action or overlapping ribosomal binding sites[2,24–26].

bioRxiv preprint doi: https://doi.org/10.64898/2026.08.21.746212; this version posted August 24, 2026. The copyright holder for this preprint (which was not certified by peer review) is the author/funder, who has granted bioRxiv a license to display the preprint in perpetuity. It is made available under a CC-BY-NC-ND 4.0 International license.

In many cases, the individual dose-response curves provide sufficient information to infer uptake and target-binding kinetics, which the model then uses to predict pairwise interactions[2,3,21]. These results show that a quantitative description of global cell physiology can illuminate the mechanistic basis of drug interactions. They also highlight the need to test growth-law predictions in multidrug contexts.

The predictive power of growth laws raises the question of whether analogous relations exist for the perturbation of bacterial functions other than translation. Transcription inhibition is a prime candidate because it affects the synthesis of rRNA, tRNA, and mRNA, all of which are tightly linked to translation[27]. This involvement could be captured by generalizing the existing theoretical framework for translation inhibitors[1,3]. Recent mathematical models have incorporated the role of transcription by considering RNA polymerase (RNAP) and mRNA levels[28–30]. These models predict that growth can sometimes be limited by mRNA availability rather than by ribosomes[30,31]. Another prediction is that ribosome levels can increase, decrease, or remain constant under transcription inhibition depending on the nutrient environment; an increase is predicted in poor nutrient conditions and a decrease in rich conditions[30]. However, experimental validation is sparse: direct measurements of ribosome levels and global proteome allocation under transcription inhibition—alone or combined with translation inhibitors—are missing. For rifampicin, RNA/protein measurements hint at a distinct resource allocation pattern[30,32–34], but quantitative proteomics under transcription inhibition has yet to be performed.

Beyond ribosome levels, global responses to drug combinations may follow general principles[35–37], pointing to a more general, low-dimensional structure in how biological systems respond to perturbations[38]. High-resolution transcriptional measurements across two-dimensional drug concentration gradients revealed that most gene expression levels interpolate the responses to the individual drugs along lines of constant growth rate in both *E. coli*[36] and yeast[37]. Depending on the drug interaction, the transition can be either smooth and continuous or relatively abrupt[35–37]. This growth-rate-anchored interpolation is a candidate empirical law for predicting the effects of combinations from single-drug data, but it has not yet been tested at the protein level.

Here, we report how translation and transcription inhibitors differentially impact *E. coli* proteome allocation, and how these differences shape drug interactions. We found that certain translation inhibitors violate the second growth law, as ribosome concentration remained constant despite a decrease in growth rate. The transcription inhibitor rifampicin even induced a linear decline in ribosome levels. Combining translation inhibitors with rifampicin revealed a generalized growth law that partly explains the differences in drug interactions between rifampicin and different translation inhibitors. High-resolution

bioRxiv preprint doi: https://doi.org/10.64898/2026.08.21.746212; this version posted August 24, 2026. The copyright holder for this preprint (which was not certified by peer review) is the author/funder, who has granted bioRxiv a license to display the preprint in perpetuity. It is made available under a CC-BY-NC-ND 4.0 International license.

proteomics across two-dimensional drug gradients further revealed a low-dimensional structure of the response space, enabling partial prediction of proteome reallocation and drug interaction under multidrug stress.

Results

Ribosome responses to antibiotics depend on drug mode of action

To quantify how the bacterial proteome reorganizes in response to antibiotics, we performed quantitative data-independent acquisition (DIA) mass-spectrometry proteomics on *E. coli* cultures in steady-state exponential growth exposed to various translation and transcription inhibitors. We inferred protein abundances from peptide-level measurements using the xTop algorithm and converted them to absolute proteome mass fractions with the help of published ribosome-profiling reference data[39] (Methods). We collected two independent datasets under different cultivation conditions: one in a mini-bioreactor (15 mL) under tightly controlled growth at fixed optical density, and another in flasks where cultures were precultured and diluted into antibiotic-containing medium (20 mL). Both ensured balanced exponential growth at the time of sampling, as verified by optical density tracking (Methods). We generated a comprehensive dataset of several conditions in duplicate using both techniques. We profiled proteomes across graded growth inhibition induced by carbon limitation, as well as one- and two-dimensional gradients of antibiotics targeting different stages of translation and transcription (Fig. 1A). Across both datasets, 1,700 to 2,400 proteins were detected per condition, including at least 43 ribosomal proteins and at least 7 RNAP-associated proteins. Reproducibility was high across both replicates and cultivation procedures (Methods). The resulting dataset provides a high-resolution map of proteome allocation under various stressors.

Our proteomics experiments reproduced the canonical growth-law relationships for ribosome allocation. To determine how these changes in ribosome levels were accompanied by broader proteome reorganization, we assigned proteins to functional sectors[40] and tracked the proteome mass fractions of different sectors across conditions and growth rates (Table S1). As a physiological benchmark, we first examined carbon limitation induced by increasing concentrations of α-methylglucoside, a non-metabolizable glucose analog (Methods). Under this perturbation, growth rate and ribosome concentration decreased in parallel, following an approximately linear relationship, consistent with the first growth law[9] (Fig. 1B). In contrast, the translation inhibitors chloramphenicol and erythromycin, which block peptide bond formation and translocation, respectively (Fig. 1A), caused an approximately linear increase in ribosome concentration as growth rate decreased (Fig. 1B), in line with the second growth law[9]. This ribosome upregulation was accompanied by

bioRxiv preprint doi: https://doi.org/10.64898/2026.08.21.746212; this version posted August 24, 2026. The copyright holder for this preprint (which was not certified by peer review) is the author/funder, who has granted bioRxiv a license to display the preprint in perpetuity. It is made available under a CC-BY-NC-ND 4.0 International license.

proportional downregulation of other sectors, particularly central carbon metabolism (Fig. S1; Table S1)[14,15], consistent with a feedback loop in which stalled ribosomes stimulate the production of more ribosomes to maintain translational capacity[1,9,29,41]. The agreement under previously reported perturbations validates the quantitative accuracy of our proteomic measurements[14,15].

Motivated by numerous mathematical models of bacterial translation inhibition that invoke the compensatory ribosome upregulation captured by the second growth law[1–3,5,9,17], we asked whether this response is conserved across antibiotics that target different stages of protein synthesis. Tetracycline and doxycycline, which block tRNA entry into the ribosomal A-site[42], induced an increase in ribosome concentration. However, this increase was modest compared with chloramphenicol and erythromycin (Figs. 1B and S2A). Notably, streptomycin, an aminoglycoside that disrupts translation fidelity[11,12,43], and kasugamycin, which blocks translation initiation[44], failed to elicit ribosome upregulation (Figs. 1B and S2A) and produced only modest sector-level reorganization relative to untreated bacteria (Table S1). Recent RNA/protein measurements revealed a similar lack of ribosome upregulation when translation initiation was inhibited using CRISPRi to knock down translation initiation factor IF-1 (*infA*)[45]. These differences suggest that ribosome compensation is most effective when translation elongation is slowed or stalled, allowing bacteria to offset reduced translational throughput by increasing ribosome abundance. In contrast, the effects of antibiotics that block initiation or corrupt decoding fidelity appear to be compensated for less effectively[11,12,42,43]. Together, these data show that there is no universal proteome response to translation inhibition; instead, the response reflects the specific molecular mechanism of different antibiotics.

Next, we explored how the proteome adapts to transcriptional inhibition, a fundamentally different perturbation that indirectly impairs translation by reducing the supply of rRNAs, mRNAs, and tRNAs. Unlike translation inhibitors, rifampicin, an antibiotic that blocks transcription initiation by inhibiting RNAP[32], caused a decline in ribosome concentration as growth rate decreased, following an approximately linear trend, albeit less steep than under carbon limitation (Fig. 1B). In parallel, the mass fraction of RNAP increased substantially in response to rifampicin, again following an approximately linear trend (Fig. 1C; Methods). This reciprocal response – ribosome levels down, RNAP levels up – mirrors the ribosome upregulation observed under translation inhibition (Fig. 1B), but in reverse: here, the bacteria appear to boost the abundance of the inhibited enzyme to counteract reduced transcriptional flux. In line with this view, RNAP levels were essentially unchanged under most translation inhibitors, showing only minor increases, e.g., under tetracycline, and a slight decrease under chloramphenicol (Fig. 1C). We also observed that central carbon pathways were

bioRxiv preprint doi: https://doi.org/10.64898/2026.08.21.746212; this version posted August 24, 2026. The copyright holder for this preprint (which was not certified by peer review) is the author/funder, who has granted bioRxiv a license to display the preprint in perpetuity. It is made available under a CC-BY-NC-ND 4.0 International license.

expressed at higher levels in rifampicin-treated cells than in translation-inhibited cells, and at similar levels to those in carbon-starved cells (Fig. S1). Notably, the expression level of the premature transcription termination factor Rho, which plays a key role in coordinating transcription-translation coupling[46,47], behaved similarly to ribosomal protein concentration across all perturbations investigated here (Fig. S2C). This suggests that the need for premature transcription termination changes in tandem with total translation capacity. Together, these results show that antibiotics elicit distinct proteome allocation responses depending on whether translation or transcription is perturbed. They also highlight that core cellular machinery, such as the ribosome, can be regulated in opposite ways by closely related perturbations.

Combining transcription and translation inhibitors reveals a generalized growth law

The contrasting responses to translational and transcriptional inhibition raise the question of how bacteria respond when both processes are inhibited simultaneously: Do the combined perturbations generate a qualitatively different proteome allocation state, or do bacteria transition continuously between the single-drug responses corresponding to each process? To resolve this, we systematically mapped proteome reorganization under combined antibiotic perturbations, starting with ribosomal proteins and transcriptional machinery, and then extending the analysis to the entire proteome.

We first examined the combination of rifampicin and chloramphenicol, which elicit strongly opposing ribosomal allocation responses when applied alone (Fig. 1B). Ribosome allocation followed a superposition of the responses to the individual drugs. Progressively increasing chloramphenicol concentrations at a fixed rifampicin concentration resulted in an upregulation of ribosome levels, following an approximately linear trend (Fig. 2A,B). The slope of this increase increased with decreasing growth rate in the rifampicin-only condition (Fig. 2B). Notably, this behavior resembles that observed across nutrient conditions in the second growth law[5,7–9], despite quantitative differences. Conversely, increasing the rifampicin concentration at fixed chloramphenicol concentration pulled the system to the lower-ribosome rifampicin state (Fig. S3A,B). Independent measurements under balanced exponential growth conditions in a controlled bioreactor reproduced the observed growth-ribosome trajectories (Fig. S3C,D; Methods). Therefore, the combined rifampicin–chloramphenicol treatment robustly produced a superposition of the two opposing ribosome responses to the individual drugs.

To test whether this superposition principle holds more generally, we examined rifampicin combined with kasugamycin—a drug that, on its own, leaves ribosome levels essentially

bioRxiv preprint doi: https://doi.org/10.64898/2026.08.21.746212; this version posted August 24, 2026. The copyright holder for this preprint (which was not certified by peer review) is the author/funder, who has granted bioRxiv a license to display the preprint in perpetuity. It is made available under a CC-BY-NC-ND 4.0 International license.

unchanged (Fig. 1B). The corresponding ribosome concentrations remained tightly constrained across conditions (Fig. 2C). Increasing the kasugamycin concentration at a fixed rifampicin concentration caused only modest deviations from the rifampicin trajectory (Fig. 2C), reflecting the limited response induced by kasugamycin alone. As with the rifampicin–chloramphenicol pair, the combined response was consistent with a superposition of the single-drug responses, albeit within a narrow dynamic range that precluded detailed quantitative analysis.

These results suggest that, under combined drug stress, ribosome allocation follows a generalized growth law in which the two single-drug states are superimposed (Fig. 2B,C). They further imply that mathematical models of bacterial physiology based on growth laws[1–3], which connect cellular resource allocation to fitness, can be extended rigorously to antibiotic combinations, when relaxing the ad hoc assumption that the second growth law holds universally[1–3,21].

Antibiotic-specific ribosome responses rescale drug susceptibility and reshape drug interactions

We asked whether the drug-specific ribosome responses (Fig. 1B) could account for the differences in drug interactions observed when different translation inhibitors are combined with a transcription inhibitor. To characterize these interactions, we mapped lines of constant growth rate (isoboles) in two-dimensional drug space, using Loewe additivity as the null model[20]. Straight isoboles indicate additivity; convex isoboles indicate synergy (i.e., stronger-than-additive growth inhibition); and concave isoboles indicate antagonism (i.e., weaker-than-additive growth inhibition) (Fig. 3A). To quantify global drug interaction patterns using a compact metric, we computed the interaction score, LI_{log}, which is defined as the logarithm of the ratio of the integrated measured growth response surface to the corresponding additive reference surface[2]. Positive LI_{log} values indicate antagonism, $LI_{log} \approx 0$ indicates additivity, and negative values indicate synergy (Methods). The strongest interactions between ribosome inhibitors, which include highly suppressive interactions caused by ribosome traffic jams on mRNAs, have $|LI_{log}| > 0.2$, but interactions with $|LI_{log}| > 0.1$ are robustly detectable[2].

Although both drugs target translation, chloramphenicol and kasugamycin behaved differently when paired with the transcription inhibitor rifampicin. The rifampicin–chloramphenicol growth response surface revealed pronounced antagonism between the two antibiotics ($LI_{log} = 0.11$; Fig. 3B), a result that was independently reproduced in a mini-bioreactor ($LI_{log} = 0.12$; Fig. S4B). By contrast, the rifampicin–kasugamycin growth response surface remained close to additive ($LI_{log} \approx 0$; Fig. 3C). This implies that the combination with compatible ribosome responses (Fig. 2C) remained additive, while the combination with divergent single-drug responses (Fig. 2B) produced strong antagonism. This observation

bioRxiv preprint doi: https://doi.org/10.64898/2026.08.21.746212; this version posted August 24, 2026. The copyright holder for this preprint (which was not certified by peer review) is the author/funder, who has granted bioRxiv a license to display the preprint in perpetuity. It is made available under a CC-BY-NC-ND 4.0 International license.

suggests that ribosome allocation under stress can influence the effects of drug combinations.

To address whether the transition from near-additivity to antagonism between rifampicin and translation inhibitors stems from their distinct ribosome responses, we extended a mathematical model of antibiotic effects on bacterial growth. This extension relaxes the fixed ribosome-growth relationship (second growth law) and introduces a drug-specific ribosome-response parameter, θ, which scales the magnitude of ribosomal up- or down-regulation (Supplementary Text). We analyzed the model in steady state, corresponding to balanced exponential growth at fixed drug concentrations. In this framework, θ = 1 reproduces the strong compensatory ribosome upregulation of the second growth law observed with chloramphenicol, $\theta \approx 0$ captures the minimal reallocation as observed with kasugamycin, and $\theta < 0$ describes the ribosome downregulation induced by rifampicin (Fig. 1B). The resulting generalized ribosome-growth relation (Fig. 3D), which extends previously used growth laws[1–3,5], is given by

$$r_{\mathrm{tot}}(\lambda;\theta) = r_0 + \theta \cdot s_{\mathrm{G}} \cdot (\lambda - \lambda_0).$$

Where r_{tot} is the total ribosome concentration, λ is the growth rate, r_0 and λ_0 denote the ribosome concentration and growth rate in the drug-free reference condition, respectively, and s_{G} is the slope of the original second growth law[5]. This generalization captures the spectrum of experimentally observed ribosome responses while maintaining the predictive power of earlier growth-law models.

In this model, modulating the ribosome response preserves the intrinsic shape of the dose-response curve for translation inhibitors, but rescales the effective drug concentration axis, resulting in a horizontal shift of the curve (Fig. S4A). Thus, the ribosome-response parameter θ acts as an independent lever on drug susceptibility. In particular, a lack of compensatory ribosome upregulation ($\theta \approx 0$) markedly increases susceptibility to translation inhibitors (Fig. S4A). By contrast, altering the shape of the dose-response curve requires changes to kinetic parameters, such as drug binding, unbinding, or transport[1]. This finding highlights the ribosome-response parameter θ as a key regulatory node that modulates antibiotic susceptibility without altering their intrinsic potency.

To capture the joint action of a transcription inhibitor and a translation inhibitor, we next extended the model to two drugs. We treated the transcription inhibitor (drug X, e.g., rifampicin) as a modifier of the physiological background, while the translation inhibitor (drug Y) acts within this altered background. Based on our experimental observations (Figs. 1B and 2B-C), we described the transcription inhibitor as reducing the effective growth rate in a manner analogous to nutrient limitation:

bioRxiv preprint doi: https://doi.org/10.64898/2026.08.21.746212; this version posted August 24, 2026. The copyright holder for this preprint (which was not certified by peer review) is the author/funder, who has granted bioRxiv a license to display the preprint in perpetuity. It is made available under a CC-BY-NC-ND 4.0 International license.

$$\lambda_0(c_X) = \lambda_{00} \cdot g_X(c_X).$$

Here, $g_X(c_X)$ is the normalized dose-response curve of drug X, λ_{00} denotes the drug-free growth rate, and $\lambda_0(c_X)$ is the background growth rate established by drug X. Thus, the transcription inhibitor shifts the physiological context in which the translation inhibitor operates.

We assumed that the ribosome response to the translation inhibitor retains the same functional form as in the single-drug case, but is applied to the physiological state set by the transcription inhibitor (Supplementary text). Consequently, both the dynamic range of accessible ribosome concentrations and the susceptibility to the translation inhibitor become functions of the transcription inhibitor concentration, matching the trends seen experimentally (Fig. 2B,C). Solving the model showed that, at each fixed transcription inhibitor concentration, the dose-response curve of the translation inhibitor is simply rescaled (Fig. S4A), and the system remains monostable. Therefore, the steady state reached is independent of the order in which the drugs are added. The full set of these rescaled dose-response curves constitutes the growth response surface (Supplementary text). This two-drug model thus reveals how the interaction between transcription and translation inhibitors is governed by the ribosome-response parameter θ, provided that the antibiotics do not disrupt other cellular processes (e.g., drug uptake) that are not included in the model.

In contrast to the single-drug case, where different ribosome responses merely rescale the effective dose, in the two-drug case these responses can reshape the interaction landscape. The resulting growth-response surfaces revealed that drug pairs with opposing ribosome responses, such as rifampicin and chloramphenicol, produce markedly concave isoboles, indicating antagonism (Fig. 3E). Conversely, combinations of drugs with weaker, more similar ribosome responses, such as rifampicin and kasugamycin, produce nearly straight isoboles, indicating additivity (Fig. 3F). Thus, the model predicts stronger antagonism for rifampicin–chloramphenicol than for rifampicin–kasugamycin (Fig. 3E,F), a trend that aligns qualitatively with experimental data (Fig. 3B,C). Moreover, the interaction scores closely match, while the detailed shapes of the response surfaces differ, partly due to measurement noise (Fig. 3B,C,E,F). Together, these results provide evidence that drug-specific ribosome responses are key determinants of drug interaction outcomes. More broadly, they reveal how antibiotic-induced proteome reorganization can shape response surfaces, providing a mechanistic link between cellular physiology and drug interactions.

bioRxiv preprint doi: https://doi.org/10.64898/2026.08.21.746212; this version posted August 24, 2026. The copyright holder for this preprint (which was not certified by peer review) is the author/funder, who has granted bioRxiv a license to display the preprint in perpetuity. It is made available under a CC-BY-NC-ND 4.0 International license.

An interpolation principle captures the proteome-wide response to antibiotic combinations

After finding that the ribosome concentration responds to antibiotic combinations according to a generalized growth law (Fig. 2), we wondered whether a similar principle might govern individual proteins across the entire proteome. Our high-resolution quantitative proteomics dataset spanning fine-grained two-dimensional antibiotic concentration gradients (Figs. 2 and S3; Table S2) enables us to address this question systematically. To dissect how *E. coli* rearranges its proteome globally, we performed principal component analysis (PCA) on the measured protein expression levels (Methods). In essence, this approach extracts the dominant response modes, or principal components (PCs), that capture most of the variance in the data. Each protein's expression across the entire two-drug space can then be approximated as a linear combination of a small number of PCs (Methods). Previous studies that applied this analysis to transcriptional regulation data under drug combinations in *E. coli* and yeast showed that the first three PCs explain more than 95% of the variance[36,37,48], revealing a low-dimensional structure that enables predictions of responses to combinatorial perturbations. Here, we extend this framework to the protein level—arguably the most functionally relevant layer of cellular regulation[5,9,14,15].

The leading PCs dominate the variance in protein levels in response to antibiotic combinations. Across all datasets, the top three PCs collectively account for roughly 80% of the variance (Fig. 4A). However, the explanatory power of additional PCs diminishes rapidly: explaining 95% of the variance typically requires about ten PCs, with components beyond the third each explaining less than 5% (Fig. 4A). This indicates that protein-level responses to drug combinations occupy a higher-dimensional space than transcriptional responses. Still, the first two PCs explain most of the variance, raising the question of whether they reflect biologically interpretable response modes.

The first two PCs capture the bulk of the proteome response: a global allocation shift driven by changes in growth rate and a finer adjustment that resolves drug-induced regulatory conflicts. Since growth rate exerts a dominant effect on cellular physiology at all levels[5,7,9,14,15,28,41,46], we dissected protein levels along isoboles to separate this strong growth effect from other response modes[36,37]. The first PC, which explains 55-65% of the variance for different antibiotic pairs (Fig. 4A), is essentially flat along isoboles (Figs. 4B,D and S5F). In addition, the scores of the first PC across samples were strongly correlated with the corresponding growth rates; the correlation was much weaker when the first PC scores were compared to the relative drug fraction (Fig. S6A-D; Methods). Thus, this component captures the global response to growth-rate modulation, regardless of which drug causes it. The high fraction of variance explained aligns with the expected dominant effect of growth-rate

bioRxiv preprint doi: https://doi.org/10.64898/2026.08.21.746212; this version posted August 24, 2026. The copyright holder for this preprint (which was not certified by peer review) is the author/funder, who has granted bioRxiv a license to display the preprint in perpetuity. It is made available under a CC-BY-NC-ND 4.0 International license.

changes on proteome rearrangements. Most of the contribution to the first PC loadings derived from amino acid and nucleotide biosynthetic pathways, which are typically regulated in response to the demand flux via feedback inhibition (Fig. S6E-H; Methods).

The scores of the second PC, which contributes 12-22% of the variance, were not correlated with growth, but rather with the relative drug fraction (Fig. S7A-D; Methods). Thus, the second PC captures how regulatory conflicts are reconciled under drug combinations when protein levels diverge between single-antibiotic treatments. An analysis of how different protein functional groups contribute to the loadings of the second PC highlighted the main changes in the proteome (Fig. S7E-H; Methods). For the rifampicin-chloramphenicol pair, ribosomal proteins had a negative projection, and central carbon pathways had a positive projection (Fig. S7E,F), in agreement with the single drug proteomics results (Fig. 1B, Fig. S1). For this drug pair, we also observed a negative contribution for nucleotide biosynthetic pathways (Fig. S7E,F), possibly due to lower nucleotide consumption in transcription-inhibited cells. For the rifampicin-kasugamycin pair, the results were similar, except for a less prominent contribution from ribosomal proteins (Fig. S7G), due to their more similar growth-rate dependence (Fig. 1B). Finally, the results for the erythromycin-tetracycline pair did not highlight any specific protein groups other than ribosomal proteins (Fig. S7H), indicating that these two drugs mostly elicit responses that differ on a finer scale. Along isoboles traversing the two-drug space, conflicting protein levels are smoothly interpolated (Figs. 4B-D and S5F), as previously observed at the transcriptional level[36,37,48].

The quantitative pattern of regulatory conflict interpolation mirrors the drug interactions. We used the relative drug fraction, a coordinate derived from each drug's concentration in the combination relative to its half-maximal inhibitory concentration (IC_{50}), to specify positions along isoboles in two-drug space (Methods). Along the 50% growth-inhibition isobole, the relative drug fraction ranges from 0 (only drug X) to 0.5 (equal contributions of X and Y, relative to their IC_{50}) to 1 (only drug Y). For the nearly additive rifampicin–kasugamycin pair (Fig. 3C), the second PC exhibited an almost perfectly linear interpolation of regulatory conflicts along the isobole (Fig. 4B). A similar linear interpolation emerged for the additive combination of the two translation inhibitors erythromycin and tetracycline (Fig. S5F). By contrast, the antagonistic rifampicin–chloramphenicol pair (Fig. 3B) produced a mildly sigmoidal second PC centered at a relative drug fraction of 0.5 (Fig. 4D), indicating a more switch-like transition between the conflicting single-drug responses.

This interpolation principle was also evident at the level of individual proteins. We classified each protein's abundance trajectory along IC_{50}-normalized isoboles as linear, sigmoidal, or ambiguous based on whether they were better fit by a sigmoidal function or a straight line,

bioRxiv preprint doi: https://doi.org/10.64898/2026.08.21.746212; this version posted August 24, 2026. The copyright holder for this preprint (which was not certified by peer review) is the author/funder, who has granted bioRxiv a license to display the preprint in perpetuity. It is made available under a CC-BY-NC-ND 4.0 International license.

while penalizing additional fit parameters (Methods). For the antagonistic rifampicin–chloramphenicol combination, the vast majority (>80%) of classified proteins exhibited switch-like sigmoidal transitions centered at a relative drug fraction of 0.5, rather than gradual linear behavior (Fig. 4E). This points to a prioritization strategy for antagonistic drug pairs, in which bacteria switch from one response program to another, depending on which antibiotic dominates. A notable example is the transcription-termination factor Rho, which transitions relatively abruptly from an elevated expression level under chloramphenicol to a lower level under rifampicin as the relative drug fraction crosses the 0.5 threshold (Fig. 4E). These results provide evidence for a more general interpolation principle: regulatory conflicts are linearly interpolated for additive drug pairs, while antagonistic drug pairs elicit switch-like transitions, extending earlier transcription-level findings[36,37] to the proteome.

Only a handful of proteins deviated qualitatively from the interpolation principle. This principle also does not accurately capture ribosome levels along isoboles (Fig. S9); instead, they align with the generalized growth law (Fig. 5). This is likely due to their exceptional regulatory mechanisms, which are more elaborate than those of most other proteins[7,49]. We found no consistent evidence of emergent responses, i.e., protein levels under the combination that exceeded or fell below both single-drug treatments. Any hints of such emergent responses under dual treatment (Fig. S8D) proved inconsistent across the dataset. Therefore, the proteome response to antibiotic combinations appears to be remarkably simple, as it is well captured by interpolating between the protein-level responses to the individual drugs. In practice, two ingredients are sufficient to predict the global proteome allocation under drug combinations: (i) the universal growth inhibition effect captured by the first PC, and (ii) each protein's specific response to the individual antibiotics. Applying the interpolation principle together with a high-resolution growth-response surface enables the direct prediction of most combinatorial outcomes from the responses to individual drugs.

Discussion

Our results show that the bacterial proteome allocation response to translation-inhibiting antibiotics depends critically on the drug's molecular mechanism of action and does not universally adhere to the second growth law. Inhibitors of translocation elongation or peptide bond formation produced the expected increase in ribosome concentration, whereas antibiotics targeting other stages of translation, such as initiation or decoding, resulted in a weaker or absent increase (Fig. 1B). In contrast, rifampicin-induced transcription inhibition triggered the opposite trend: ribosome levels declined while RNAP abundance increased (Fig. 1C). Under combined inhibition of transcription and translation, ribosome levels followed a superposition of the single-drug responses, closely resembling the second growth

bioRxiv preprint doi: https://doi.org/10.64898/2026.08.21.746212; this version posted August 24, 2026. The copyright holder for this preprint (which was not certified by peer review) is the author/funder, who has granted bioRxiv a license to display the preprint in perpetuity. It is made available under a CC-BY-NC-ND 4.0 International license.

law under different nutrient conditions (Fig. 2). Incorporating this generalized growth law into a mathematical model of bacterial growth produced the graded levels of antagonism between rifampicin and different translation inhibitors (Fig. 3), indicating that drug interactions are at least partially shaped by stress-induced proteome reorganization. Building on earlier results at the transcriptional level[36,37,48], we further showed that protein levels under antibiotic combinations are often smoothly interpolated along isoboles, rendering them partially predictable from the single-drug responses and growth-rate measurements alone (Fig. 4).

The divergent ribosome responses to distinct translation inhibitors likely arise from their different modes of action. In particular, these responses may be explained by signaling through the alarmones guanosine tetraphosphate and pentaphosphate, collectively termed (p)ppGpp, which represses ribosome production[50–52]. Synthesis of (p)ppGpp is stimulated under nutrient limitation, especially amino acid starvation, as uncharged tRNAs accumulate and activate the ribosome-associated (p)ppGpp synthetase RelA[51]. Inhibitors of translocation elongation or peptide bond formation, such as chloramphenicol, erythromycin, tetracycline, and doxycycline cause ribosomes to stall, thus reducing the fraction of active ribosomes[41]. The resulting surplus of charged tRNAs may suppress (p)ppGpp levels, thereby triggering the compensatory upregulation of ribosome production (Fig. 1B). This view aligns with the recent observation that (p)ppGpp levels are inversely related to the translation elongation rate across diverse growth conditions, suggesting that (p)ppGpp synthesis reflects the balance between dwelling ribosomes awaiting charged tRNAs and those undergoing productive translocation during elongation[29]. In contrast, drugs that block initiation, such as kasugamycin, or corrupt decoding fidelity, such as streptomycin, may not generate the stalled-ribosome signal needed to trigger compensatory ribosome production. To dissect these non-canonical responses (Fig. 1B), it will be essential to directly probe and perturb (p)ppGpp dynamics and other regulators of ribosome production[53].

The decrease in ribosome concentration observed under rifampicin (Fig. 1B) is also mechanistically plausible. Rifampicin directly inhibits bacterial RNAP, reducing global mRNA synthesis and limiting the productive translation of all proteins, including ribosomal proteins[32]. Because ribosome biogenesis requires an exceptionally high level of transcription from rRNA operons[7,49], a loss of transcriptional capacity disproportionately impairs rRNA synthesis. Since the rate of ribosome production is largely determined by rRNA synthesis[7,29,41], rifampicin thereby limits the formation of new ribosomes, which offers a plausible explanation for the observed decrease in ribosome mass fraction relative to the proteome. This response is also consistent with recent theory proposing that growth under transcriptional limitation depends on both ribosome abundance and mRNA availability[30]. This work predicted a

bioRxiv preprint doi: https://doi.org/10.64898/2026.08.21.746212; this version posted August 24, 2026. The copyright holder for this preprint (which was not certified by peer review) is the author/funder, who has granted bioRxiv a license to display the preprint in perpetuity. It is made available under a CC-BY-NC-ND 4.0 International license.

decrease in ribosome concentration in response to transcriptional inhibition in richer nutrient environments, which turns into an increase in poorer nutrient environments[30]. Our experiments used a defined medium with glucose as the carbon source (Methods), which supports a relatively high growth rate in *E. coli*, rendering the observed ribosome response broadly consistent with this prediction. An interesting direction for future work is testing the predicted effect of transcription inhibition by extending these quantitative proteomics measurements to poorer nutrient conditions.

Our results point to quantitative principles that govern bacterial responses to combinatorial perturbations in balanced exponential growth. First, the ribosome response to combinations of antibiotics that elicit distinct responses individually (Fig. 2) suggests that the second growth law may be a special case of a more general law. A non-translation perturbation – such as reduced nutrient quality or transcription inhibition – elicits a decline in ribosome abundance that depends linearly on growth rate (Fig. 5A). When translation is inhibited while holding the non-translation perturbation fixed, ribosome abundance again changes linearly with growth rate (Fig. 5B). Quantitatively, this second change mirrors the translation-inhibition response observed without the primary perturbation, but with a rescaled growth rate axis. Inhibitors of translocation elongation or peptide bond formation, such as chloramphenicol, elicit an increase in ribosome abundance, as predicted by the classical second growth law. However, the generalized growth law also captures the response to initiation inhibitors such as kasugamycin, and to other antibiotics for which ribosome abundance remains nearly constant. It makes concrete predictions, e.g., for the ribosome response to kasugamycin under different nutrient conditions (Fig. 5C). Whether this organizing principle applies to antibiotics with different modes of action or other stressors is an interesting question for future study.

Second, we found an interpolation principle that explains much of the proteome response to drug combinations based on the responses to the individual drugs (Fig. 4). This finding builds upon earlier studies in *E. coli* and yeast showing that transcriptional responses to antibiotic combinations occupy a low-dimensional space largely determined by the single-drug responses[36,37,48]. We found that the same principle extends to the proteome, the more functionally relevant layer. After factoring out the dominant growth-rate effect, additive drug pairs exhibit near-linear interpolation between single-drug proteome states, whereas antagonistic combinations produce more switch-like transitions between distinct physiological programs (Fig. 4B,D). The first PC (growth rate) explained a smaller fraction of the variance than in prior transcriptomic studies (Fig. 4A), likely because protein levels are subject to tighter post-transcriptional regulation, and proteomic sampling is sparser and noisier. Denser sampling along growth isoboles[37] could sharpen the extraction of low-

bioRxiv preprint doi: https://doi.org/10.64898/2026.08.21.746212; this version posted August 24, 2026. The copyright holder for this preprint (which was not certified by peer review) is the author/funder, who has granted bioRxiv a license to display the preprint in perpetuity. It is made available under a CC-BY-NC-ND 4.0 International license.

dimensional proteome response modes. Collectively, these findings indicate that large swaths of the bacterial response to antibiotic combinations can be predicted from single-drug data, offering a strategy to avoid the combinatorial explosion in drug-combination design.

Although our study examined several mechanistically distinct antibiotics, the broader landscape of translation and transcription inhibitors offers fertile ground for future work. Several inhibitors act through distinct mechanisms that may help further elucidate the interplay between translation and transcription in bacteria. For example, we did not investigate transcription elongation inhibitors such as streptolydigin, which perturbs RNAP through a mechanism that differs from that of rifampicin[32,54,55]. Similarly, aminoacyl-tRNA synthetase inhibitors such as mupirocin, which strongly activate the stringent response through accumulation of uncharged tRNAs[50–52,56], could elicit markedly different proteome allocation states. The same applies to translation inhibitors that cause premature chain termination and proteotoxic stress, such as puromycin[57]. Applying quantitative proteomics to these antibiotics and their combinations would further challenge the universality of the identified principles of bacterial physiology.

The fact that biophysical models of resource allocation extend so readily from translation to transcription inhibition underscores the power of empirical growth laws derived from quantitative proteomics. Further advances in proteomics methodology, such as improved coverage, more accurate absolute quantification, and robust cross-species normalization, could extend this framework to antibiotics targeting other cellular processes, and to bacteria beyond *E. coli*. In other species, the relationship between ribosome abundance and growth rate may differ[10], and regulators other than (p)ppGpp may take center stage[58]. Combining these advances with high-throughput, automated sample preparation will enable rigorous testing of whether system-level antibiotic stress responses are universally governed by low-dimensional physiological constraints. Ultimately, this approach could transform the design of effective antibiotic combination therapies from a process of trial-and-error to one of quantitative prediction.

Methods

Bacterial strains

Experiments were performed using *Escherichia coli* K-12 BW25113 carrying the pCS-λ plasmid, which encodes the constitutive *luxCDABE* reporter system. Calibration measurements were performed using the EQ353 strain, as described in[14,39].

bioRxiv preprint doi: https://doi.org/10.64898/2026.08.21.746212; this version posted August 24, 2026. The copyright holder for this preprint (which was not certified by peer review) is the author/funder, who has granted bioRxiv a license to display the preprint in perpetuity. It is made available under a CC-BY-NC-ND 4.0 International license.

Growth media

Unless otherwise stated, bacteria were grown in M9 minimal medium consisting of 1×M9 salts (Sigma-Aldrich, M6030), supplemented with 2 mM $MgSO_4$ (Sigma-Aldrich, M7506), 0.1 mM $CaCl_2$ (VWR, 22317), and 4 g/L glucose (Sigma-Aldrich, G8270). Carbon limitation experiments were performed by increasing the concentration of methyl α-D-glucopyranoside (Sigma-Aldrich, M9376-1KG) while keeping the glucose concentration constant. This resulted in methyl α-D-glucoside/glucose ratios of 5, 10, 15, and 20. For the calibration experiments, cultures of the EQ353 strain were grown in MOPS minimal medium prepared as described in[39], using MOPS (Sigma-Aldrich, M3183-500G).

Antibiotics

We used rifampicin (Sigma-Aldrich, R3501-1G), chloramphenicol (Sigma-Aldrich, C0378), kanamycin (Sigma-Aldrich, K4000), streptomycin sulfate (Sigma-Aldrich, S6501-25G), tetracycline (Sigma-Aldrich, 87128), doxycycline hyclate (Sigma-Aldrich, D9891-1G), kasugamycin hydrochloride from *Streptomyces kasugaensis* (Sigma-Aldrich, K4013-10G), and erythromycin hydrate (Sigma-Aldrich, 856193-25G). Stock solutions of rifampicin, streptomycin sulfate, and kasugamycin were prepared in pure water (MilliQ). Chloramphenicol, tetracycline, doxycycline, and erythromycin stock solutions were prepared in ethanol. All stock solutions were filter sterilized and stored at −20°C.

Bioreactor and batch culture growth assays for proteomics samples

Batch culture experiments

Batch culture experiments were performed in 100 mL Erlenmeyer flasks containing 20 mL of medium. The flasks were incubated in a shaking incubator at 37°C and 250 rpm. Cultures were inoculated from frozen stocks by 1:1,000 dilution into a pre-culture medium that was identical to the respective experimental conditions. During the exponential growth phase, the cultures were further diluted 1:100 into fresh medium to obtain the desired starting conditions. Growth was monitored by measuring the optical density at 600 nm (OD_{600}) using a spectrophotometer (NanoDrop OneC). Samples were harvested for further protein extraction at OD_{600} = 0.20.

Bioreactor experiments

Aliquots of frozen overnight cultures (50 µL in 15% glycerol) were thawed and inoculated at a 1:10,000 dilution into flasks containing 15 mL of growth medium connected to the mini-bioreactor system (OGI Biotec, Bioreactor Mk3 Main CCA). Growth was continuously monitored. Samples (10 mL) for proteomics analysis were collected at OD_{600} = 0.2 to ensure sampling during the exponential growth phase. The bioreactor system estimates cell density using a backscatter signal, which was calibrated against spectrophotometric OD_{600}

bioRxiv preprint doi: https://doi.org/10.64898/2026.08.21.746212; this version posted August 24, 2026. The copyright holder for this preprint (which was not certified by peer review) is the author/funder, who has granted bioRxiv a license to display the preprint in perpetuity. It is made available under a CC-BY-NC-ND 4.0 International license.

measurements using a power-law relationship $\mathrm{OD} = p_0 + p_1 \cdot x^{p_2}$, where ($x$) denotes the measured backscatter signal. All bioreactor experiments were performed at 37°C.

Proteomics sample processing

Samples were centrifuged for 12 min at 3,000 × *g* at 4°C using a refrigerated centrifuge. The supernatant was discarded, and cell pellets were washed with 2 mL PBS buffer (Carl Roth, 1107.1). The pellets were then centrifuged again for 2 min at 13,000 × *g* using a tabletop centrifuge and subsequently stored at −80°C until protein extraction.

Protein quantification

Total protein concentration was determined using a modified Lowry assay (Total Protein Kit Micro Lowry, Peterson's modification; Sigma-Aldrich, TP0300-1KT), which was adapted for small sample volumes.

Proteomics sample preparation

We prepared proteomics samples according to the standard protocol of the CECAD/CMMC Proteomics Facility at the University of Cologne. Cell pellets were washed with ice-cold PBS and resuspended in 100 µL lysis buffer containing 100 mM ammonium bicarbonate (Sigma-Aldrich, A6141), 2% sodium deoxycholate (Sigma-Aldrich, D6750), and protease inhibitor cocktail (cOmplete, Roche, 04693159001). Cells were lysed by vortexing and sonication on ice. Cell debris was then removed by centrifugation (16,000 × g, 15 min, 4 °C). The supernatant was transferred to a fresh tube and stored at −80 °C until further processing. Protein concentration was determined prior to digestion. Approximately 30 µg protein was reduced with 5 mM dithiothreitol (DTT) for 1 h at 20 °C and alkylated with 40 mM chloroacetamide (CAA) for 30 min at 30°C in the dark. Proteins were digested with Lys-C at an enzyme-to-substrate ratio of 1:75 for 4 h at 25°C, followed by overnight digestion with trypsin at a ratio of 1:75 at 25°C. Digestion was stopped by adding trifluoroacetic acid to a final concentration of 5%, followed by centrifugation to remove precipitated detergent. Peptides were purified using SDR StageTips preconditioned with methanol and equilibrated with buffer A (0.1% formic acid in water) and buffer B (0.1% formic acid in 80% acetonitrile). Samples were washed and eluted according to the facility protocol, then stored at 4 °C until LC–MS analysis.

Data Acquisition

Samples were analyzed by the CECAD Proteomics Facility on an Orbitrap Exploris 480 mass spectrometer either coupled to a Vanquish neo in reverse flow setup (all Thermo Scientific) or an Evosep One (Evosep). For analyses using a Vanquish neo, samples were loaded onto a PepMap precolumn cartridge (#160434, Thermo Scientific) before reverse-flushing onto an in-house packed 30 cm column filled with C18 material (75 µm inner

bioRxiv preprint doi: https://doi.org/10.64898/2026.08.21.746212; this version posted August 24, 2026. The copyright holder for this preprint (which was not certified by peer review) is the author/funder, who has granted bioRxiv a license to display the preprint in perpetuity. It is made available under a CC-BY-NC-ND 4.0 International license.

diameter, filled with Agilent Poroshell). Samples were separated on a 90 min gradient running eluent A (0.1% formic acid) against eluent B (80% acetonitrile + 0.1% formic acid) on a linear gradient between 4% and 98% B. Alternatively, samples were loaded onto Evotips and analyzed using the 30 SPD method with vendor-recommended column on the Evosep One. The mass spectrometer was operated in data-independent acquisition mode with MS1 scans acquired from 399 m/z to 1001 m/z, MS2 scans ranged from 400 m/z to 1000 m/z. Both MS1 and MS2 scans were acquired at 15k or 30k resolution, respectively, with maximum injection times set to allow maximal parallelization. AGC targets for MS2 were set to 1000% and MS2 scans were acquired either in 60 x 10 m/z or 30 x 20 m/z windows with an overlap of 1 m/z. All scans were stored as centroid.

For the Gas-phase fractionated library[59], a pool generated from all samples was analyzed in six individual runs covering the range from 400 m/z to 1000 m/z in 100 m/z increments using identical LC settings as the samples. For each run, MS1 was acquired at 60k resolution with a maximum injection time of 98 ms and an AGC target of 100%. MS2 spectra were acquired at 30k resolution with a maximum injection time of 60 ms. Spectra were acquired in staggered 4 m/z windows, resulting in nominal 2 m/z windows after deconvolution using ProteoWizard[60].

Sample Processing in DIA-NN

The gas-phase fractionated library was built using DIA-NN 1.8.1[61] using a Swissprot *E. coli* canonical database (downloaded 04/01/2023 and 15/01/2025, respectively) with settings matching acquisition parameters. DIA-NN was run with the additional command line prompts “—report-lib-info” and “—relaxed-prot-inf”. Further output settings were: filtered at 0.01 FDR, N-terminal methionine excision enabled, maximum number of missed cleavages set to 1, min peptide length set to 7, max peptide length set to 30, min precursor m/z set to 400, max precursor m/z set to 1000, cysteine carbamidomethylation enabled as a fixed modification. Finally, acquired sample files were searched against the GPF library or, alternatively, library-free using the match-between-runs option in DIA-NN. Afterwards, DIA-NN output was further filtered on library q-value and global q-value <= 0.01 and at least one unique peptides per protein using R (4.1.3). The mass spectrometry proteomics data have been deposited to the ProteomeXchange Consortium via the PRIDE partner repository[62] with the dataset identifier PXD082778.

Quantitative protein abundance analysis

Peptide abundances were aggregated into protein abundances using the xTop v2 algorithm as detailed in[14]. Protein molecular weights were obtained from UniProt and used to convert protein abundances into proteome mass fractions by multiplying each protein abundance by

bioRxiv preprint doi: https://doi.org/10.64898/2026.08.21.746212; this version posted August 24, 2026. The copyright holder for this preprint (which was not certified by peer review) is the author/funder, who has granted bioRxiv a license to display the preprint in perpetuity. It is made available under a CC-BY-NC-ND 4.0 International license.

its corresponding molecular weight and normalizing by the total summed protein mass. To determine absolute proteome mass fractions, we included calibration conditions for which ribosome profiling reference data are available[39] in the dataset. Protein abundances were scaled to these reference conditions following the calibration procedure described in[14]. Proteins were assigned to proteome sectors as previously described[40]. The flask dataset exhibited a global median coefficient of variation (CV) of approximately 14%, while replicated anchor conditions in the mini-bioreactor dataset exhibited a comparable median CV of approximately 16%. Samples with biological replicates were averaged, while conditions without replicates are represented by a single measurement. The number of replicates is indicated in the column headings of Tables S1 and S2.

Global proteome analysis

Protein abundances for each drug combination condition were normalized to the corresponding untreated condition. Prior to downstream analysis, proteins containing missing values or zero abundances across analyzed conditions were excluded. Relative protein abundances were transformed into $\log_2$ fold changes relative to the untreated condition. For principal component analysis (PCA), protein abundance profiles were standardized using `sklearn.preprocessing.StandardScaler`. PCA was subsequently performed using `sklearn.decomposition.PCA` to identify dominant axes of proteome variation across drug-treatment conditions. To determine which functional groups contributed the most to each principal component, proteins were grouped by their level-2 annotation. For each group, squared PC scores were summed and normalized to the total squared scores of all level-2 annotated proteins. Positive and negative scores were considered separately to preserve the direction of the contribution. Drug concentrations were normalized by their IC_{50}, determined from single-drug dose-response measurements using a Hill function fitted with `scipy.optimize.curve_fit`:

$$y(c) = \frac{1}{1 + \left(\frac{c}{\mathrm{IC}_{50}}\right)^{n}}$$

where c denotes drug concentration, IC_{50} the half-maximal inhibitory concentration, and n the Hill coefficient.

Continuous response surfaces for growth rate, principal component scores, and individual protein abundances were reconstructed on dense, regular grids using `numpy.meshgrid` and piecewise linear interpolation with `scipy.interpolate.griddata` (`method="linear"`). Interpolation was performed in IC_{50}-normalized concentration space and restricted to the convex hull of experimentally measured conditions to avoid

bioRxiv preprint doi: https://doi.org/10.64898/2026.08.21.746212; this version posted August 24, 2026. The copyright holder for this preprint (which was not certified by peer review) is the author/funder, who has granted bioRxiv a license to display the preprint in perpetuity. It is made available under a CC-BY-NC-ND 4.0 International license.

extrapolation beyond sampled concentration regions. Isoboles corresponding to constant growth inhibition levels were extracted from interpolated growth surfaces and plotted as a function of the relative drug fraction $x_A = \frac{c_A/\mathrm{IC}_{50,A}}{c_A/\mathrm{IC}_{50,A}+c_B/\mathrm{IC}_{50,B}}$ (Figs. 4B,D,E and Fig. S5F) .

Protein trajectories along isoboles were analyzed using both linear and sigmoidal models. Linear trajectories were fitted using ordinary least-squares regression implemented with `scipy.stats.linregress`. The linear fits were then evaluated using the coefficient of determination (R^2), slope directionality, and monotonicity along the analyzed trajectories. Sigmoidal trajectories were fitted using `scipy.optimize.curve_fit` and a hyperbolictangent function:

$$y(x) = y_0 + \tanh\left(\frac{x-x_0}{w}\right)$$

where y_0 denotes the baseline level, h the transition amplitude, x_0 the midpoint position, and w the transition width parameter. Model quality was evaluated using the coefficient of determination (R^2) and the Akaike Information Criterion (AIC). We compared AIC values between sigmoidal and linear fits to assess if the sigmoidal fits substantially improved the description of the data. Proteins were classified only if at least five valid data points were available along the analyzed isobole and if the dynamic range exceeded 0.30 $\log_2$ fold-change units. Proteins were classified as sigmoidal if they satisfied all of the following criteria: $R^2 \geq 0.90$ for the sigmoidal fit, $\Delta\mathrm{AIC} \geq 4$ compared to the linear model, transition width $w < 0.40$, and midpoint position $0.45 \leq x_0 \leq 0.55$. Proteins were classified as linear if they satisfied the following criteria: linear fit quality $R^2 \geq 0.90$ and monotonic fraction ≥ 0.6. The monotonic fraction was defined as the fraction of neighboring steps along the isobole that followed the dominant direction of change. Proteins not fulfilling these criteria were classified as unassigned. To reduce computational costs during large-scale fitting, proteins exhibiting highly linear behavior (linear $R^2 > 0.97$) were optionally excluded from additional sigmoidal fitting steps.

bioRxiv preprint doi: https://doi.org/10.64898/2026.08.21.746212; this version posted August 24, 2026. The copyright holder for this preprint (which was not certified by peer review) is the author/funder, who has granted bioRxiv a license to display the preprint in perpetuity. It is made available under a CC-BY-NC-ND 4.0 International license.

Candidate emergent-response examples

To identify possible emergent responses, protein trajectories along the analyzed isobole were screened for proteins with higher abundance in the mixed-drug region than at both single-drug ends. The single-drug edge regions were defined as relative drug fractions $x \leq 0.15$ and $x \geq 0.85$, and the mixed-drug region as $0.35 \leq x \leq 0.65$. Candidate proteins were required to have at least five valid data points, edge values close to baseline, and a higher maximum $\log_2$ fold-change in the mixed-drug region than at either edge. The four clearest candidates were selected for visualization in Fig. S5D, but because this behavior was weak and inconsistent across the dataset, they were treated as illustrative examples rather than as a robust emergent-response class.

Quantification of drug interactions

Drug interactions were quantified using the logarithmic Loewe interaction score, LI_{log}, following the volume-based definition of Kavčič *et al.*[2]. For each antibiotic pair, the Loewe-additive response surface, $y_{\mathrm{add}}(c_A, c_B)$, was reconstructed from the normalized single-drug dose-response curves. At each concentration pair, the additive growth response $y(c_A, c_B)$ was determined by solving

$$\frac{c_A}{D_A(y)} + \frac{c_B}{D_B(y)} = 1,$$

where $D_i(y)$ is the concentration of drug *i* required to produce the normalized growth response *y*. Within each analysis, the measured or model-predicted response surface and its corresponding additive surface were integrated over identical points in two-dimensional concentration space. The interaction score was calculated as

$$\mathrm{LI}_{\log} = \ln\left[\frac{\iint y\,(c_A, c_B)\mathrm{d}c_A\mathrm{d}c_B}{\iint y_{\mathrm{add}}\,(c_A, c_B)\mathrm{d}c_A\mathrm{d}c_B}\right]$$

Experimental surfaces were integrated over the original measured concentration grid using weights determined by the spacing between concentrations, with missing values excluded. Model surfaces were evaluated on an 80×80 grid spanning 0–1.6×IC_{50} along both drug axes. Positive LI_{log} values indicate antagonism, negative values indicate synergy, and values close to zero indicate additivity.

Numerical solutions

We evaluated the steady-state solutions of the one- and two-drug models described in the Supplementary Text by directly solving the corresponding cubic equation for the growth rate λ. All roots were calculated using `numpy.roots`, and only real roots within the physically admissible range $0 \leq \lambda \leq \lambda_0$ were retained. At zero drug concentration, the largest admissible

bioRxiv preprint doi: https://doi.org/10.64898/2026.08.21.746212; this version posted August 24, 2026. The copyright holder for this preprint (which was not certified by peer review) is the author/funder, who has granted bioRxiv a license to display the preprint in perpetuity. It is made available under a CC-BY-NC-ND 4.0 International license.

root was selected. At subsequent concentrations, the root closest to the preceding solution was chosen to follow a continuous solution branch. Growth was normalized by the drug-free growth rate, $y=\lambda/\lambda_{00}$, and the model IC_{50} was determined by interpolation at $y=0.5$.

For the two-drug model, the transcription inhibitor X established a concentration-dependent background growth rate, $\lambda_0(c_X) = \lambda_{00} g_X(c_X)$, described by a normalized Hill function with $IC_{50,X}=0.7$ and Hill coefficient $n_X=2$. At each concentration of drug X, the effective ribosome range was recalculated according to the generalized growth law, and the steady-state equation was solved over increasing concentrations of the translation inhibitor Y. We used $\kappa_t=0.061\mu M^{-1}h^{-1}$, $r_{min}=19.3\mu M$, $\Delta r=46.5\mu M$, and $\lambda_{00}=0.85h^{-1}$; the remaining kinetic parameters were set as described in the Supplementary Text. Two-dimensional response surfaces were calculated for $\theta=1$ and $\theta=0$, representing strong and weak ribosome upregulation, respectively. For Fig. S4A, one-dimensional dose-response curves were calculated for $\theta=-0.4$, 0, and 1, with concentrations normalized by the IC_{50} of the $\theta=0$ response.

Data Availability

Source data are provided with this paper. Proteomics raw data files have been uploaded to ProteomeXchange under the study accession code PXD082778. Proteome sectors and slopes of conditions are provided in the Supplementary Information (Table S1). Also provided in the Supplementary Information are the expression levels of all detected proteins in all conditions investigated here (Table S2).

Code Availability

This study did not produce any new computer code, except for a few Python 3 scripts used for data analysis and exploration. All codes are available from the corresponding author upon request.

References

1. Greulich, P., Scott, M., Evans, M. R. & Allen, R. J. Growth-dependent bacterial susceptibility to ribosome-targeting antibiotics. *Mol Syst Biol* **11**, MSB145949 (2015).
2. Kavčič, B., Tkačik, G. & Bollenbach, T. Mechanisms of drug interactions between translation-inhibiting antibiotics. *Nat Commun* **11**, 4013 (2020).
3. Kavčič, B., Tkačik, G. & Bollenbach, T. Minimal biophysical model of combined antibiotic action. *PLoS Comput Biol* **17**, e1008529 (2021).

bioRxiv preprint doi: https://doi.org/10.64898/2026.08.21.746212; this version posted August 24, 2026. The copyright holder for this preprint (which was not certified by peer review) is the author/funder, who has granted bioRxiv a license to display the preprint in perpetuity. It is made available under a CC-BY-NC-ND 4.0 International license.

4. Droghetti, R. *et al.* Hands-On Growth Laws Theory Cookbook. *PRX Life* **4**, 012001 (2026).
5. Scott, M., Gunderson, C. W., Mateescu, E. M., Zhang, Z. & Hwa, T. Interdependence of Cell Growth and Gene Expression: Origins and Consequences. *Science* **330**, 1099–1102 (2010).
6. Schaechter, M., Maaløe, O. & Kjeldgaard, N. O. Dependency on Medium and Temperature of Cell Size and Chemical Composition during Balanced Growth of Salmonella typhimurium. *Journal of General Microbiology* **19**, 592–606 (1958).
7. Bremer, H. & Dennis, P. P. Modulation of Chemical Composition and Other Parameters of the Cell at Different Exponential Growth Rates. *EcoSal Plus* **3**, 10.1128/ecosal.5.2.3 (2008).
8. Dennis, P. P. & Bremer, H. Macromolecular Composition During Steady-State Growth of *Escherichia coli* B/r. *J Bacteriol* **119**, 270–281 (1974).
9. Scott, M. & Hwa, T. Bacterial growth laws and their applications. *Current Opinion in Biotechnology* **22**, 559–565 (2011).
10. Matamouros, S. *et al.* Growth-rate dependency of ribosome abundance and translation elongation rate in Corynebacterium glutamicum differs from that in Escherichia coli. *Nat Commun* **14**, 5611 (2023).
11. Wilson, D. N. Ribosome-targeting antibiotics and mechanisms of bacterial resistance. *Nat Rev Microbiol* **12**, 35–48 (2014).
12. Blanchard, S. C., Cooperman, B. S. & Wilson, D. N. Probing Translation with Small-Molecule Inhibitors. *Chemistry & Biology* **17**, 633–645 (2010).
13. Neidhardt, F. C. & Magasanik, B. Studies on the role of ribonucleic acid in the growth of bacteria. *Biochimica et Biophysica Acta* **42**, 99–116 (1960).
14. Mori, M. *et al.* From coarse to fine: the absolute Escherichia coli proteome under diverse growth conditions. *Mol Syst Biol* **17**, MSB20209536 (2021).
15. Hui, S. *et al.* Quantitative proteomic analysis reveals a simple strategy of global resource allocation in bacteria. *Mol Syst Biol* **11**, MSB145697 (2015).

bioRxiv preprint doi: https://doi.org/10.64898/2026.08.21.746212; this version posted August 24, 2026. The copyright holder for this preprint (which was not certified by peer review) is the author/funder, who has granted bioRxiv a license to display the preprint in perpetuity. It is made available under a CC-BY-NC-ND 4.0 International license.

16. Basan, M. *et al.* Overflow metabolism in Escherichia coli results from efficient proteome allocation. *Nature* **528**, 99–104 (2015).
17. Deris, J. B. *et al.* The Innate Growth Bistability and Fitness Landscapes of Antibiotic-Resistant Bacteria. *Science* **342**, 1237435 (2013).
18. Elf, J., Nilsson, K., Tenson, T. & Ehrenberg, M. Bistable Bacterial Growth Rate in Response to Antibiotics with Low Membrane Permeability. *Phys. Rev. Lett.* **97**, 258104 (2006).
19. Frenkel, N., Saar Dover, R., Titon, E., Shai, Y. & Rom-Kedar, V. Bistable Bacterial Growth Dynamics in the Presence of Antimicrobial Agents. *Antibiotics* **10**, 87 (2021).
20. Loewe, S. Die quantitativen Probleme der Pharmakologie. *Ergebnisse der Physiologie* **27**, 47–187 (1928).
21. Bollenbach, T. Antimicrobial interactions: mechanisms and implications for drug discovery and resistance evolution. *Current Opinion in Microbiology* **27**, 1–9 (2015).
22. Yeh, P., Tschumi, A. I. & Kishony, R. Functional classification of drugs by properties of their pairwise interactions. *Nat Genet* **38**, 489–494 (2006).
23. Roemhild, R., Bollenbach, T. & Andersson, D. I. The physiology and genetics of bacterial responses to antibiotic combinations. *Nat Rev Microbiol* **20**, 478–490 (2022).
24. Lázár, V., Snitser, O., Barkan, D. & Kishony, R. Antibiotic combinations reduce Staphylococcus aureus clearance. *Nature* **610**, 540–546 (2022).
25. Fatsis-Kavalopoulos, N., Roemhild, R., Tang, P.-C., Kreuger, J. & Andersson, D. I. CombiANT: Antibiotic interaction testing made easy. *PLoS Biol* **18**, e3000856 (2020).
26. Brochado, A. R. *et al.* Species-specific activity of antibacterial drug combinations. *Nature* **559**, 259–263 (2018).
27. Zhang, Q. *et al.* A Decrease in Transcription Capacity Limits Growth Rate upon Translation Inhibition. *mSystems* **5**, e00575-20 (2020).
28. Balakrishnan, R. *et al.* Principles of gene regulation quantitatively connect DNA to RNA and proteins in bacteria. *Science* **378**, eabk2066 (2022).

bioRxiv preprint doi: https://doi.org/10.64898/2026.08.21.746212; this version posted August 24, 2026. The copyright holder for this preprint (which was not certified by peer review) is the author/funder, who has granted bioRxiv a license to display the preprint in perpetuity. It is made available under a CC-BY-NC-ND 4.0 International license.

29. Wu, C. *et al.* Cellular perception of growth rate and the mechanistic origin of bacterial growth law. *Proc. Natl. Acad. Sci. U.S.A.* **119**, e2201585119 (2022).
30. Calabrese, L., Ciandrini, L. & Cosentino Lagomarsino, M. How total mRNA influences cell growth. *Proc. Natl. Acad. Sci. U.S.A.* **121**, e2400679121 (2024).
31. Espinosa, R., Sørensen, M. A. & Svenningsen, S. L. Escherichia coli protein synthesis is limited by mRNA availability rather than ribosomal capacity during phosphate starvation. *Front. Microbiol.* **13**, 989818 (2022).
32. Campbell, E. A. *et al.* Structural Mechanism for Rifampicin Inhibition of Bacterial RNA Polymerase. *Cell* **104**, 901–912 (2001).
33. Si, F. *et al.* Invariance of Initiation Mass and Predictability of Cell Size in Escherichia coli. *Current Biology* **27**, 1278–1287 (2017).
34. Roy, A., Goberman, D. & Pugatch, R. A unifying autocatalytic network-based framework for bacterial growth laws. *Proc Natl Acad Sci U S A* **118**, e2107829118 (2021).
35. Geva-Zatorsky, N. *et al.* Protein Dynamics in Drug Combinations: a Linear Superposition of Individual-Drug Responses. *Cell* **140**, 643–651 (2010).
36. Bollenbach, T. & Kishony, R. Resolution of Gene Regulatory Conflicts Caused by Combinations of Antibiotics. *Molecular Cell* **42**, 413–425 (2011).
37. Lukačišin, M. & Bollenbach, T. Emergent Gene Expression Responses to Drug Combinations Predict Higher-Order Drug Interactions. *Cell Systems* **9**, 423-433.e3 (2019).
38. Russo, C. J., Husain, K. & Murugan, A. Soft Modes as a Predictive Framework for Low-Dimensional Biological Systems Across Scales. *Annual Review of Biophysics* **54**, 401–426 (2025).
39. Li, G.-W., Burkhardt, D., Gross, C. & Weissman, J. S. Quantifying Absolute Protein Synthesis Rates Reveals Principles Underlying Allocation of Cellular Resources. *Cell* **157**, 624–635 (2014).

bioRxiv preprint doi: https://doi.org/10.64898/2026.08.21.746212; this version posted August 24, 2026. The copyright holder for this preprint (which was not certified by peer review) is the author/funder, who has granted bioRxiv a license to display the preprint in perpetuity. It is made available under a CC-BY-NC-ND 4.0 International license.

40. Zhu, M., Mori, M., Hwa, T. & Dai, X. Distantly related bacteria share a rigid proteome allocation strategy with flexible enzyme kinetics. *Proc. Natl. Acad. Sci. U.S.A.* **122**, e2427091122 (2025).
41. Dai, X. *et al.* Reduction of translating ribosomes enables Escherichia coli to maintain elongation rates during slow growth. *Nat Microbiol* **2**, 16231 (2016).
42. Tritton, T. R. Ribosome-tetracycline interactions. *Biochemistry* **16**, 4133–4138 (1977).
43. Davies, J. & Davis, B. D. Misreading of Ribonucleic Acid Code Words Induced by Aminoglycoside Antibiotics. *Journal of Biological Chemistry* **243**, 3312–3316 (1968).
44. Schluenzen, F. *et al.* The antibiotic kasugamycin mimics mRNA nucleotides to destabilize tRNA binding and inhibit canonical translation initiation. *Nat Struct Mol Biol* **13**, 871–878 (2006).
45. Eaton, D. S. *et al.* Essentialome-Wide Multigenerational Imaging Reveals Mechanistic Origins of Cell Growth Laws. Preprint at https://doi.org/10.1101/2025.06.10.658525 (2025).
46. Zhu, M., Mori, M., Hwa, T. & Dai, X. Disruption of transcription–translation coordination in Escherichia coli leads to premature transcriptional termination. *Nat Microbiol* **4**, 2347–2356 (2019).
47. Karp, P. D. *et al.* The EcoCyc database (2025). *EcoSal Plus* **13**, eesp-0019-2024 (2025).
48. Qi, Q., Angermayr, S. A. & Bollenbach, T. Uncovering Key Metabolic Determinants of the Drug Interactions Between Trimethoprim and Erythromycin in Escherichia coli. *Front. Microbiol.* **12**, 760017 (2021).
49. Keseler, I. M. *et al.* EcoCyc: A comprehensive view of Escherichia coli biology. *Nucleic Acids Research* **37**, D464–D470 (2009).
50. Hauryliuk, V., Atkinson, G. C., Murakami, K. S., Tenson, T. & Gerdes, K. Recent functional insights into the role of (p)ppGpp in bacterial physiology. *Nat Rev Microbiol* **13**, 298–309 (2015).
51. Irving, S. E., Choudhury, N. R. & Corrigan, R. M. The stringent response and physiological roles of (pp)pGpp in bacteria. *Nat Rev Microbiol* **19**, 256–271 (2021).

bioRxiv preprint doi: https://doi.org/10.64898/2026.08.21.746212; this version posted August 24, 2026. The copyright holder for this preprint (which was not certified by peer review) is the author/funder, who has granted bioRxiv a license to display the preprint in perpetuity. It is made available under a CC-BY-NC-ND 4.0 International license.

52. Potrykus, K. & Cashel, M. (p)ppGpp: Still Magical? *Annu. Rev. Microbiol.* **62**, 35–51 (2008).

53. Ripamonti, A., Lacassin, M., Droghetti, R., Bokinsky, G. & Cosentino Lagomarsino, M. Transcriptional competition biases the effects of second messengers in Escherichia coli. *Cell Systems* **17**, 101609 (2026).

54. Tuske, S. *et al.* Inhibition of Bacterial RNA Polymerase by Streptolydigin: Stabilization of a Straight-Bridge-Helix Active-Center Conformation. *Cell* **122**, 541–552 (2005).

55. Temiakov, D. *et al.* Structural Basis of Transcription Inhibition by Antibiotic Streptolydigin. *Molecular Cell* **19**, 655–666 (2005).

56. Hughes, J. & Mellows, G. Inhibition of Isoleucyl-Transfer Ribonucleic Acid Synthetase in Escherichia coli by Pseudomonic Acid. **176**, (1978).

57. Nathans, D. PUROMYCIN INHIBITION OF PROTEIN SYNTHESIS: INCORPORATION OF PUROMYCIN INTO PEPTIDE CHAINS. *Proc. Natl. Acad. Sci. U.S.A.* **51**, 585–592 (1964).

58. Thiermann, R. *et al.* Decoupling of global metabolic flux and proteome partitioning in bacteria. *Science* **392**, eaeb6410 (2026).

59. Searle, B. C. *et al.* Generating high quality libraries for DIA MS with empirically corrected peptide predictions. *Nat Commun* **11**, 1548 (2020).

60. Chambers, M. C. *et al.* A cross-platform toolkit for mass spectrometry and proteomics. *Nat Biotechnol* **30**, 918–920 (2012).

61. Demichev, V., Messner, C. B., Vernardis, S. I., Lilley, K. S. & Ralser, M. DIA-NN: neural networks and interference correction enable deep proteome coverage in high throughput. *Nat Methods* **17**, 41–44 (2020).

62. Perez-Riverol, Y. *et al.* The PRIDE database at 20 years: 2025 update. *Nucleic Acids Res* **53**, D543–D553 (2025).

bioRxiv preprint doi: https://doi.org/10.64898/2026.08.21.746212; this version posted August 24, 2026. The copyright holder for this preprint (which was not certified by peer review) is the author/funder, who has granted bioRxiv a license to display the preprint in perpetuity. It is made available under a CC-BY-NC-ND 4.0 International license.

Acknowledgments

We thank the entire Bollenbach group, especially Booshini Fernando, for technical support and fruitful discussions; Marco Cosentino-Lagomarsino, Theresa Fink, Terence Hwa, and Leon Seeger for critical reading of the manuscript; and Jan- Wilm Lackmann and the whole CECAD / CMMC Proteomics Facility for technical support.

Funding

NG and TB were supported by the Deutsche Forschungsgemeinschaft (DFG, German Research Foundation - standalone grant BO 3502/2-1, project number 422345533 and SFB1310/3 - 325931972). MM acknowledges the support of the NIH through grant 1R35GM152133.

Author contributions

Conceptualization: N.G. and T.B. Investigation: N.G. Formal Analysis: N.G. and M.M. Writing – original draft: N.G. and T.B. Writing – review and editing: N.G., M.M., and T.B. Supervision: T.B. Funding acquisition: T.B.

Competing interests

The authors declare no competing interests.

bioRxiv preprint doi: https://doi.org/10.64898/2026.08.21.746212; this version posted August 24, 2026. The copyright holder for this preprint (which was not certified by peer review) is the author/funder, who has granted bioRxiv a license to display the preprint in perpetuity. It is made available under a CC-BY-NC-ND 4.0 International license.

Figures

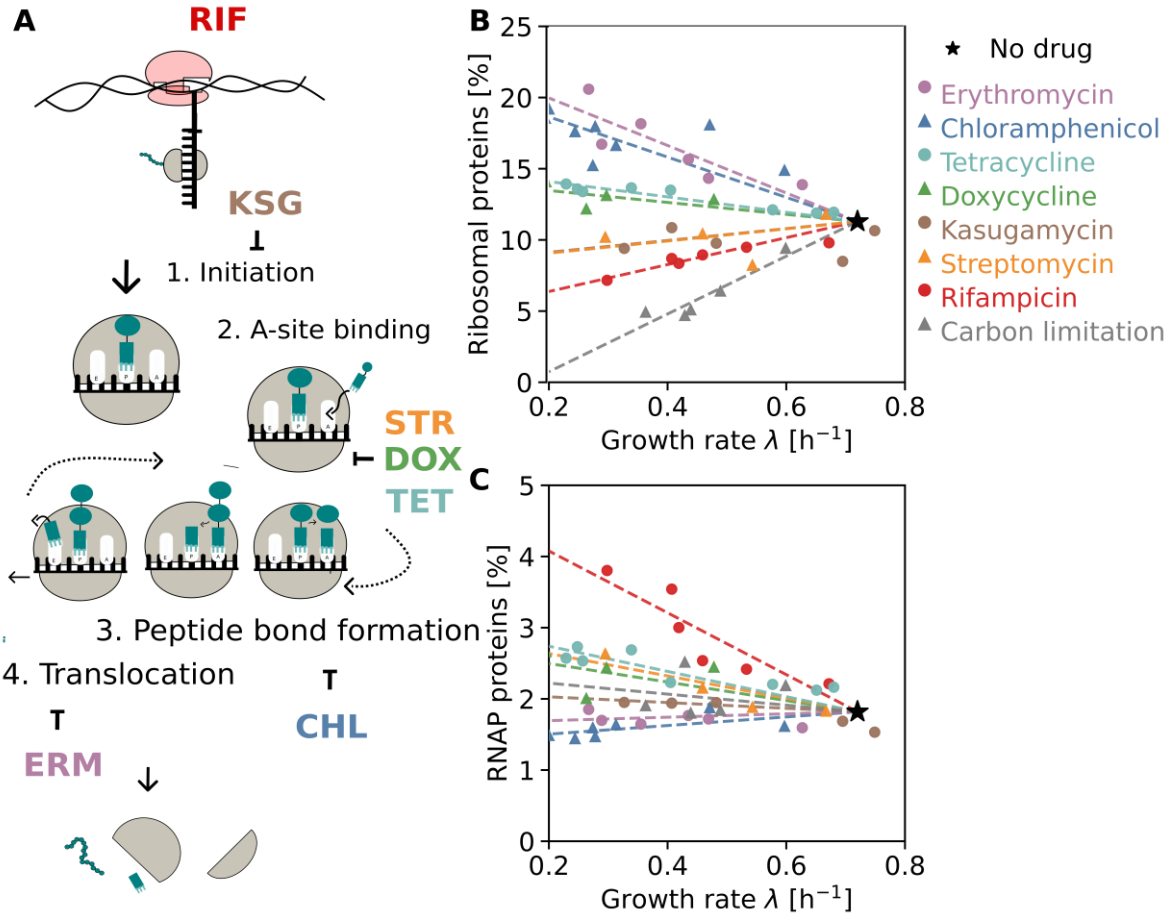


Fig. 1: Quantitative proteomics reveals drug-specific ribosome-growth relationships for translation- and transcription-targeting antibiotics.

A) Schematic overview of the primary molecular targets of the antibiotics used in this study, including diverse translation inhibitors (streptomycin, STR; doxycycline, DOX; tetracycline, TET; erythromycin, ERM; chloramphenicol, CHL, kasugamycin, KSG) and the transcription inhibitor rifampicin (RIF).

B) Ribosomal protein mass fraction as a function of growth rate under different antibiotics (colors) or carbon limitation (gray; Methods).

C) As B, but for the RNA polymerase-associated protein mass fraction (Methods).

Data in B-C were obtained from bioreactor-grown cultures (Methods).

bioRxiv preprint doi: https://doi.org/10.64898/2026.08.21.746212; this version posted August 24, 2026. The copyright holder for this preprint (which was not certified by peer review) is the author/funder, who has granted bioRxiv a license to display the preprint in perpetuity. It is made available under a CC-BY-NC-ND 4.0 International license.

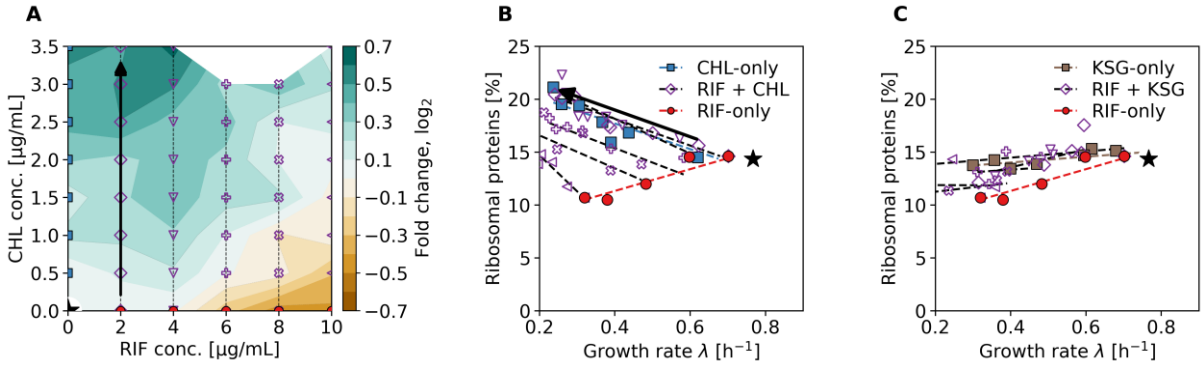


Fig. 2: Ribosome response to antibiotic combinations is a superposition of the responses to the individual drugs, suggesting a generalized growth law.

A) Heatmap of ribosomal protein abundance relative to the no-drug condition across a two-dimensional concentration gradient of rifampicin (RIF) and chloramphenicol (CHL). Black arrow indicates a trajectory of increasing chloramphenicol concentration at one fixed rifampicin level.

B) Ribosomal protein mass fraction as a function of growth rate for rifampicin-only, chloramphenicol-only, and combined rifampicin-chloramphenicol conditions at the concentrations indicated by the same symbols in A. The combined response is well approximated by a superposition of the two single-drug responses.

C) As B, but for the combination of rifampicin and kasugamycin (KSG).

Data in A-C were obtained from cultures grown in flasks (Methods).

bioRxiv preprint doi: https://doi.org/10.64898/2026.08.21.746212; this version posted August 24, 2026. The copyright holder for this preprint (which was not certified by peer review) is the author/funder, who has granted bioRxiv a license to display the preprint in perpetuity. It is made available under a CC-BY-NC-ND 4.0 International license.

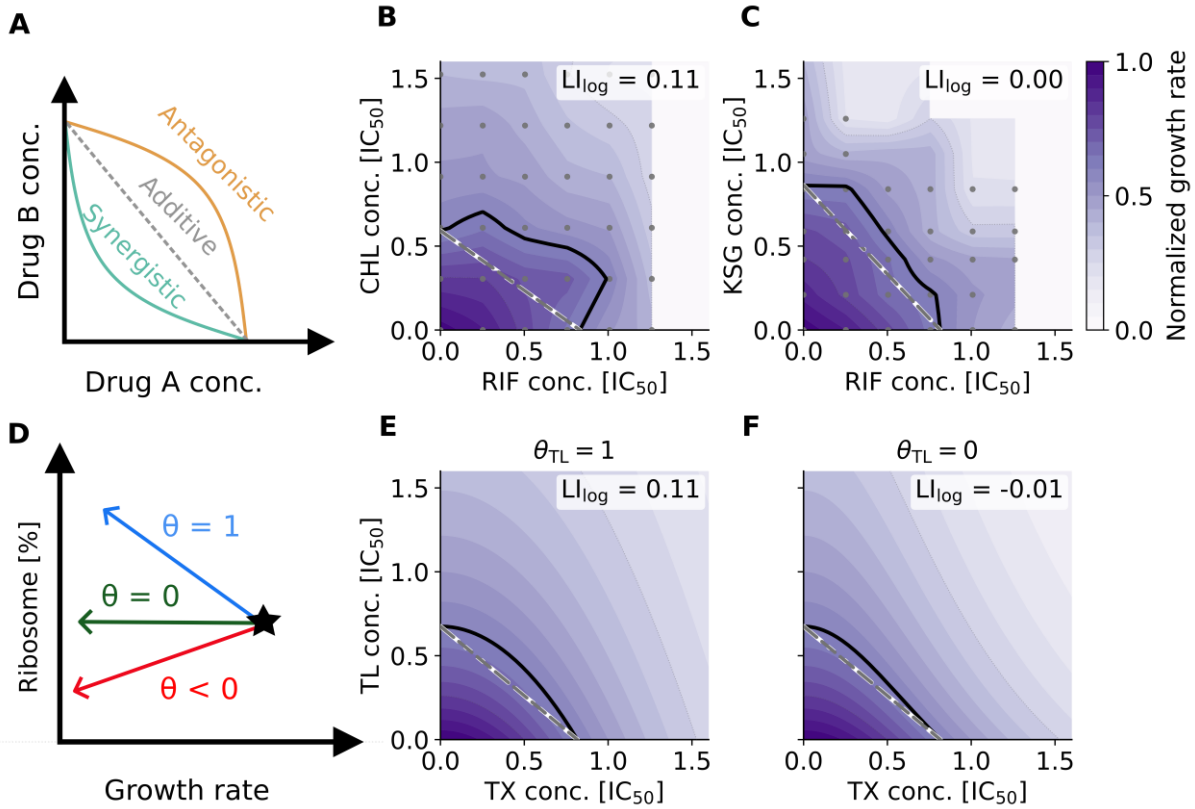


Fig. 3: A mathematical model based on the generalized growth law captures much of the observed variation in drug interactions.

A) Schematic of Loewe additivity in two-drug concentration space[20]. Lines of constant growth rate (isoboles) are shown. Straight isoboles (gray) indicate additive interactions. Concave (orange) and convex isoboles (green) indicate antagonistic and synergistic interactions, respectively.

B) Growth-rate landscape of rifampicin (RIF) and chloramphenicol (CHL) combinations in two-dimensional concentration space. The isobole at 40% growth inhibition (black line) is concave, indicating strong antagonism. The interaction score, LI_{log}=0.11, quantifies the strength of the drug interaction based on the entire landscape (Methods); LI_{log}>0 for antagonism and LI_{log}<0 for synergy. Gray points indicate the experimentally measured conditions; intermediate regions were interpolated (Methods).

C) As B, but for the combination of rifampicin and kasugamycin (KSG). The isobole remains close to the Loewe-additive expectation, indicating near-additive behavior, consistent with interaction score LI_{log}≈0.

D) Schematic representation of growth laws with different ribosome-response parameters (slopes) θ for different antibiotics targeting translation and transcription (Supplementary Text). Some translation inhibitors elicit strongly increasing ribosome allocation (θ=1), others weak ribosome responses (θ=0); transcription inhibition is captured by θ<0.

E) Growth-rate landscape for combination of a transcription inhibitor (TX) and a translation

bioRxiv preprint doi: https://doi.org/10.64898/2026.08.21.746212; this version posted August 24, 2026. The copyright holder for this preprint (which was not certified by peer review) is the author/funder, who has granted bioRxiv a license to display the preprint in perpetuity. It is made available under a CC-BY-NC-ND 4.0 International license.

inhibitor (TL) that elicits strong ribosome upregulation (θ=1), calculated from a mathematical model of bacterial growth (Methods). The model produces a clearly antagonistic interaction (LI_{log}=0.11), as observed experimentally (B).

F) As E, but for a translation inhibitor with a weak ribosome responses (θ=0). The model produces a nearly additive interaction (LI_{log}=-0.01), as observed experimentally (C).

Data in B-C were obtained from cultures grown in flasks (Methods).

bioRxiv preprint doi: https://doi.org/10.64898/2026.08.21.746212; this version posted August 24, 2026. The copyright holder for this preprint (which was not certified by peer review) is the author/funder, who has granted bioRxiv a license to display the preprint in perpetuity. It is made available under a CC-BY-NC-ND 4.0 International license.

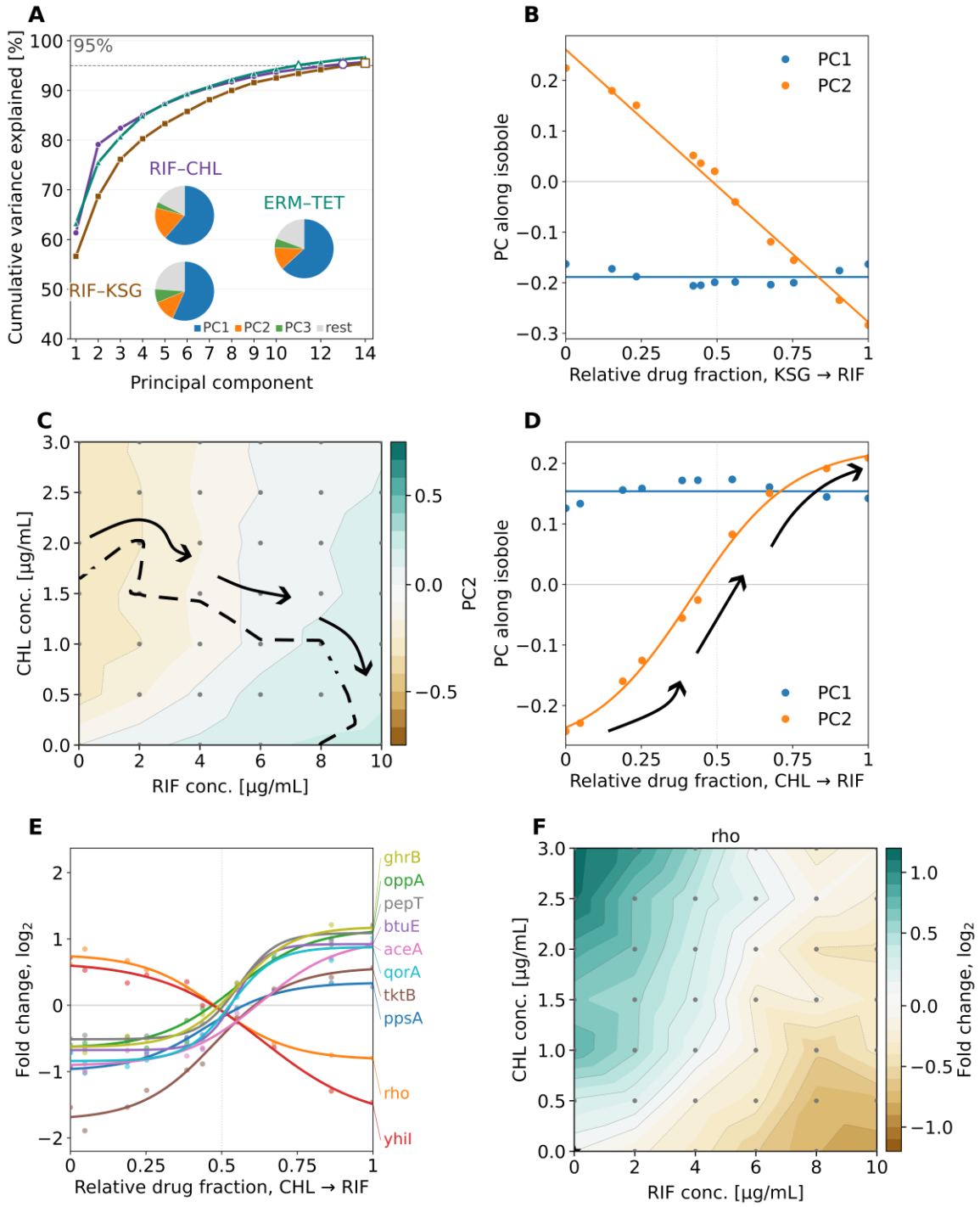


Fig. 4: Proteome response to drug combinations is captured by an interpolation of the individual drug responses.

A) Cumulative fraction of variance explained by principal component analysis (PCA) of proteome responses under the antibiotic combinations rifampicin-chloramphenicol (RIF–CHL, purple), rifampicin-kasugamycin (RIF–KSG, brown), and erythromycin-tetracycline (ERM–TET, green). The pie charts show the variance explained by the first three PCs for each dataset.

B) Principal components along the isobole at 50% growth inhibition as a function of the

bioRxiv preprint doi: https://doi.org/10.64898/2026.08.21.746212; this version posted August 24, 2026. The copyright holder for this preprint (which was not certified by peer review) is the author/funder, who has granted bioRxiv a license to display the preprint in perpetuity. It is made available under a CC-BY-NC-ND 4.0 International license.

relative drug fraction for the near-additive rifampicin-kasugamycin combination (Methods). The first PC remains approximately constant along the isobole, indicating a general growth-related response. The second PC linearly connects the two single-drug responses, indicating gradual interpolation of the conflicting proteome responses.

C) Second PC for the rifampicin-chloramphenicol combination. Dashed line shows isobole at 50% growth inhibition.

D) As B, but for the antagonistic rifampicin-chloramphenicol combination. The second PC exhibits a sigmoidal shape, indicating a more switch-like transition between the single-drug states.

E) Fold-change in expression level of representative proteins along the isobole at 50% growth inhibition for the antagonistic rifampicin-chloramphenicol combination. See Table S2 for the full dataset.

F) Fold-change in expression level of the premature transcription termination factor Rho in response to the rifampicin-chloramphenicol combination. Additional examples of individual protein responses with clear regulatory conflicts are shown in Fig. S8A-C.

Data in A-F were obtained from cultures grown in flasks (Methods).

bioRxiv preprint doi: https://doi.org/10.64898/2026.08.21.746212; this version posted August 24, 2026. The copyright holder for this preprint (which was not certified by peer review) is the author/funder, who has granted bioRxiv a license to display the preprint in perpetuity. It is made available under a CC-BY-NC-ND 4.0 International license.

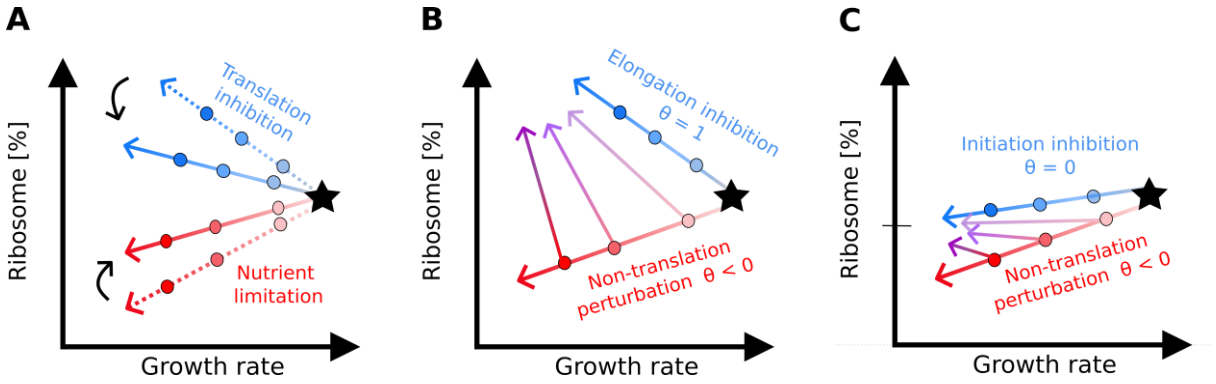


Fig. 5: A generalized growth law unifies ribosome responses across combinations of perturbations.

A) Schematic showing the first (dotted red arrow) and second bacterial growth law (dotted blue arrow). The solid lines illustrate the generalized growth law, in which the ribosome's response to a non-translation perturbation (which does not directly target translation) and its response to translation inhibition can vary.

B,C) Examples of specific predictions derived from the generalized growth law. Combining a non-translation perturbation with $\theta < 0$ such as nutrient limitation or transcription inhibition (red) with a perturbation of translation elongation ($\theta = 1$, blue) leads to ribosome responses similar to those of the second growth law, but with quantitative differences (B). Combining the non-translation perturbation with a perturbation of translation initiation or fidelity ($\theta \approx 0$) yields the ribosome responses depicted in C. These predictions generalize to perturbations with arbitrary values of θ.

bioRxiv preprint doi: https://doi.org/10.64898/2026.08.21.746212; this version posted August 24, 2026. The copyright holder for this preprint (which was not certified by peer review) is the author/funder, who has granted bioRxiv a license to display the preprint in perpetuity. It is made available under a CC-BY-NC-ND 4.0 International license.

Supporting Information

Supplementary figures

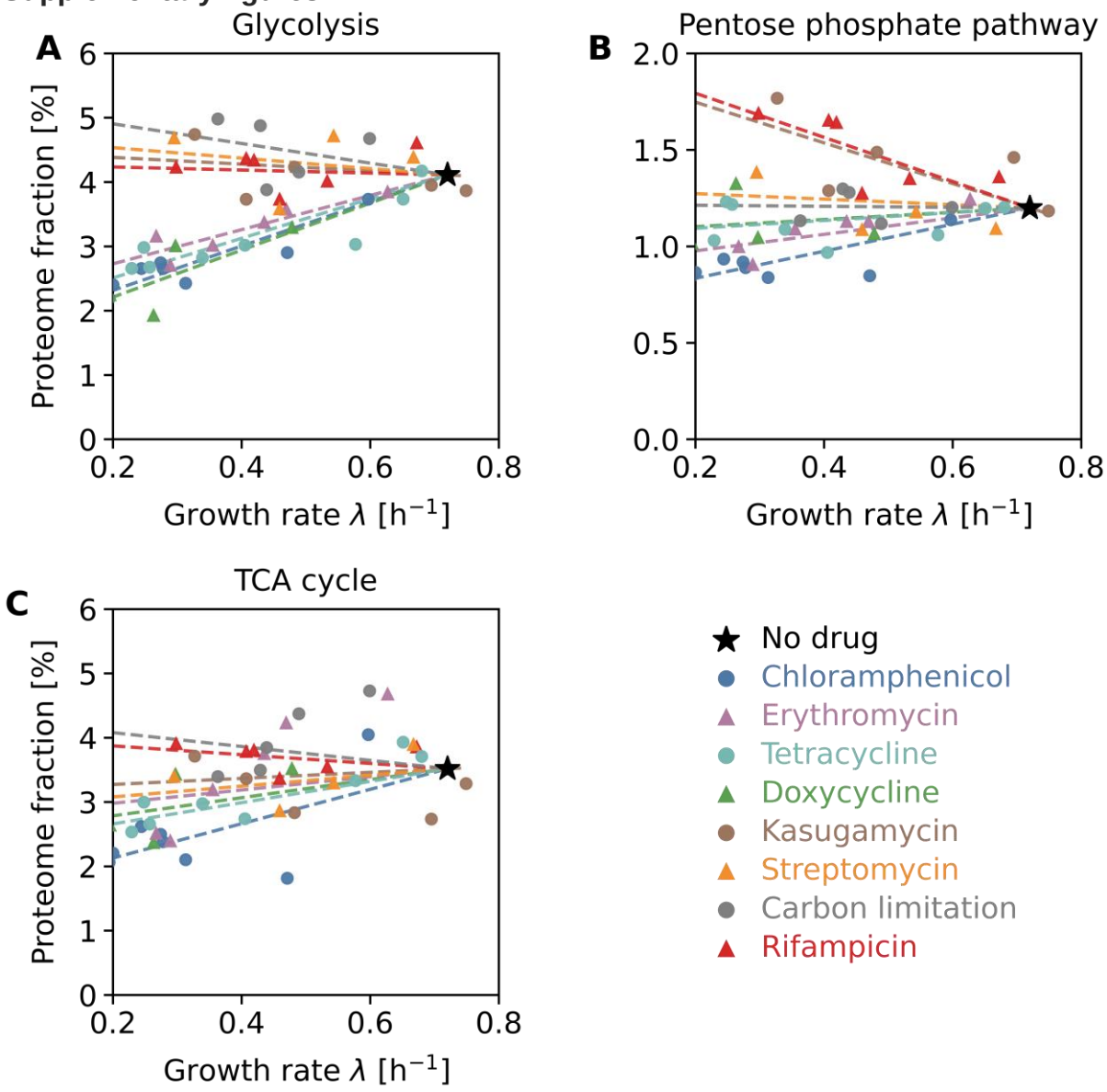


Fig. S1: Drug-specific sector responses of central carbon metabolism.

A) Glycolysis protein mass fraction as a function of growth rate under chloramphenicol (CHL), kasugamycin (KSG), rifampicin (RIF), and carbon limitation.

B) As in A, but for proteins belonging to the pentose phosphate pathway.

C) As in A and B, but for proteins belonging to TCA cycle. Data were obtained from bioreactor-grown cultures (Methods).

bioRxiv preprint doi: https://doi.org/10.64898/2026.08.21.746212; this version posted August 24, 2026. The copyright holder for this preprint (which was not certified by peer review) is the author/funder, who has granted bioRxiv a license to display the preprint in perpetuity. It is made available under a CC-BY-NC-ND 4.0 International license.

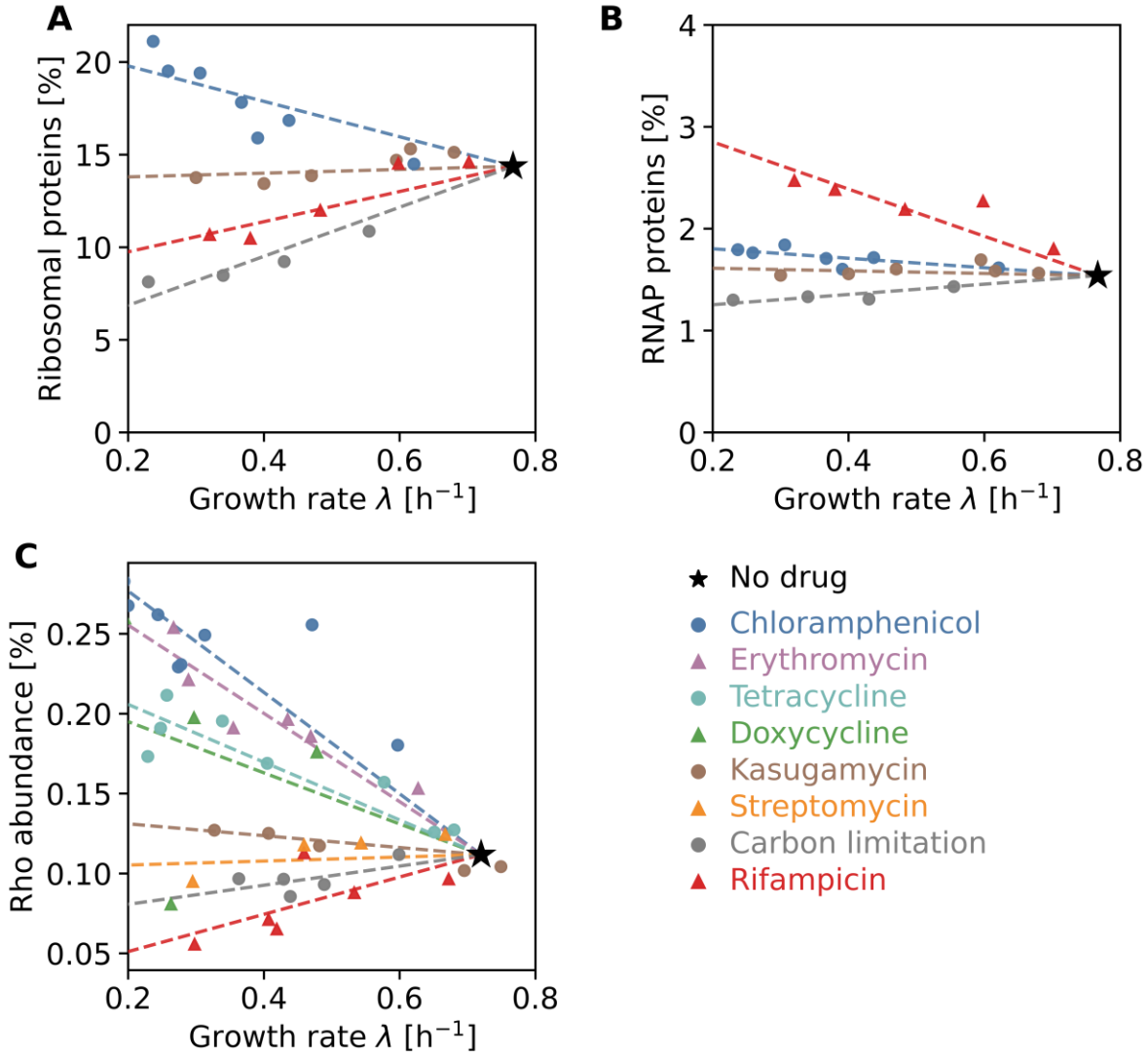


Fig. S2: Independent replicate proteomics dataset for one-dimensional gradients of antibiotics and carbon limitation.

A) Ribosomal protein mass fraction as a function of growth rate under chloramphenicol (CHL), kasugamycin (KSG), rifampicin (RIF), and carbon limitation, as in Fig. 1B, but for an independent dataset.

B) RNAP-associated protein mass fraction as in Fig. 1C, but for an independent dataset. Rifampicin increases RNAP allocation, whereas translation inhibitors produce comparatively minor changes.

C) As Fig. 1B,C, but for the transcription-termination factor Rho. Rho follows a similar trend to that of ribosomal proteins across all perturbations.

Data in A and B were obtained from cultures grown in flasks, whereas data in C were obtained from bioreactor-grown cultures (Methods).

bioRxiv preprint doi: https://doi.org/10.64898/2026.08.21.746212; this version posted August 24, 2026. The copyright holder for this preprint (which was not certified by peer review) is the author/funder, who has granted bioRxiv a license to display the preprint in perpetuity. It is made available under a CC-BY-NC-ND 4.0 International license.

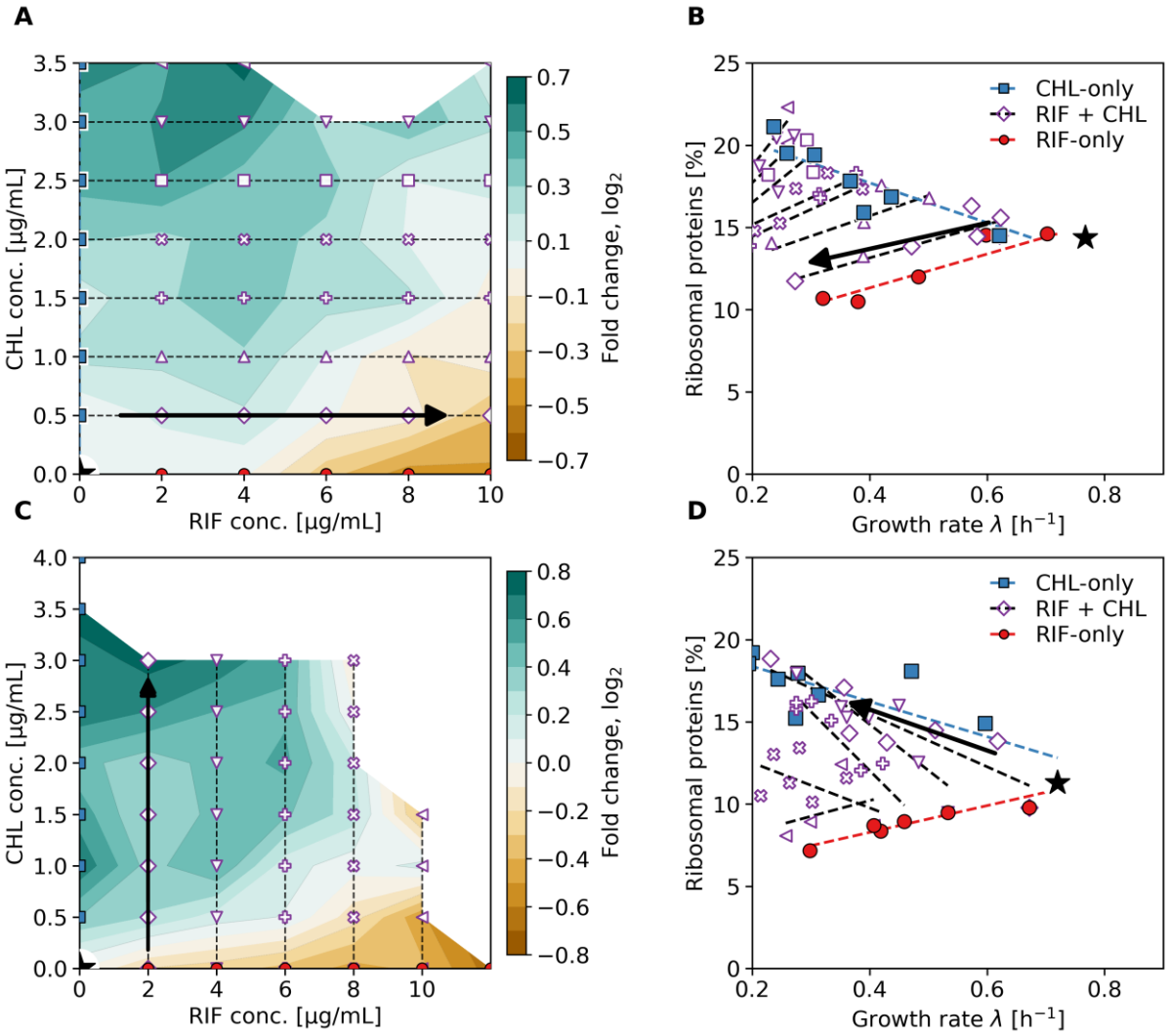


Fig. S3: Ribosome response to transcription inhibition at fixed translation inhibition and independent replicate proteomics measurement of the response to rifampicin-chloramphenicol.

A) Heatmap of ribosomal protein abundance (fold change relative to the no-drug condition) across a two-dimensional concentration gradient of rifampicin (RIF) and chloramphenicol (CHL). Black arrow indicates trajectory of increasing rifampicin concentration at a fixed chloramphenicol concentration. Ribosome allocation continuously shifts from the elevated ribosome state characteristic of chloramphenicol treatment toward the low-ribosome rifampicin state.

B) Ribosomal protein mass fraction as a function of growth rate for rifampicin-only, chloramphenicol-only, and combined rifampicin-chloramphenicol conditions at the concentrations indicated in A.

C) As Fig. 2A, but measured in an independent steady-state bioreactor dataset. Black arrow indicates trajectory of increasing chloramphenicol concentration at a fixed RIF concentration.

bioRxiv preprint doi: https://doi.org/10.64898/2026.08.21.746212; this version posted August 24, 2026. The copyright holder for this preprint (which was not certified by peer review) is the author/funder, who has granted bioRxiv a license to display the preprint in perpetuity. It is made available under a CC-BY-NC-ND 4.0 International license.

D) As Fig. 2B, but for the independent dataset in C. Combined-drug conditions interpolate between the single-drug growth-law responses, reproducing the trends observed in Fig. 2. Data in A and B were obtained from cultures grown in flasks, whereas data in C and D were obtained from bioreactor-grown cultures (Methods).

bioRxiv preprint doi: https://doi.org/10.64898/2026.08.21.746212; this version posted August 24, 2026. The copyright holder for this preprint (which was not certified by peer review) is the author/funder, who has granted bioRxiv a license to display the preprint in perpetuity. It is made available under a CC-BY-NC-ND 4.0 International license.

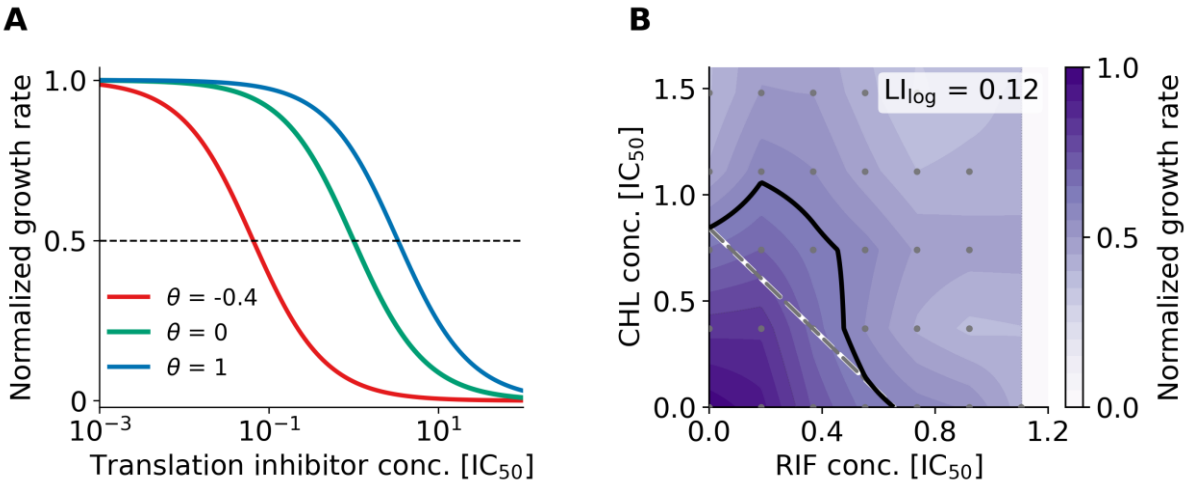


Fig. S4: Properties and independent experimental validation of the mathematical model based on the generalized growth law.

A) Dose-response curves calculated from the mathematical model for translation inhibitors with different ribosome-response parameters θ. Changing the value of θ rescales the effective drug concentration and shifts the dose-response curve horizontally without substantially altering its shape. Strong ribosome upregulation (θ=1) decreases susceptibility, whereas weak or negative ribosome responses increase susceptibility.

B) Independent bioreactor replicate of the rifampicin (RIF) and chloramphenicol (CHL) growth-response surface (Methods). The antagonistic interaction observed in Fig. 3B is reproduced. Dashed line: Loewe-additive expectation. Gray points indicate experimentally measured conditions. Data in B were obtained from bioreactor-grown-cultures (Methods).

bioRxiv preprint doi: https://doi.org/10.64898/2026.08.21.746212; this version posted August 24, 2026. The copyright holder for this preprint (which was not certified by peer review) is the author/funder, who has granted bioRxiv a license to display the preprint in perpetuity. It is made available under a CC-BY-NC-ND 4.0 International license.

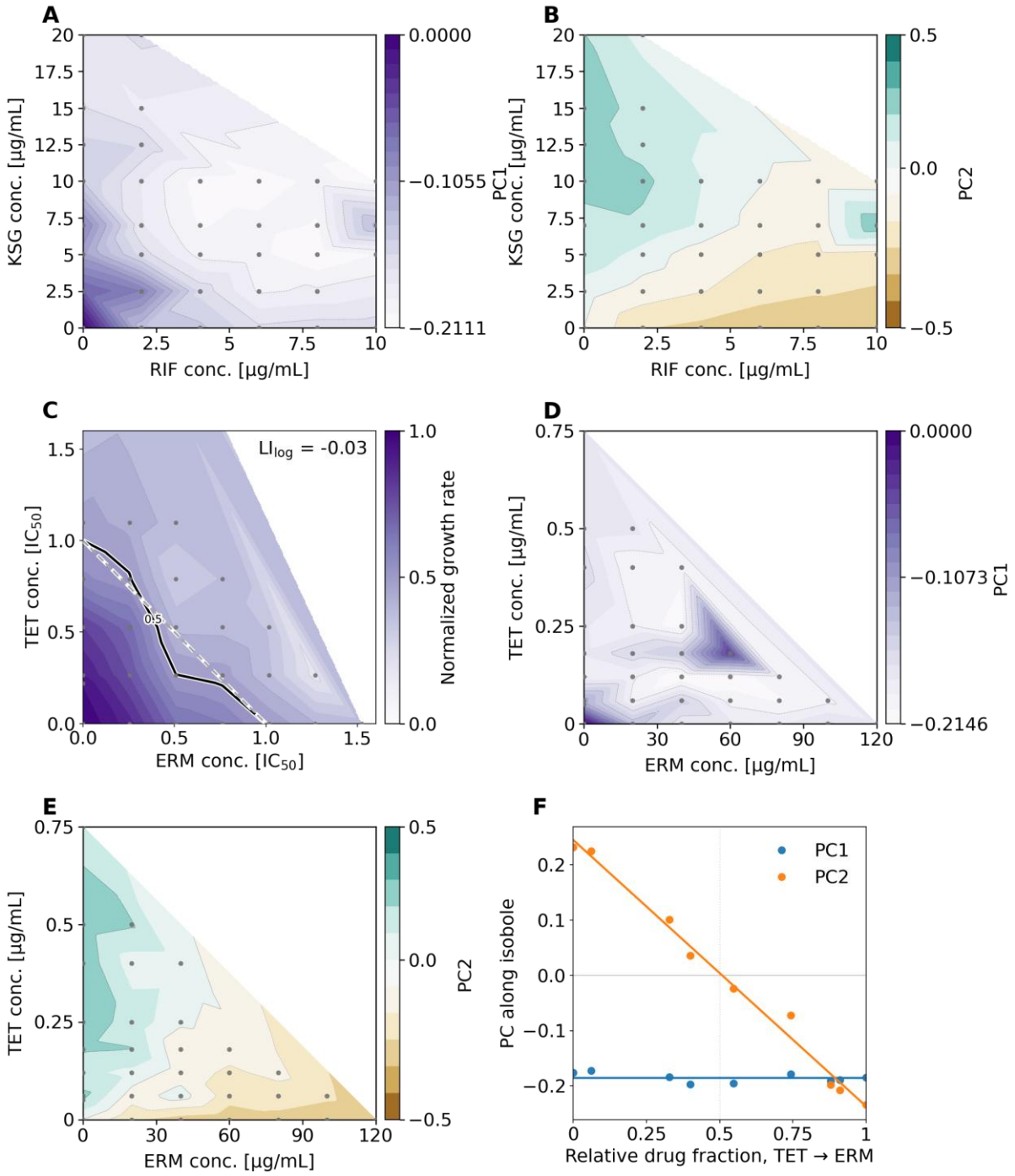


Fig. S5: Growth response surfaces and principal components of proteome responses for additive combinations of translation and transcription inhibitors.

A-B) First (A) and second (B) principal component for the rifampicin-kasugamycin (RIF-KSG) combination.

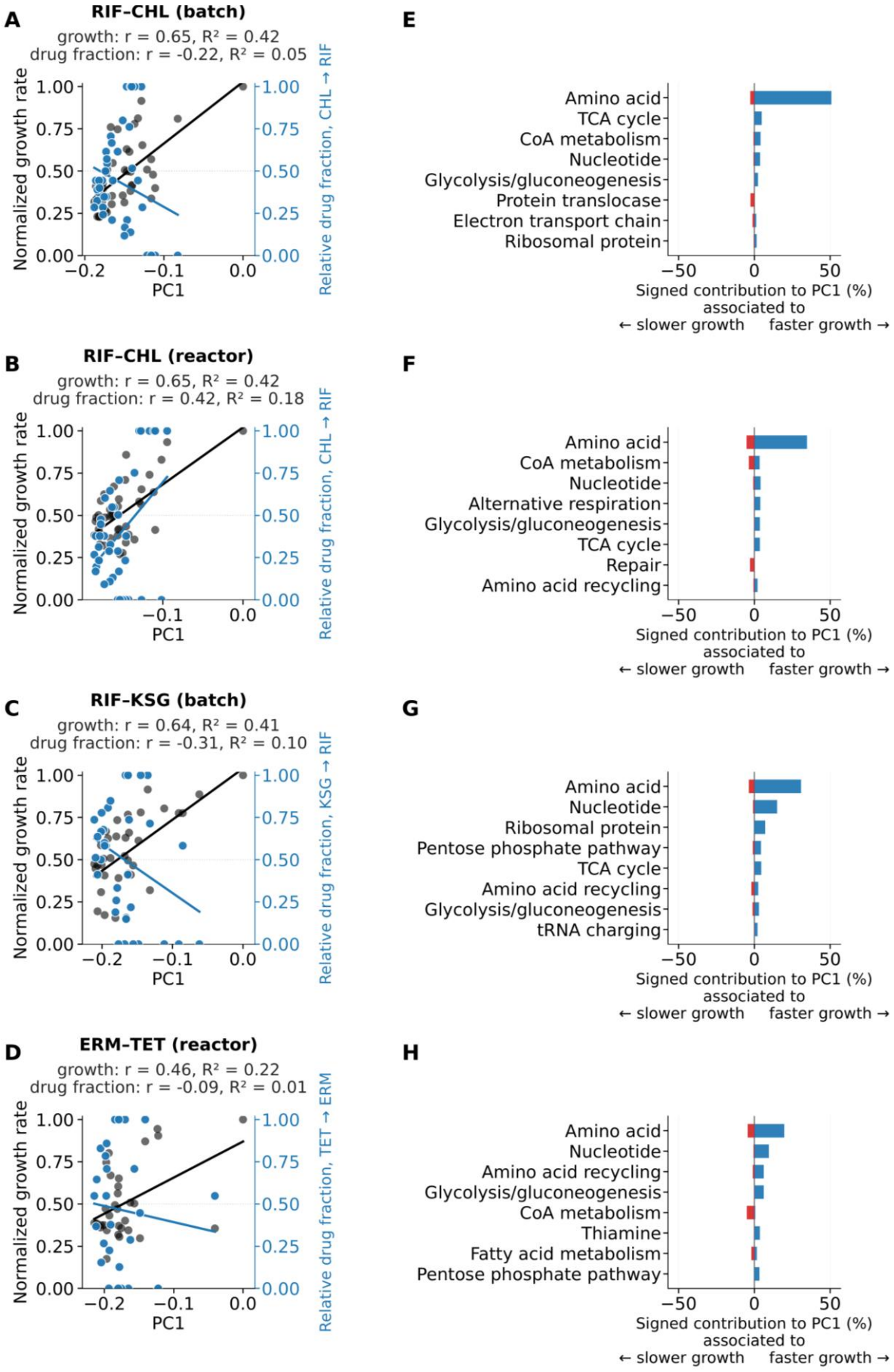
C-D) Growth-response surface (C) and first principal component (D) for the erythromycin-tetracycline (ERM-TET) combination.

E-F) Second principal component in two-dimensional concentration space (E) and along the isobole at 50% growth inhibition (F) for the erythromycin-tetracyclline combination.

bioRxiv preprint doi: https://doi.org/10.64898/2026.08.21.746212; this version posted August 24, 2026. The copyright holder for this preprint (which was not certified by peer review) is the author/funder, who has granted bioRxiv a license to display the preprint in perpetuity. It is made available under a CC-BY-NC-ND 4.0 International license.

Data in A and B were obtained from cultures grown in flasks, whereas data in C–F were obtained from bioreactor-grown cultures (Methods).

bioRxiv preprint doi: https://doi.org/10.64898/2026.08.21.746212; this version posted August 24, 2026. The copyright holder for this preprint (which was not certified by peer review) is the author/funder, who has granted bioRxiv a license to display the preprint in perpetuity. It is made available under a CC-BY-NC-ND 4.0 International license.

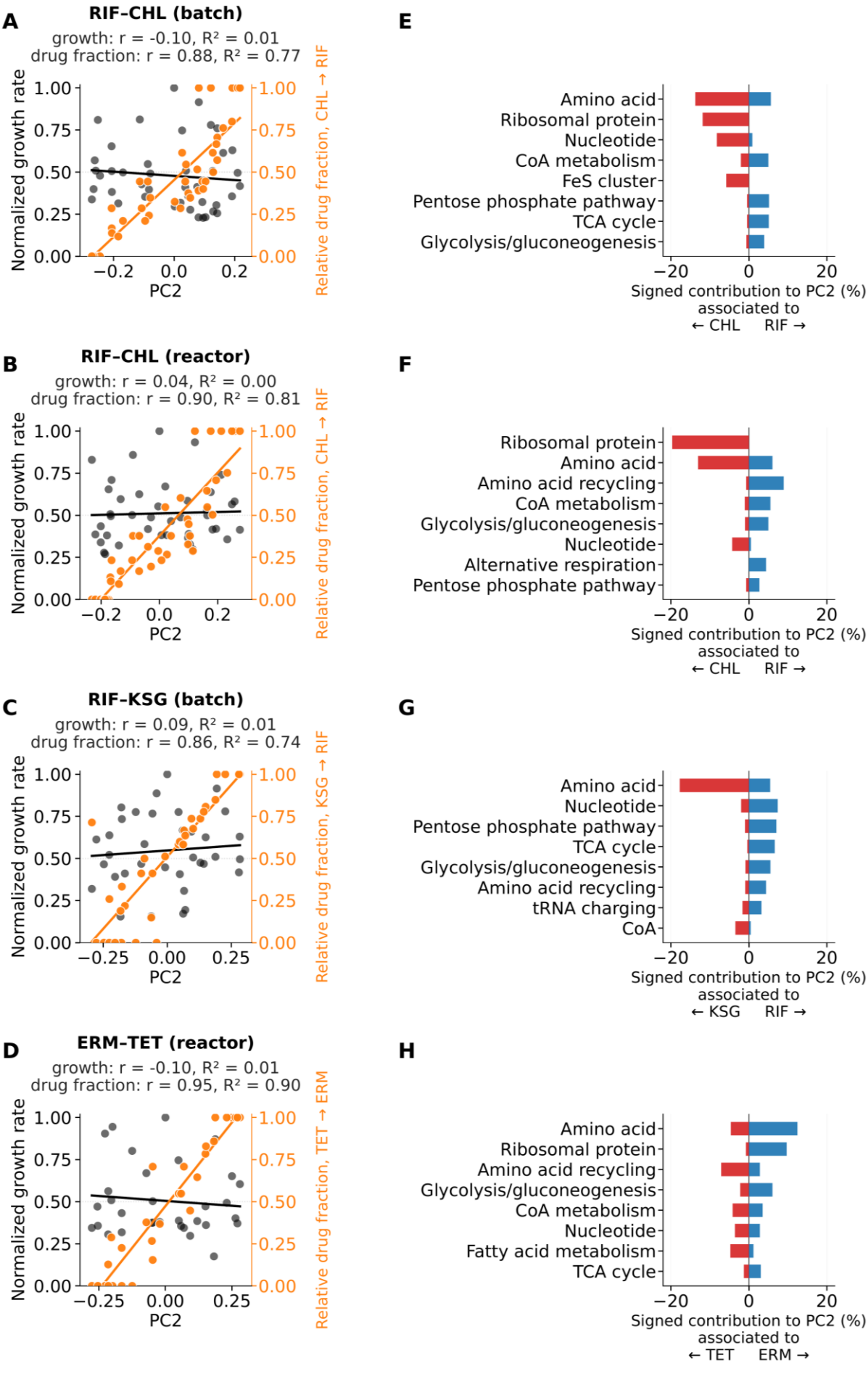


bioRxiv preprint doi: https://doi.org/10.64898/2026.08.21.746212; this version posted August 24, 2026. The copyright holder for this preprint (which was not certified by peer review) is the author/funder, who has granted bioRxiv a license to display the preprint in perpetuity. It is made available under a CC-BY-NC-ND 4.0 International license.

Fig. S6: The first principal component captures growth-rate-dependent proteome variation.

A–D) normalized growth rate (gray) and relative drug fraction (blue) plotted against the first PC (PC1) for rifampicin–chloramphenicol (A, batch culture; B, bioreactor), rifampicin–kasugamycin (C, batch culture), and erythromycin–tetracycline (D, bioreactor). Lines show linear fits; Pearson's *r* and R^2 are indicated. The relative fraction of drug A in a combination with drug B is defined as $x_A = \frac{c_A/\mathrm{IC}_{50,A}}{c_A/\mathrm{IC}_{50,A}+c_B/\mathrm{IC}_{50,B}}$ (Methods). **E–H)** Signed contributions to the first PC of the main level-2 functional groups for rifampicin–chloramphenicol (E, batch culture; F, bioreactor), rifampicin–kasugamycin (G, batch culture), and erythromycin–tetracycline (H, bioreactor). Positive values are associated with faster growth and negative values with slower growth.

bioRxiv preprint doi: https://doi.org/10.64898/2026.08.21.746212; this version posted August 24, 2026. The copyright holder for this preprint (which was not certified by peer review) is the author/funder, who has granted bioRxiv a license to display the preprint in perpetuity. It is made available under a CC-BY-NC-ND 4.0 International license.



bioRxiv preprint doi: https://doi.org/10.64898/2026.08.21.746212; this version posted August 24, 2026. The copyright holder for this preprint (which was not certified by peer review) is the author/funder, who has granted bioRxiv a license to display the preprint in perpetuity. It is made available under a CC-BY-NC-ND 4.0 International license.

Fig. S7: The second principal component captures drug-specific proteome variation.

A–D) Second PC plotted against normalized growth rate (gray) and relative drug fraction (orange) for the same four datasets as in Fig. S6A-D. Lines show linear fits; Pearson *r* and R^2 are indicated.

E–H) Signed contributions to the second PC of the main level-2 functional groups. The direction of the contribution indicates association with the drug indicated below each panel.

bioRxiv preprint doi: https://doi.org/10.64898/2026.08.21.746212; this version posted August 24, 2026. The copyright holder for this preprint (which was not certified by peer review) is the author/funder, who has granted bioRxiv a license to display the preprint in perpetuity. It is made available under a CC-BY-NC-ND 4.0 International license.

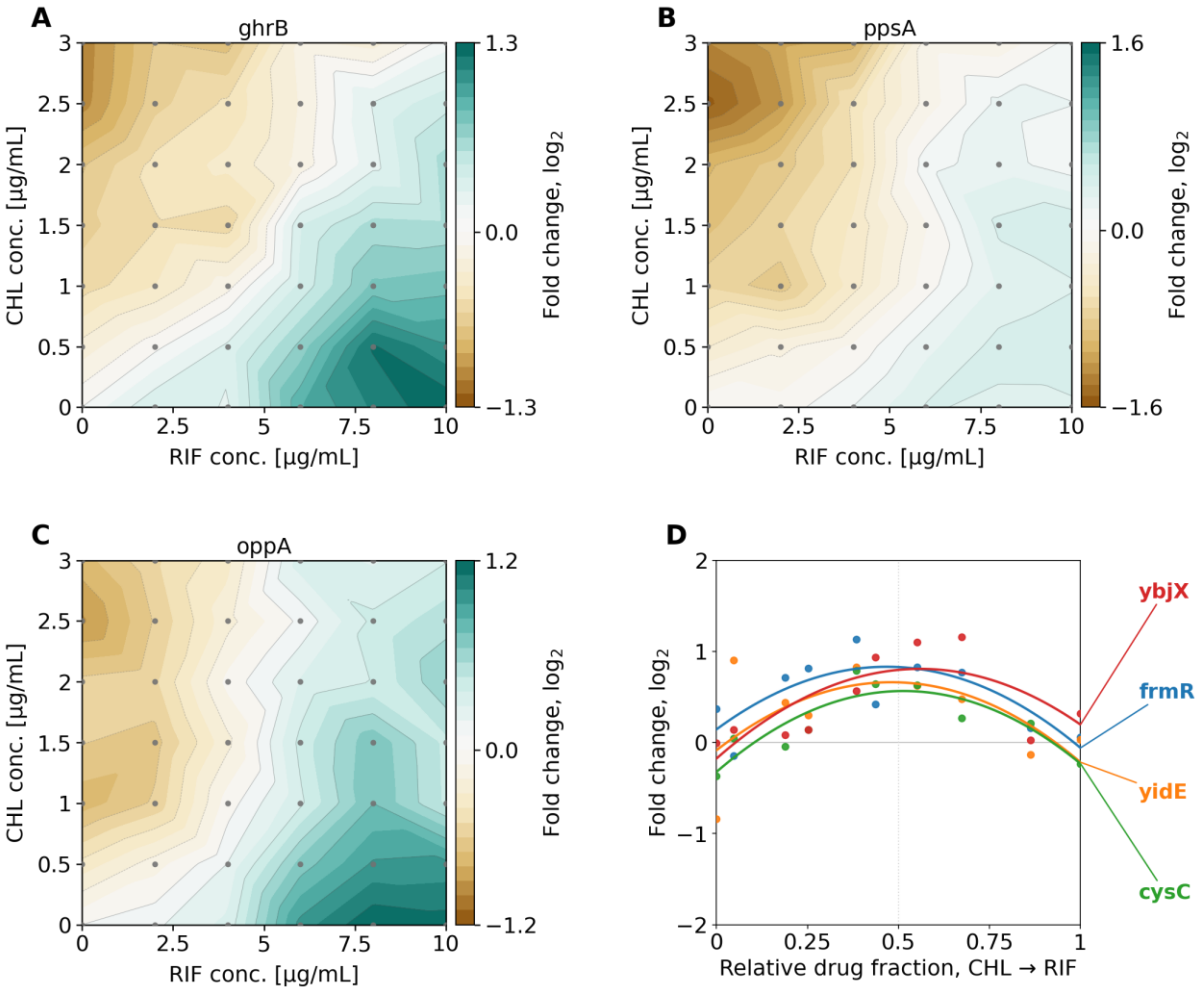


Fig. S8: Examples of protein-level responses to an antibiotic combination and candidates for emergent responses.

A-C) Fold-change in expression level in two-dimensional concentration gradient of chloramphenicol (CHL) and rifampicin (RIF) for the glyoxylate reductase GhrB (A), the phosphoenolpyruvate synthetase PpsA (B), and OppA (C), the periplasmic binding protein of an oligopeptide ABC transporter[49].

D) Expression level along isobole as in Fig. 4E for the four best candidate proteins (YbjX, FrmR, YidE, CysC) exhibiting signs of emergent responses (Methods).

Data in A–D were obtained from bioreactor-grown cultures (Methods).

bioRxiv preprint doi: https://doi.org/10.64898/2026.08.21.746212; this version posted August 24, 2026. The copyright holder for this preprint (which was not certified by peer review) is the author/funder, who has granted bioRxiv a license to display the preprint in perpetuity. It is made available under a CC-BY-NC-ND 4.0 International license.

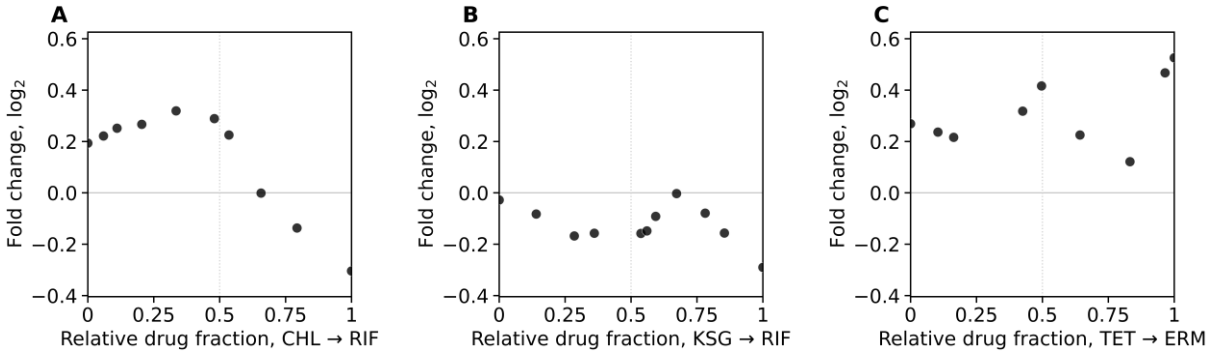


Fig. S9: Ribosome response to antibiotic combinations along isoboles.

A) Fold-change in ribosome concentration in response to the rifampicin-chloramphenicol (RIF-CHL) combination as in Fig 2A, but plotted along the isobole at 50% growth inhibition as in Fig. 4E.

B-C) As A, but for the rifampicin-kasugamycin (RIF-KSG, B) and erythromycin-tetracycline (ERM-TET) combinations (C).

Data in A and B were obtained from cultures grown in flasks, whereas data in C were obtained from bioreactor-grown cultures (Methods).

bioRxiv preprint doi: https://doi.org/10.64898/2026.08.21.746212; this version posted August 24, 2026. The copyright holder for this preprint (which was not certified by peer review) is the author/funder, who has granted bioRxiv a license to display the preprint in perpetuity. It is made available under a CC-BY-NC-ND 4.0 International license.

Supplementary data

Table S1: Assignments of proteins and slopes in one-dimensional antibiotic concentration gradients for different sectors in level 1–3 groups across two independent batches[40].

Table S2: Absolute scaled protein mass fractions (in percent) for all detected proteins across all experimental conditions.

3 Drug interactions between translation inhibitors are largely conserved across nutrient conditions

3.1 Introduction

The same antibiotic can produce different dose–response curves under varying nutrient conditions. The nutrient environment affects cellular resource allocation, growth rate [1, 7, 45], drug transport and response to translation inhibitors [62]. A biophysical model incorporating bacterial growth laws explains both steep and gradual responses to translation inhibitors [62]. Related theoretical and experimental work has also identified bistable antibiotic responses, in which different growth states can occur at the same antibiotic concentration [63, 96]. The model is described in section 1.6.1 [62]. At steady state, the model introduces two characteristic quantities. The response parameter $\alpha = \frac{\lambda_0^*}{\lambda_0}$ describes the shape of the dose–response curve by comparing the drug-specific reversibility scale λ_0^* with the drug-free growth rate λ_0. The reversibility scale is defined as $\lambda_0^* = 2\sqrt{P_{\text{out}}\kappa_{\text{t}}K_{\text{D}}}$, combining the antibiotic efflux rate P_{out}, the ribosome dissociation constant K_{D} and the translational capacity κ_{t}.
The characteristic concentration $\text{IC}_{50}^* = \frac{\Delta r \lambda_0^*}{2P_{\text{in}}}$ sets the antibiotic concentration scale of the response with Δr the dynamic range of the ribosome concentration and P_{in} the antibiotic influx rate [62, 88].

If λ_0^* and IC_{50}^* remain constant for a given antibiotic, nutrient-dependent changes in the drug-free growth rate λ_0 lead to predictable changes in the dose–response curve. For example, an increase in λ_0 results in a decrease in α.
The model has also been extended to pairs of translation inhibitors. The interaction depends on the two single-drug responses and whether the drugs compete for ribosome binding or bind independently [71, 88]. Strong changes in the single-drug dose–response curves across nutrient conditions could also alter the interaction between two antibiotics. Within the model, if the drug properties and ribosome-binding mechanisms remain unchanged, changes in the interaction should arise from changes in the single-drug responses. This raises the question of whether these changes are sufficient to alter drug interactions across nutrient conditions.
By measuring the growth of a luminescent strain across antibiotic concentration gradients, I obtained dose–response curves for nine antibiotics in six nutrient conditions, spanning an approximately threefold range in drug-free growth rates. These measurements allowed me to test whether dose–response shape and susceptibility followed the growth law prediction across nutrient conditions (section 3.2.1).
Next, I analyzed 28 drug pair–medium combinations involving six pairs of four translation inhibitors across five nutrient conditions. The measured growth surfaces were compared with Loewe additivity [69, 87] (section 3.2.2), while the fitted single-drug parameters and the drug-free growth rate were used as inputs to the interaction model to evaluate how well a simple biophysical model captures the drug interactions (section 3.2.3).
The single-drug responses covered the different regimes predicted by the growth law-based model, but their changes across nutrient conditions could not be explained by the drug-free growth rate alone. In contrast, most drug interactions were conserved across nutrient conditions, although the interaction between chloramphenicol and erythromycin gradually shifted from antagonistic to additive. The two-drug model provided an exploratory description of these interactions. The independent-binding model captured some of the variation in measured interaction types but predicted a narrower range of interaction strengths. The model can therefore help distinguish which aspects of the interactions can be explained by the single-drug responses and which require additional mechanisms.

3.2 Results

3.2.1 Single-drug responses vary across nutrient conditions

To obtain a broad range of drug-free growth rates, λ_0, I used six media with different nutrient compositions. The resulting growth rates ranged from approximately 0.37 to 1.30 h^{-1}. The media included lysogeny broth (LB), M9 glucose (GLU), M9 mannose (MAN), glucose or mannose supplemented with amino acids (GLUAA and MANAA). Among these conditions, the lowest growth rate was achieved in a medium containing a 1:10 ratio of glucose to α-methyl-D-glucopyranoside (α-MG-10) (fig. 3.1).

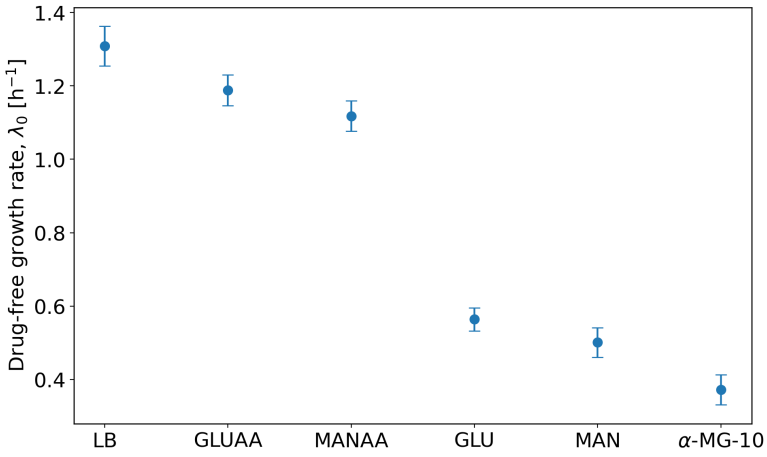


Figure 3.1: **Drug-free growth rates across nutrient conditions.** Mean drug-free growth rate, λ_0, in six media for eight replicates.

Responses were measured for nine translation inhibitors: kasugamycin (KSG), streptomycin (STR), doxycycline (DOX), tetracycline (TET), erythromycin (ERM), lincomycin (LCY), chloramphenicol (CHL), capreomycin (CRY) and fusidic acid (FUS). These drugs covered a broad range of molecular targets within translation and produced different dose–response shapes. The modes of action are summarized in table 1.1. KSG, CHL and FUS are examples of steep, intermediate and gradual responses, respectively (fig. 3.2). The parameters IC_{50} and α were obtained by fitting the steady-state solution of the growth-dependent model (eq. (3.1)) to each dose–response curve [62, 71, 88]. Here, $y = \lambda/\lambda_0$ is the growth rate relative to the drug-free growth rate and $c = \frac{a_{ex}}{IC_{50}}$ is the extracellular antibiotic concentration normalized by the IC_{50}. The steady-state solution is

$$c(y;\alpha) = \frac{1}{1+\alpha^2}\left(\frac{\alpha^2}{y} - \alpha^2 + 4y - 4y^2\right). \tag{3.1}$$

Small values of α produce steep responses, whereas larger values produce more gradual inhibition [62]. The complete set of fits is shown in fig. A.1.

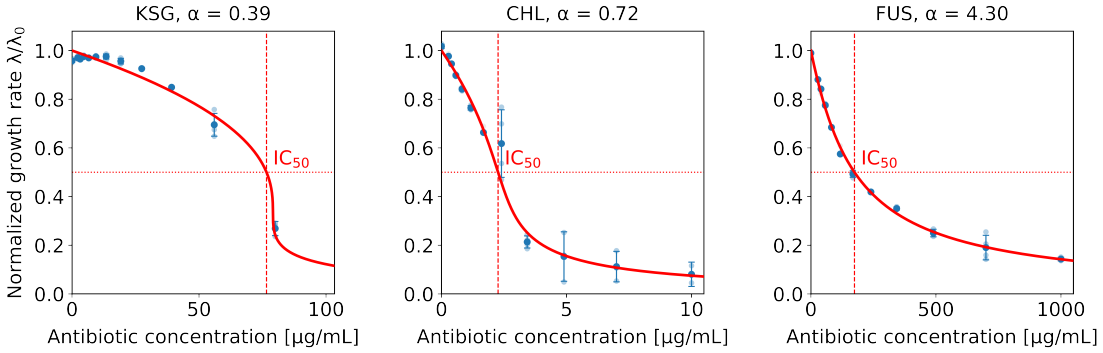


Figure 3.2: **Single-drug growth law fits.** KSG, CHL and FUS show steep, intermediate and gradual responses. Red lines show fits of eq. (3.1) and dashed lines indicate the fitted IC_{50}.

At half-maximal inhibition, $y = 0.5$, the model gives the universal susceptibility relation

$$\frac{IC_{50}}{IC_{50}^*} = \frac{1}{2}\left(\alpha + \frac{1}{\alpha}\right), \tag{3.2}$$

Taking the derivative of eq. (3.2) gives $f'(\alpha) = \frac{1}{2}\left(1 - \frac{1}{\alpha^2}\right)$. For $\alpha < 1$, the normalized IC_{50} decreases with increasing α, while for $\alpha > 1$ it increases. The relation is therefore U-shaped with a minimum at $\alpha = 1$. Since α depends on the drug-free growth rate, the model predicts that different growth conditions can either increase or decrease the IC_{50}, depending on the response regime of the antibiotic. Across the included drug–medium conditions, the normalized IC_{50} values showed a moderate correlation with the universal prediction (fig. 3.3A; Spearman $\rho = 0.37$, $p = 0.028$). However, the model explained only a small fraction of the quantitative variation ($R^2 = 0.22$ in $\log_{10}$ space). When each medium was excluded in turn, 74% of the predicted values were within twofold of the measured IC_{50}.
Prediction errors also differed among drugs. ERM and TET showed the closest agreement with mean fold errors of approximately 1.21- and 1.25-fold, respectively. CRY showed the largest error, approximately 2.05-fold, followed by STR and FUS with errors of approximately 1.77-fold.
I next tested whether the model predicted the direction of susceptibility changes within individual drugs. I considered three nutrient transitions: α-MG-10 to GLU, GLU to GLUAA and MAN to MANAA (fig. 3.3B).
Among the 13 matched nutrient transitions with accepted fits, the measured IC_{50} changed in the predicted direction in 10 cases. The three exceptions were CHL

from GLU to GLUAA, CRY from MAN to MANAA and DOX from α-MG-10 to GLU. This level of agreement was greater than expected if both directions were equally likely (one-sided binomial $p = 0.046$).
Thus, the growth law-based model predicted whether susceptibility increased or decreased in most cases, but not the size of these changes. This suggests that drug-specific parameters assumed to be constant in the model may change between nutrient conditions.

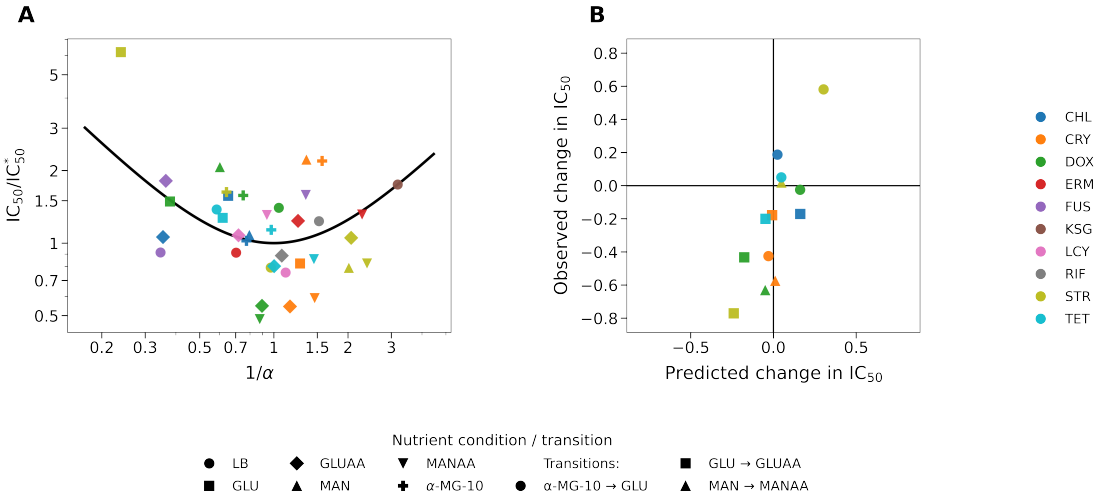


Figure 3.3: **Nutrient-dependent single-drug susceptibility in the growth law framework.** (A) IC_{50}/IC_{50}^{*} as a function of $1/\alpha$ for drug–medium conditions with accepted dose–response fits. The black line shows the universal growth law relation. (B) Predicted versus measured changes in IC_{50} for matched nutrient transitions.

3.2.2 Most interactions remain stable across nutrient conditions

After observing nutrient-dependent changes in the single-drug responses, I examined whether the interactions between two antibiotics also changed with the nutrient condition. I measured two-dimensional concentration gradients for all six pairs of CHL, ERM, STR and TET across five media. Growth rates were normalized to the drug-free growth rate in the same medium, giving a two-dimensional response surface for each drug pair and condition. Two-dimensional concentration gradients are commonly used to quantify antibiotic interactions across drug combinations [85].

For each surface, the deviation from Loewe additivity was summarized by the Loewe interaction score (LI; see section 1.4.2 and methods section of chapter 2) [69, 87, 88]. Interactions were classified as antagonistic for LI > 0.08, synergistic for LI < -0.12 and additive between these thresholds. Representative examples of the three interaction classes are shown in fig. 3.4.

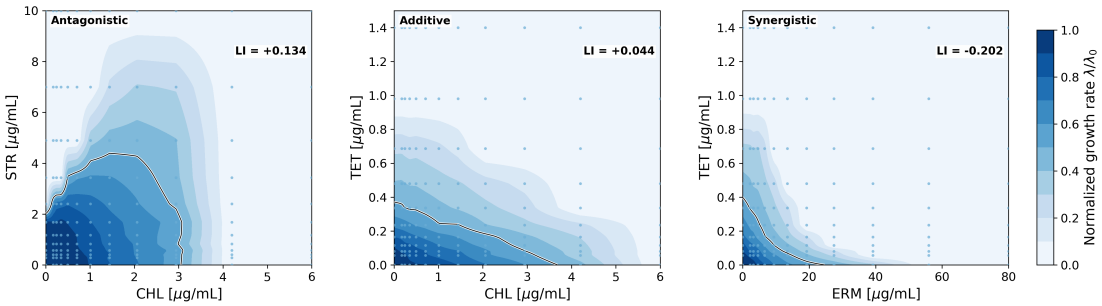


Figure 3.4: **Representative measured two-drug interactions.** Examples of antagonistic, additive and synergistic measured growth surfaces. Dashed lines indicate the IC_{50} isoboles.

Four of the six drug pairs showed little change in interaction class across media (fig. 3.5; complete two-dimensional response surfaces are shown in fig. A.2). CHL–STR was antagonistic and CHL–TET additive in all five conditions. STR–ERM was antagonistic in most conditions. In MAN, the LI was +0.072, slightly below the antagonistic cutoff. ERM–TET was synergistic in four media and additive only in GLU. The classification of these pairs remained largely conserved, despite changes in single-drug responses between media.

Larger changes were observed for CHL–ERM and STR–TET (fig. 3.6). CHL–ERM became less antagonistic from LB to the slower-growing media. The interaction was antagonistic in LB and GLUAA but additive in MANAA, GLU and MAN with the LI gradually decreasing from +0.121 in LB to +0.045 in MAN as the drug-free growth rate decreased. However, the fitted single-drug α values did not show a corresponding trend. The change in CHL–ERM could not be explained

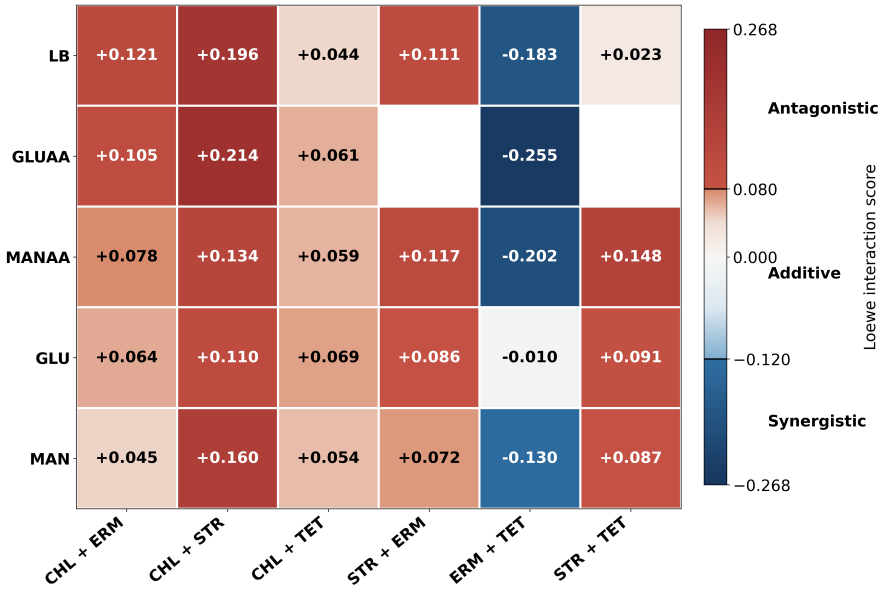


Figure 3.5: **Drug interaction scores across nutrient conditions.** Loewe interaction scores for six antibiotic pairs across five nutrient conditions. Scores were classified as antagonistic (LI > 0.08), synergistic (LI < -0.12) or additive otherwise. Empty fields indicate missing measurements.

directly by changes in the single-drug dose–response shapes.
STR–TET behaved differently. The interaction was additive only in LB and antagonistic in all other conditions measured. No surface was available in GLUAA due to technical issues. Across the measured drug pairs, the interactions did not change systematically with the drug-free growth rate, except for CHL–ERM.
Overall, the interaction network was largely conserved with a few exceptions. Some of these differences could partly result from using the same absolute concentration ranges across nutrient conditions. Because drug susceptibility changed between media, future measurements should instead use condition-specific concentration ranges.

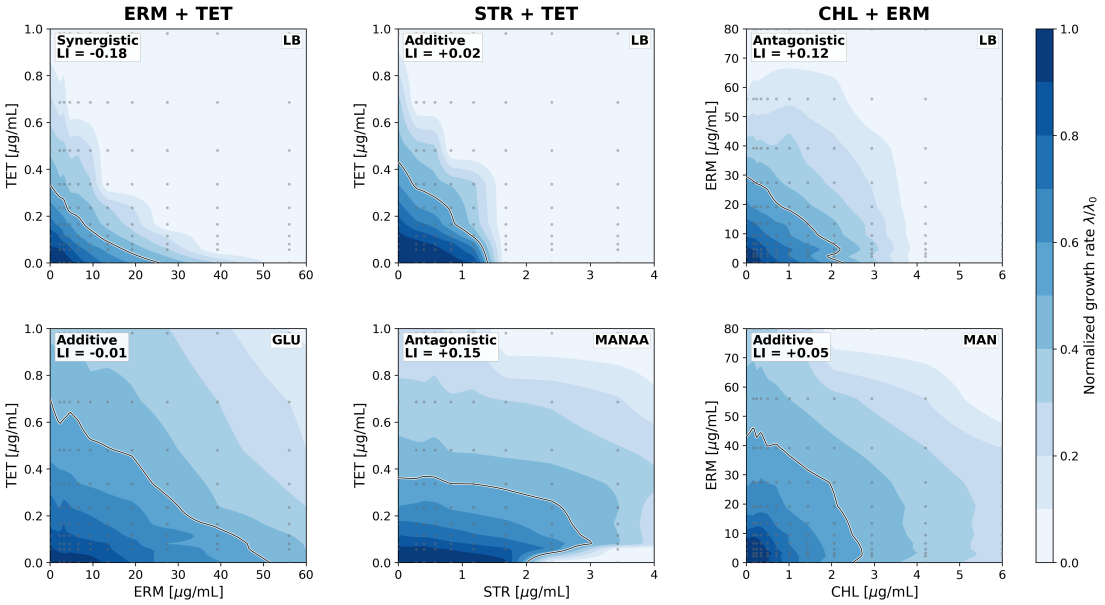


Figure 3.6: **Nutrient-dependent changes in drug interactions.** Measured growth surfaces for drug pairs for which the interaction classification changed across nutrient conditions. Dashed black lines denote the IC_{50} isoboles.

3.2.3 Biophysical model captures part of the measured drug interactions

If the single-drug responses together with the ribosome-binding scheme are sufficient to determine the drug interaction, the measured interaction should be reproduced by the biophysical model described in section 1.6.2. The model considers two binding schemes for pairs of ribosome-targeting antibiotics [71, 88]. When two drugs compete for binding, so that one prevents the other from binding, the model predicts an additive interaction. In the independent-binding scheme, both drugs can bind simultaneously and the interaction depends on the single-drug dose–response parameters. For each drug pair and nutrient condition, the fitted IC_{50} values were used to normalize the concentrations of the two antibiotics. The fitted response parameters α_A and α_B, together with the corresponding drug-free growth rate λ_0, were then used to calculate the two-dimensional growth surfaces, focusing on the independent-binding scheme.

The independent-binding model showed both antagonistic and synergistic interactions. Pairs in which both drugs had steep single-drug responses with $\alpha_i < 1$, where i denotes the individual drug, generally produced antagonism, which became stronger for smaller α_i values. In contrast, pairs in which both drugs had more

gradual responses with $\alpha_i > 1$ generally produced synergy, which became stronger as the α_i values increased [71, 88]. Antagonistic, additive and synergistic model surfaces are shown in fig. 3.7.

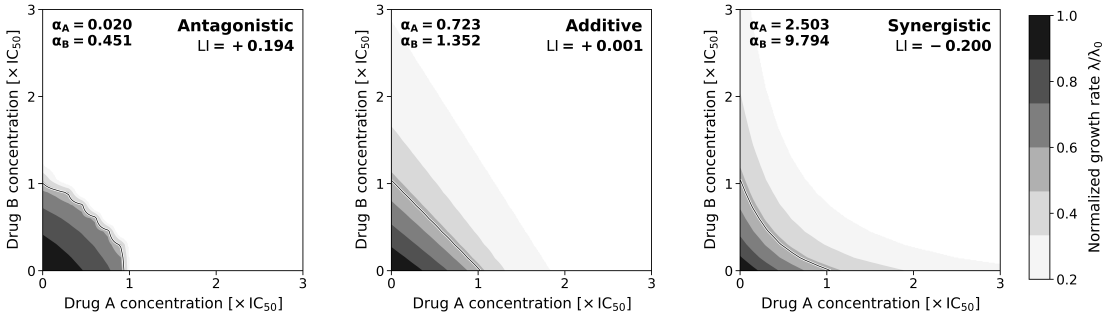


Figure 3.7: **Representative model interactions.** Examples of antagonistic, additive and synergistic growth surfaces generated from different combinations of the response parameter α. For the additive interaction, the competitive-binding scheme was chosen. The LI score and interaction type are shown. Colors indicate predicted growth normalized to the drug-free growth rate.

The complete interaction predictions for the 28 measured growth surfaces are shown for the competitive-binding and independent-binding schemes in fig. A.3 and fig. A.4, respectively. For the independent-binding scheme, the predicted and measured LI values were moderately correlated (Pearson $r = 0.57$, $n = 28$; fig. 3.8). More antagonistic measured interactions tended to have higher predicted LI values, whereas stronger synergistic measured interactions tended to have lower predicted values.

The predicted LI values covered a narrower range than the measured values and were shifted toward zero. Strong antagonistic and synergistic interactions were therefore generally predicted to be weaker than measured. The model captured the general trend from stronger antagonistic to stronger synergistic interactions, but not their full strength. This suggests that the single-drug response parameters contain some information about the interaction, but are not sufficient to determine the interaction strength. Determining α is particularly difficult for steep dose–response curves because the transition from little inhibition to strong growth reduction occurs over a narrow concentration range and only a few measured points constrain the fit.

Together, the independent-binding model captured part of the measured interaction pattern, but shifted the predictions toward additivity. The model tested here assumed that the two drugs affect each other symmetrically. Allowing for asymmetric effects could help explain some of the remaining differences between

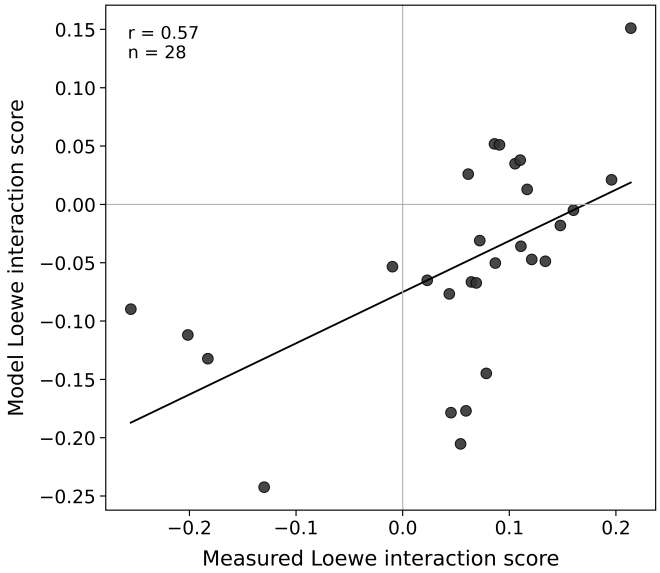


Figure 3.8: **Comparison of measured and independent-binding model interaction scores.** Measured Loewe interaction scores are compared with scores calculated from the corresponding independent-binding model surfaces for $n = 28$ drug pair–medium combinations, with a Pearson correlation coefficient of $r = 0.57$. The black line shows the linear trend.

predicted and measured interaction strengths [88].

3.3 Discussion

Nutrient conditions affected the single-drug responses more strongly than the interactions between drug pairs. The growth law-based model captured the direction of most changes in susceptibility but not their magnitude (fig. 3.3). In contrast, most interactions remained stable across nutrient conditions (fig. 3.5). This is consistent with previous work showing that antibiotic interactions are often conserved within a bacterial species, whereas larger differences can occur between species and in some cases between strains [80, 81].

One reason for this stability may be that all tested drugs target translation. Interactions between translation inhibitors depend on which steps of the translation cycle are affected [71]. Nutrient conditions change growth rate, ribosome abundance and drug susceptibility, but the molecular targets of the antibiotics remain the same.

This explanation did not account for all pairs. CHL–ERM became gradually less antagonistic as the drug-free growth rate decreased, although the fitted single-drug α values did not show a corresponding trend. STR–TET also changed interaction class without a systematic relation to growth rate.

The independent-binding model captured only part of the measured interaction pattern. Changes in drug transport, intracellular drug concentrations or the state of the translation machinery could contribute to the remaining differences [62, 80].

A useful next step would be to compare proteome changes during single-drug and combination treatments in nutrient conditions where the interaction changes. For example, the response to CHL–ERM could be compared between conditions with weaker and stronger antagonism to identify changes in ribosome allocation, transport systems or stress responses. For STR–TET, the role of streptomycin transport could be tested using an *acrD* deletion strain. AcrD is an aminoglycoside efflux transporter and deletion of *acrD* increases intracellular dihydrostreptomycin accumulation [97]. Comparing the interaction between the wild type and the deletion strain across nutrient conditions could test whether AcrD-mediated efflux contributes to the change in interaction type.

Overall, most interactions between translation inhibitors were conserved, while the exceptions point to physiological effects that are not captured by growth rate alone.

3.4 Materials and Methods

3.4.1 Experimental methods

Bacterial strain and frozen stocks

All experiments were performed with *Escherichia coli* K-12 BW25113 carrying the pCS-λ plasmid, which contains the constitutively expressed *luxCDABE* reporter system. Frozen stocks were prepared from overnight cultures grown in lysogeny broth (LB). Glycerol was added to a final concentration of 15% and the stocks were stored at $-80\,^{\circ}\mathrm{C}$.

Growth media and antibiotic preparation

Along with LB, five M9-based nutrient conditions were used. Minimal media consisted of $1\times$ M9 salts, 2 mM $MgSO_4$, 0.1 mM $CaCl_2$ and either 4 g/L glucose or 4 g/L mannose. For the amino acid-supplemented conditions, 2 g/L amino acids were added to the corresponding glucose or mannose medium. An additional slow-growth condition included glucose and α-methyl-D-glucopyranoside at a 1:10 ratio.
Chloramphenicol, erythromycin and tetracycline were dissolved in ethanol. The remaining antibiotics were dissolved in Milli-Q water. All antibiotic solutions were passed through 0.22 μm filters and stored at $-20\,^{\circ}\mathrm{C}$ until use.

Growth measurements

Cells from frozen stocks were diluted $1 : 10^6$ directly into prepared antibiotic concentration gradients (one- or two-dimensional). Cultures were grown at 30°C for at least 70 h. Luminescence was measured approximately every 15 min using a plate reader with an automated stacker. Before each measurement, the plates were shaken at 250 rpm for 15 s.

3.4.2 Analysis

Growth-rate extraction

Growth rates were calculated for each well from the exponential increase in luminescence. The logarithm of the luminescence signal was fitted using linear regression over consecutive windows of 3 to 10 measurements with `scipy.stats.linregress`. Only increasing signals above approximately 200 luminescence units and before the maximum signal were considered. The longest accepted window with a slope standard error below 0.1 h^{-1} was retained and its slope was used as the growth

rate. If no suitable window was found, the growth rate was set to zero. Growth rates were normalized to the untreated condition in the same nutrient medium.

Single-drug dose–response fitting

Single-drug dose–response curves were fitted in inverse form using the `least_squares` function from `scipy.optimize` and the reduced growth-law relation in eq. (3.1). The parameters IC_{50} and α were estimated simultaneously using bounded least-squares fitting. Fits with $R^2 < 0.80$ or with insufficient inhibition to constrain α were excluded from the main statistical analyses, as indicated.

Universal susceptibility relation

For each accepted antibiotic–medium combination, the fitted IC_{50} and α values were used to calculate IC_{50}^* according to eq. (3.2). For each antibiotic, a single drug-specific IC_{50}^* value was calculated as the mean across accepted nutrient conditions.
Condition-specific IC_{50} values were then calculated from the drug-specific IC_{50}^* and the fitted α values. Agreement between measured and calculated IC_{50} values was evaluated using `scipy.stats.spearmanr` and R^2 calculated in $\log_{10}$ space. For validation, each medium was excluded in turn when calculating IC_{50}^* for each drug. This value was then combined with the fitted α of the excluded condition to calculate its IC_{50}.
For matched changes between nutrient conditions, agreement in the direction of measured and calculated changes in IC_{50} was tested against a null probability of 0.5 using the one-sided exact binomial test from `scipy.stats.binomtest`.

Two-drug interaction analysis

For the two-drug interaction analysis, the single-drug dose–response curves were fitted with Hill functions. These fits were used to create the Loewe-additive reference surface according to eq. (1.6). At each concentration pair, the additive growth level was obtained by solving the Loewe additivity equation numerically using `scipy.optimize.root_scalar`.
The Loewe interaction score LI was calculated as described in the Methods of chapter 2. Regions with normalized growth $y \leq 0.05$ were excluded.
Interactions were classified as antagonistic when $LI > 0.08$, synergistic when $LI < -0.12$ and additive otherwise ($-0.12 \leq LI \leq 0.08$), following the classification used in [71].

Two-drug biophysical model

A detailed description can be found in [88]. Each modeled interaction used the medium-specific drug-free growth rate λ_0 and the fitted response parameters α of both antibiotics. The fitted IC_{50} values were used to normalize the corresponding antibiotic concentrations. The model equations were solved using `scipy.integrate.solve_ivp`.
Independent single-drug fits were used where available. If a single-drug fit for α failed the fitting criteria, α was instead obtained from the corresponding zero-partner edge of the two-dimensional measurement. These values were marked as low-confidence inputs.
Both binding schemes were evaluated for the measured drug pair–medium combinations. The main quantitative comparison used the independent-binding scheme, while competitive-binding scheme provided an additive surface.

4 Comparison of GFP reporter dynamics and protein abundance during the diauxic shift

4.1 Introduction

Quantitative studies comparing mRNA and protein levels have shown that mRNA abundance explains part of the variation in protein abundance [98, 99], while post-transcriptional regulation and protein-specific processes also contribute substantially [100–102]. More recently, close coordination between mRNA and protein fractions under steady-state growth conditions in *E. coli* was reported [19]. Promoter on-rates were identified as a main determinant of protein concentrations. These rates were inferred from transcription initiation rates calculated from mRNA abundance, mRNA degradation rates and gene copy number and were then normalized by the estimated concentration of available RNA polymerase [19].
Time-resolved fluorescent reporters have also been used to quantify promoter activity and regulatory dynamics in *E. coli* [103, 104]. Genome-scale robotic measurements with the same promoter-reporter library have further enabled high-throughput tracking of promoter activity across growth phases and environmental conditions [105, 106].
Here, we asked whether promoter-dependent reporter signals and protein abundance remain similarly coordinated during a dynamic change in growth conditions. The glucose–lactose diauxic shift was used as a model system because it represents a classical example of metabolic adaptation through gene regulation. When glucose is depleted, growth temporarily slows while lactose-utilization genes are induced, allowing growth to resume on lactose [12, 107]. This process involves extensive changes in gene expression, including induction of lactose-use genes and changes in growth- and stress-related pathways [108–110].
To compare green fluorescent protein (GFP) reporter dynamics with protein abundance changes, we combined time-resolved GFP measurements with quantitative proteomics obtained under the corresponding diauxic-shift conditions. The GFP reporter measurements were performed with experimental support from Dr. Adriana Espinosa-Cantu. The reporter strains were taken from the Uri Alon promoter

library, in which promoter regions are fused to a fast-folding GFP reporter carried on low-copy plasmids [108]. The library contains more than 1800 promoter constructs and allows promoter-dependent fluorescence accumulation to be followed over time. All 21 library plates were measured using a high-throughput robotic system and processed in two experimental batches. For the corresponding proteomics time course, *E. coli* K-12 MG1655 without the GFP reporter plasmid was grown under the same diauxic-shift conditions in 96-well plates. At defined time points, whole plates were pooled to obtain sufficient material for proteomics analysis, as illustrated in fig. 4.1.

Throughout this chapter, background-subtracted GFP fluorescence normalized by OD is referred to as GFP profiles (section 4.4.2). These profiles reflect accumulated promoter-dependent fluorescence per biomass, whereas protein mass fraction describes the relative contribution of a protein to the cellular proteome. We compared both relative temporal dynamics and GFP-derived pseudo mass fractions with proteomics-derived protein mass fractions.

Both datasets captured the expected diauxic-shift response. Genome-wide, GFP reporter and protein dynamics showed a positive but moderate correspondence, with a median Pearson correlation of $r = 0.25$. Agreement was strongest for prominently induced metabolic genes, while other genes differed in timing or profile shape. Aggregation at the transcription-unit level did not improve the correspondence. GFP-derived pseudo mass fractions also showed only weak quantitative agreement with protein mass fractions. Thus, the reporters captured relative temporal regulation but were not reliable quantitative proxies for protein abundance.

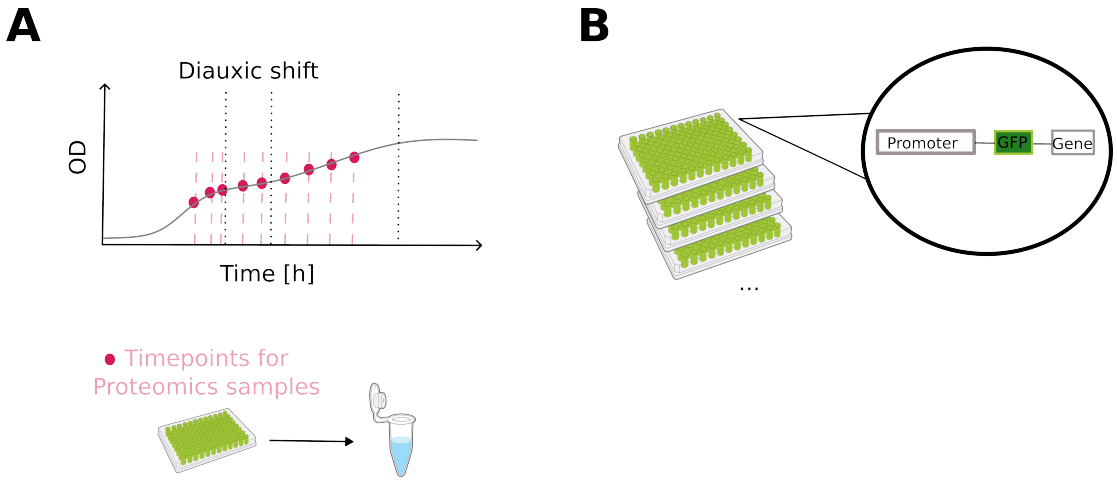


Figure 4.1: **Experimental setup for comparing GFP reporter dynamics and protein abundance during the diauxic shift.** (A) Growth trajectory and proteomics sampling time points. (B) GFP reporter strains were measured over time to follow promoter-dependent fluorescence accumulation.

4.2 Results

4.2.1 Dataset characterization and responses during the diauxic shift

As a first step, the GFP reporter and proteomics datasets were analyzed separately to characterize the temporal structure of the experiment and to determine whether representative marker genes and proteins showed the expected responses during the diauxic shift (fig. 4.2). All OD and GFP profiles shown here are based on background-subtracted measurements, as described in Section 4.4.2.
The optical density increased throughout the experiment and approached a plateau at approximately 16.5 h, indicating the onset of stationary phase (fig. 4.2, top). The diauxic transition was estimated to occur between approximately 7.5 and 8.5 h, corresponding to glucose depletion and the transition to lactose-dependent growth. This is consistent with the expected glucose–lactose diauxic-shift response [109, 110], in which lactose- and galactose-utilization genes are induced after depletion of the preferred carbon source [108, 111]. Although the transition was only weakly visible in the OD trajectory itself, it was clearly reflected in the GFP reporter and proteomics measurements.
The processed GFP dataset contained 1806 unique reporter profiles after exclusion of the promoterless control strains. Of these, 513 reporters exceeded the clear-signal

threshold (GFP/OD > 2570.2, section 4.4.2) at least three time points during the experiment, corresponding to 28.4% of the reporter library. The reproducibility of the GFP/OD measurements was assessed using the repeated *lacZ* control, which was included in well H1 on 20 of the 21 reporter-library plates. For the variability analysis, processed *lacZ* measurements were included when at least two control measurements contributed to the mean GFP/OD value and the mean exceeded the clear-signal threshold. The median coefficient of variation among replicates measured at the same time point was 13.2%.

The GFP reporter profiles showed the expected responses during the diauxic shift (fig. 4.2, middle). The strongest responses were observed for the lactose-utilization gene *lacZ* and the galactose pathway gene *galE*, both of which increased shortly after the transition. This agrees with previous measurements from the reporter library during the glucose–lactose diauxic shift [108]. Other markers expected to have strong responses based on previous work showed weaker or broader responses [108]. The *lacY* reporter was only weakly detectable and did not show clear post-shift induction. The galactose-metabolism regulator *galS* showed a weaker but visible increase after the diauxic transition. This response was less pronounced than the induction observed for *galE*. The regulatory role of *galS* within the galactose-utilization network has been described previously [112, 113].

The stress-associated marker *dps* did not show a sharp response directly at the diauxic transition, but instead showed sustained GFP reporter signal during later growth. This delayed increase is consistent with its established role in stationary-phase and stress responses [114]. Because the *galS* and *dps* signals were less visible in the combined marker plot, their profiles are also shown separately in fig. 4.3.

At the proteome level, coverage remained stable throughout the analyzed time course, with approximately 1775 of the 2793 UniProt protein entries in the processed proteomics dataset showing positive mass-fraction values at each time point (chapter 2). This corresponds to approximately 64% of the protein entries included in the dataset. Uncertainty estimates for the protein mass fractions were obtained from the protein-abundance determination workflow. The marker proteins confirmed that the proteomics dataset captured the expected physiological response, but also showed that the GFP reporter and protein profiles were not always identical (fig. 4.2, bottom). LacZ and GalE increased strongly after the diauxic shift and remained elevated at later time points, consistent with the strong induction observed in the GFP reporter data. By contrast, the protein mass fractions of RplN and RpsP decreased during the diauxic transition, whereas the corresponding GFP reporter profiles showed different temporal responses, with increases around or shortly after the transition. Thus, reporter and protein dynamics were poorly aligned for these ribosomal proteins (fig. 4.2). Dps showed a transient increase around the diauxic shift, followed by a decrease and a second increase during the early lactose-dependent growth phase, whereas the corresponding GFP reporter

activity remained elevated during later growth.
Both datasets captured the expected diauxic-shift response, but individual GFP reporter and protein profiles did not always follow the same temporal pattern.

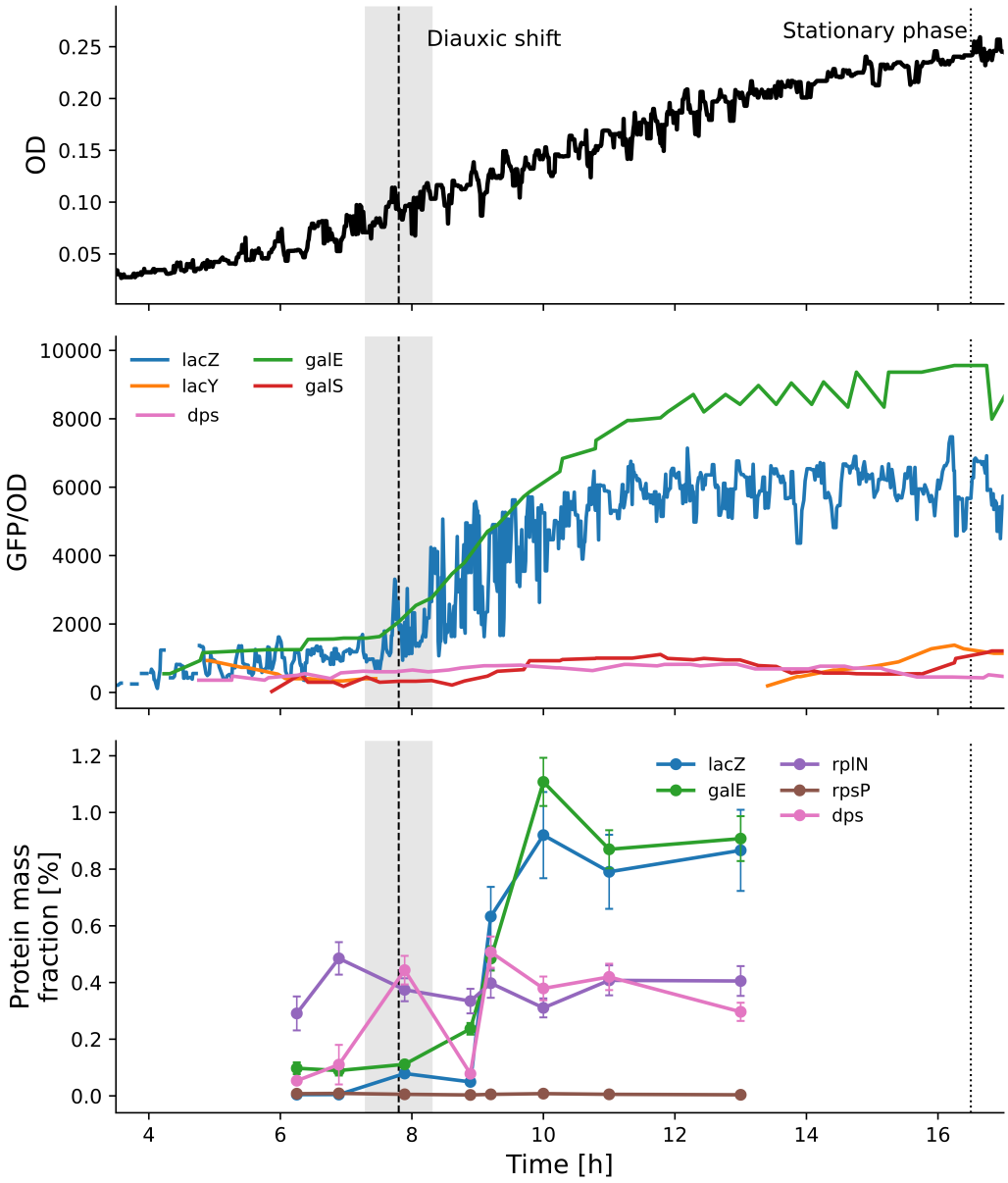


Figure 4.2: **Characterization of GFP reporter and proteomics measurements during the diauxic shift.** Top: mean background-subtracted optical density trajectory. Middle: mean GFP profiles of representative marker genes. Bottom: corresponding protein mass fractions measured by proteomics.

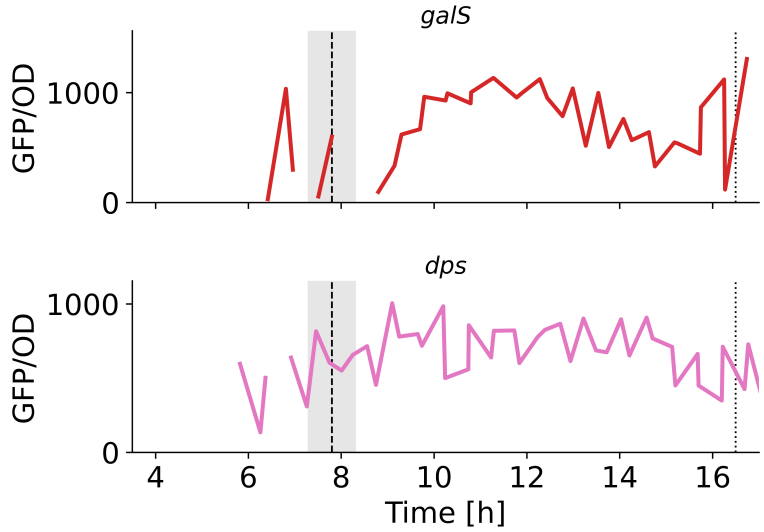


Figure 4.3: **Individual GFP profiles of *galS* and *dps*.** Top: *galS* showed a low and variable GFP signal before the diauxic shift, followed by a more sustained increase after the transition. Bottom: *dps* showed a variable GFP profile without a clear diauxic-shift-specific induction.

4.2.2 Temporal agreement between GFP reporter and protein abundance dynamics

After confirming that both datasets captured the diauxic-shift response, we next asked how closely the temporal dynamics of the GFP reporters corresponded to changes in protein abundance. This analysis focused on relative dynamics rather than direct abundance because GFP profiles and protein mass fraction are measured on different scales. For each matched reporter–protein pair, the GFP reporter profile was interpolated to the proteomics sampling times. The GFP and protein profiles were then independently normalized to their respective maximum values and their temporal similarity was quantified using the Pearson correlation coefficient. The resulting correlations therefore describe similarity in profile shape, but not quantitative agreement between the measured abundances.
Across 759 matched reporter–protein pairs, the distribution of Pearson correlation coefficients was shifted toward positive values (fig. 4.4). The median correlation was $r = 0.25$, indicating a positive but moderate genome-wide correspondence between GFP reporter and protein abundance dynamics. Overall, 67.2% of the pairs had positive correlations, while 28.5% showed stronger positive agreement with $r > 0.5$. Thus, changes in GFP profiles were frequently reflected at the protein level, but the strength of this relationship varied substantially between

genes. For comparison, Spearman rank correlations were calculated for the same 759 reporter–protein pairs. The median Spearman correlation was $\rho = 0.21$, with 66.3% of pairs showing positive correlations and 27.0% showing correlations above 0.5. Consequently, the qualitative conclusion was not dependent on the choice of correlation measure.

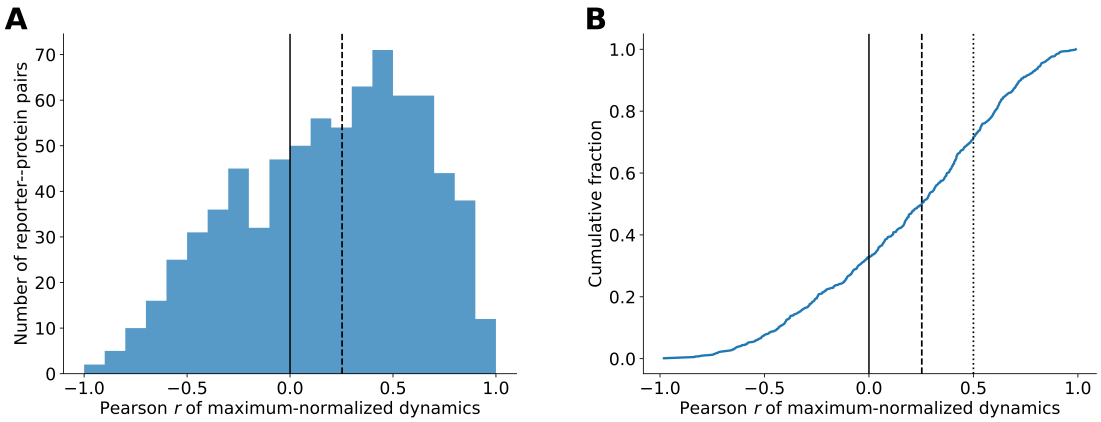


Figure 4.4: **Genome-wide comparison of maximum-normalized GFP reporter and protein abundance dynamics.** (A) Distribution of Pearson correlation coefficients for 759 matched reporter–protein pairs. (B) Corresponding cumulative distribution. The solid line marks $r = 0$, the dashed line the median correlation $r = 0.25$ and the dotted line the threshold $r = 0.5$.

This gene-specific variation was also apparent in the representative profiles shown in fig. 4.5. The lactose-utilization gene *lacZ* and the galactose-pathway gene *galE* showed particularly strong agreement, with correlations of $r = 0.99$ and $r = 0.92$, respectively. For both genes, GFP profiles were low before the diauxic transition. The corresponding protein mass fractions followed a similar pattern, showing that the strong promoter-dependent induction of these metabolic genes was also reflected at the protein level. The *selA* reporter–protein pair also showed a high positive correlation of $r = 0.85$. Both profiles increased across the diauxic transition and remained relatively high at later time points, although some differences between individual measurements remained.
The stress-associated gene *dps* showed a positive correlation of $r = 0.69$, but the detailed timing of the two profiles differed. The protein mass fraction displayed transient changes around the diauxic transition, whereas the GFP reporter profile increased more gradually and remained elevated for longer during later growth. A positive correlation therefore did not necessarily indicate identical response timing. By contrast, the ribosomal protein genes *rplN* and *rpsP* showed weak or negative

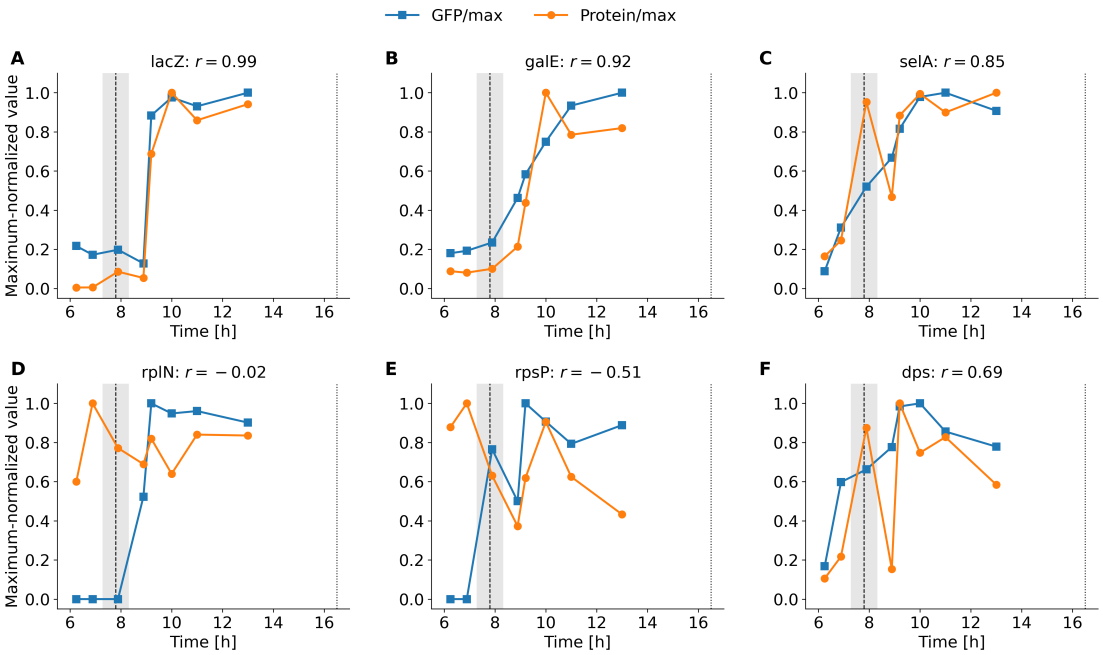


Figure 4.5: **Representative maximum-normalized GFP reporter and protein abundance profiles.** (A–C) Strong positive agreement for *lacZ*, *galE* and *selA*. (D–E) Weak agreement for *rplN* and *rpsP*. (F) Positive but temporally distinct profiles for *dps*. Pearson correlation coefficients quantify temporal profile similarity. The gray region marks the estimated diauxic-shift window.

agreement, with correlations of $r = -0.02$ and $r = -0.51$, respectively. Their protein mass fractions were already relatively high at the early sampling points or changed only moderately, whereas the corresponding GFP reporter signals remained elevated. These examples further demonstrate that promoter-reporter dynamics were not always directly reflected in protein abundance.

Because promoter reporters may reflect the activity of whole transcription units rather than individual protein-coding genes, we also tested whether aggregation at the transcription-unit level improved GFP–protein correspondence. Genes were mapped to EcoCyc transcription-unit annotations [113]. For each transcription unit, the GFP profiles and protein mass fractions of the assigned genes were summed at each time point and the resulting profiles were independently normalized to their respective maxima. The median Pearson correlation remained essentially unchanged, with $r = 0.25$ at the gene level and $r = 0.21$ at the transcription-unit level. Transcription-unit aggregation therefore did not explain the moderate genome-wide correspondence between GFP reporter and protein abundance dynamics.

GFP reporter dynamics were therefore partly reflected at the protein level, particularly for genes with strong and similarly timed induction.

4.2.3 GFP-derived pseudo mass fractions do not quantitatively reproduce protein mass fractions

The temporal comparison above tested whether GFP reporter and protein profiles changed with similar timing and shape. We next asked whether GFP-derived pseudo mass fractions could also approximate proteomics-derived protein mass fractions. To address this, the two quantities were compared directly across the sampled time points (fig. 4.6).

The quantitative correspondence between the two abundance estimates remained weak throughout the time course (fig. 4.6A). Pearson correlations calculated from the $\log_{10}$-transformed values ranged from approximately $r = 0.10$ to 0.23. Although the correlations increased during the early part of the experiment, they remained low at later time points. Thus, genes with higher GFP-derived pseudo mass fractions tended, on average, to have higher protein mass fractions, but this relationship was not sufficiently strong for quantitative estimation of protein expression levels. The limited correspondence was also apparent in the direct comparison at 10 h (fig. 4.6B). The $\log_{10}$-transformed values showed a positive Pearson correlation of $r = 0.23$, but the individual measurements were broadly distributed around the equal-abundance line and extended across several orders of magnitude. Many genes deviated by more than ten-fold from equal abundance. In addition, the median ratio of the GFP-derived pseudo mass fraction to the corresponding protein mass fraction was 6.4, indicating a systematic offset together with substantial gene-specific variation. Even at a time point with one of the highest observed correlations, GFP-derived pseudo mass fractions did not closely reproduce proteomics-derived protein mass fractions.

GFP reporter measurements therefore cannot be converted into protein mass fractions using a single general scaling factor. The reporter data were informative for comparing relative temporal regulation, but they did not provide reliable quantitative estimates of protein mass fraction.

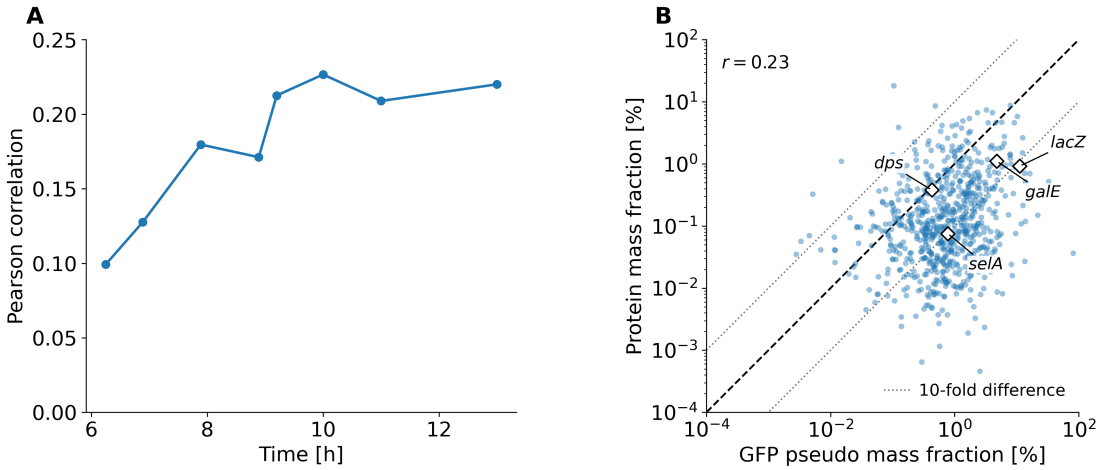


Figure 4.6: **Comparison of GFP-derived pseudo mass fractions and proteomics-derived protein mass fractions.** (A) Pearson correlations between $\log_{10}$-transformed values across the sampled time points. (B) Direct comparison at 10 h. The dashed line indicates equal abundance and the dotted lines indicate ten-fold deviations from equal abundance.

4.3 Discussion

The comparison showed a positive but moderate relationship between maximum-normalized GFP reporter and protein profiles, with a median Pearson correlation of $r = 0.25$ (fig. 4.4). Agreement varied strongly between genes. Some GFP profiles were also quite variable, particularly the weaker *galS* and *dps* signals (figs. 4.2 and 4.3). This variability makes their temporal patterns more difficult to interpret. GFP-derived pseudo mass fractions showed only weak quantitative agreement with proteomics-derived protein mass fractions (fig. 4.6). The reporter measurements therefore captured part of the relative temporal response, but not protein abundance quantitatively.

One reason for this difference is that the two measurements capture different stages of gene expression. The reporter library measures fluorescence from plasmid-based promoter–GFP fusions, whereas proteomics measures protein abundances [108]. The connection between the two is affected by mRNA stability, translation efficiency and protein turnover [98–100]. GFP maturation and dilution by growth further affect reporter dynamics [115, 116]. These processes are likely to matter especially during the diauxic shift, when the carbon source, growth rate and metabolic state are changing. Promoter induction and changes in protein abundance can therefore occur at different times. Strongly induced genes such as *lacZ* and *galE*

still showed similar reporter and protein profiles, whereas other proteins showed clear differences in timing. Time-series measurements during changes in carbon availability have similarly shown that changes in RNA and protein abundance can occur at different times [101].
Grouping genes at the transcription-unit level did not improve the agreement between the datasets. Operon organization alone therefore does not explain the moderate genome-wide relationship. Differences can also arise after promoter regulation or from the different time scales of reporter fluorescence and protein accumulation. Ribosomal proteins are a clear example because their abundance also depends on ribosome assembly, translation capacity, growth rate and global proteome allocation [3, 4, 117].
The measurements themselves also have limitations. GFP/OD represents accumulated fluorescence per biomass and is affected by GFP maturation, stability and growth dilution [115, 116]. Low background-subtracted OD values can further increase the uncertainty of the ratio. Only 28.4% of the reporters fulfilled the clear-signal criterion used here, showing that many reporters did not produce consistently strong signals under these conditions. The approximately 60% detectable fraction reported for the original library is not directly comparable because the studies used different signal definitions, background corrections and detection criteria [108].
Overall, the reporter library was most useful for detecting strong temporal responses and comparing relative profile dynamics. The differences from proteomics likely result from both biological processes acting between promoter activation and protein accumulation and limitations of the measurements. Reporter profiles should therefore not be interpreted as quantitative estimates of protein mass fraction.

4.4 Materials and Methods

4.4.1 Experimental methods

GFP reporter library and frozen stocks

Promoter-dependent GFP fluorescence during the glucose–lactose diauxic shift was measured using the *Escherichia coli* promoter reporter library [108]. In this library, promoter regions are fused to a fast-folding GFP reporter carried on a low-copy plasmid that also confers kanamycin resistance.
The library was distributed across 21 96-well plates. Plates 1–10 and 11–21 were processed as separate experimental batches. Reporter strains were diluted 1:1000 into medium containing 0.4% glucose and 25μg/mL kanamycin and grown for 24 h at 30°C. Glycerol was then added to a final concentration of 15% and the plates

were stored at −80°C.

Diauxic-shift experiment and measurements

Reporter strains were inoculated from the frozen working stocks into M9 minimal medium containing 0.4% glucose and 0.2% casamino acids. After 24 h at 30°C, the precultures were diluted 1:100 into M9 minimal medium supplemented with 0.03% glucose, 0.1% lactose and 25μg/mL kanamycin. Cultures were grown in flat-bottom 96-well plates at a final volume of 150μL per well.
The plates were incubated at 30°C, shaken at 500 rpm, and measured approximately every 40 min using a robotic system with an integrated incubator and plate reader. Optical density was measured at 600 nm. GFP fluorescence was measured using excitation and emission wavelengths of 485 and 535 nm, respectively. Promoterless reporter strains were included as fluorescence-background controls and wells containing medium without cells were used as optical-density controls where available.
For the proteomics time course, additional plates containing *E. coli* K-12 MG1655 without a GFP reporter were grown under the same diauxic-shift conditions, but without kanamycin. At approximately 6.25, 6.9, 7.9, 8.9, 9.2, 10, 11 and 13 h after inoculation, complete 96-well plates were removed and the cultures were pooled to obtain sufficient biomass for proteomics analysis.

4.4.2 Analysis

GFP and optical-density processing

Optical-density measurements were corrected by subtracting a fixed initial mean background value of 0.03. An OD-dependent fluorescence background, $B_{\mathrm{GFP}}(\mathrm{OD})$, was estimated from the promoterless reporters *U66* and *U139*.
The background-corrected GFP/OD profile was calculated as

$$\left(\frac{\mathrm{GFP}}{\mathrm{OD}}\right)_i(t) = \frac{\mathrm{GFP}_{\mathrm{raw},i}(t) - B_{\mathrm{GFP}}\left(\mathrm{OD}_{\mathrm{corr},i}(t)\right)}{\mathrm{OD}_{\mathrm{corr},i}(t)}. \tag{4.1}$$

GFP signal detection and replicate variability

A data-dependent threshold was used to distinguish clearly detectable reporter signals from weak or background-like measurements. After excluding the promoterless controls, the maximum positive GFP/OD value of each reporter was $\log_{10}$-transformed. Otsu thresholding was then used to divide the distribution into low- and high-signal populations [118]. The threshold was 2570.2 GFP/OD units. Reporters exceeding this threshold at three or more time points were classified as

clearly detectable. This classification was used to characterize the GFP dataset but not as an inclusion criterion for the genome-wide GFP–protein comparison. GFP/OD variability was estimated using the repeated *lacZ* control in well H1 of plates 1–20. For each experimental batch and time-point group, the coefficient of variation was calculated when at least two measurements were available and their mean exceeded the clear-signal threshold.

Identification of growth phases

The diauxic transition was estimated from the induction of the *lacZ*, *lacY*, *lacA*, *galE*, *galK*, *galT* and *galS* reporters. Each GFP/OD profile was smoothed using a centered five-point rolling median. For reporter i, the induction threshold was defined as

$$T_i = \max\left(0, B_i + 3\sigma_i, 0.20R_i^{\max}\right), \tag{4.2}$$

where B_i and σ_i are the median and standard deviation, respectively, of the measurements obtained up to 5 h and $R_i^{\max}$ is the maximum smoothed GFP/OD value. Induction onset was defined as the first time point after 5 h at which the smoothed profile reached or exceeded the threshold. The median onset time across the available markers was used as the estimated center of the diauxic transition. Because the reporter measurements were sampled at discrete time points and the induction onsets varied between markers, the transition was represented as an approximate time window around this value rather than as a single precise time point.
Stationary-phase onset was defined as the first time point after the diauxic transition at which the mean background-subtracted OD reached 90% of its maximum value.

Proteomics data processing

The proteomics data were processed as described in chapter 2 [3, 95].

Comparison of GFP reporter and protein dynamics

Genes in both datasets were retained if the GFP reporter had a positive signal at least once and the protein profile included at least four positive measurements. GFP/OD profiles were linearly interpolated to match the proteomics sampling times without extrapolation beyond the measured GFP time range.
For each gene, the GFP and protein profiles were normalized to their respective maximum values. Temporal similarity was quantified using the Pearson correlation coefficient between the two normalized profiles. At least four paired finite time points and nonzero variation in both profiles were required. Spearman rank

correlation was also calculated as a sensitivity analysis. Since the two profiles were normalized independently, the correlations describe similarity in temporal profile shape rather than agreement in absolute abundance.

Transcription-unit-level comparison

Genes were mapped to transcription units using EcoCyc annotations [113]. Genes assigned to several transcription units were retained in each unit, while genes without annotations were treated as single-gene entities.
For each transcription unit and time point, the summed GFP profiles of the assigned genes were calculated. The corresponding protein mass fractions were summed separately. The resulting profiles were interpolated, maximum-normalized and compared using the same Pearson correlation procedure as for the gene-level profiles.

GFP-derived pseudo mass fractions

To test whether GFP profiles could approximate protein mass fraction, the reporter signal was weighted by the molecular mass M_i of the corresponding protein. The GFP-derived pseudo mass fraction was calculated as

$$\widetilde{\phi}_i^{\mathrm{GFP}}(t) = \frac{M_i R_i(t)}{\sum_{j \in \mathcal{G}} M_j R_j(t)}, \tag{4.3}$$

where $R_i(t)$ is the GFP/OD profile of reporter i, M_i is the molecular mass of the corresponding protein and $\mathcal{G}$ is the set of reporters with protein molecular mass and GFP/OD measurements available.

5 Ultrasensitive fitness costs arise from membrane proteome displacement under protein overexpression

5.1 Publication

The following work, entitled *Ultrasensitive fitness costs arise from membrane proteome displacement under protein overexpression*, was published in *Cell Systems* in 2026 [119]. The published article is available at `https://doi.org/10.1016/j.cels.2026.101709`.

5.2 Contributions to the publication

Janina Müller, Gerrit Ansmann, Andreas Angermayr, Tobias Bollenbach and I contributed to this project. Janina Müller extended the genome-wide data analysis and performed most of the experiments. During the revision, I performed single-cell fluorescence microscopy and microfluidic time-lapse experiments, approximately doubling the amount of data shown in Figures 5 and 6 and Supplementary Figures 11 and 14. I also constructed strains required for these experiments by transforming the AtpD-YFP and PstB-YFP reporter strains with the respective overexpression plasmids.

6 Discussion and Outlook

The results of this thesis show that growth rate and proteome allocation explain important aspects of the physiological response of *E. coli*. However, these relationships did not hold equally well for every perturbation. Their usefulness depended on the affected cellular process, nutrient conditions and whether the cells were growing steadily or undergoing a dynamic transition. This discussion examines where growth laws and resource-allocation models were useful and where their limitations became apparent.

Translation and transcription inhibitors caused distinct changes in proteome allocation that helped explain their combined effects. Nutrient conditions strongly affected single-drug susceptibility and dose–response shapes, but most drug interaction types remained stable. During the diauxic shift, GFP reporter profiles and protein abundance described related but different aspects of the cellular response. The overexpression experiments revealed another limitation: a global proteome constraint was insufficient once membrane capacity became limiting.

6.1 How general are bacterial growth laws under different perturbations?

Chapter 2 demonstrates that the classical response to translation inhibition does not apply equally to all translation inhibitors. Chloramphenicol and erythromycin increased ribosome abundance as growth decreased, consistent with the second bacterial growth law [1, 2, 5]. Kasugamycin and streptomycin behaved differently and showed no increase in ribosome abundance. The allocation response therefore depends not only on growth rate but also on how translation is perturbed [94].
Within the same coarse-grained framework, these responses could be represented by allowing the ribosome-allocation slope to differ between antibiotics. In the model, stronger ribosome upregulation mainly increased the predicted IC_{50}. The basic growth-law framework could be retained while allowing drug-specific ribosome allocation to modify the relationship between growth and susceptibility [1, 62]. Why these allocation slopes differ remains unclear, but one possible contributor is (p)ppGpp signaling, which regulates ribosome synthesis and the allocation of cellular resources [26, 43, 120].
A second source of variation came from nutrient conditions (chapter 3). Both susceptibility and dose–response shape changed between growth environments, consistent with the coupling between growth physiology and the action of translation inhibitors [62]. The growth law-based model captured the direction of most susceptibility changes but not their magnitude. Drug-free growth rate alone was insufficient to explain the full response across nutrient conditions.
Rifampicin expanded this comparison beyond translation inhibition. Under rifampicin treatment, ribosome abundance decreased whereas RNA polymerase abundance increased. The increase in RNA polymerase is consistent with a compensatory allocation response to reduced transcriptional capacity [23]. The decrease in ribosome abundance resembles the response to poorer nutrient conditions [1, 5]. However, recent modeling suggests that the ribosome response to transcription inhibition can change with nutrient quality [23].
To distinguish drug-specific from state-dependent allocation, the whole-proteome measurements could be extended to antibiotic concentration series across several nutrient conditions. For the translation inhibitors, similar allocation slopes for each antibiotic across media would suggest that the response is mainly determined by the inhibited translation step. Changes in the slopes between media would instead indicate a stronger influence of the physiological state. A recent model predicts that transcription inhibition can decrease the ribosomal proteome fraction in richer media but increase it in poorer media [23].
Total ribosome abundance does not indicate how many ribosomes are actively translating or their elongation rates. Under slow growth, the fraction of actively

translating ribosomes decreases and chloramphenicol similarly causes a substantial reduction in the active ribosome pool [42]. Translation elongation rates could be measured using a time-resolved *lacZ* induction assay. Combining these measurements with growth rate and total ribosome abundance would allow the active ribosome fraction to be estimated [26, 42].
Comparing the active ribosome fraction and elongation rate between chloramphenicol, erythromycin, kasugamycin and streptomycin could help explain their different ribosome-allocation slopes. Under chloramphenicol, the increase in total ribosome abundance occurs together with a reduction in the active ribosome pool [1, 42]. Kasugamycin and streptomycin may affect these quantities differently, which could explain why total ribosome abundance does not increase under these drugs. Incorporating these measurements into the growth-law framework would separate total ribosome allocation from effective translational capacity.
The different ribosome responses may also be reflected in other growth-related properties such as cell size. Under nutrient limitation, slower-growing *E. coli* cells become smaller [121, 122], whereas cell size remains approximately constant when growth is reduced by sublethal chloramphenicol concentrations [122]. Measuring cell size under kasugamycin and streptomycin would test whether their different ribosome-allocation responses are accompanied by different cell-size responses at similar growth rates. Rifampicin provides a related comparison because transcription inhibition has been shown to reduce growth without a corresponding decrease in cell size under nutrient-rich conditions [123], despite the lower ribosome abundance observed here. If the ribosome-allocation response to rifampicin changes with nutrient quality [23], its cell-size response may also change with nutrient quality. Measurements across nutrient conditions using automated phase-contrast microscopy and single-cell segmentation would test this link [124, 125].

6.2 Can antibiotic interactions be predicted across physiological states?

The antibiotic combinations studied in chapter 2 tested whether the response to individual drugs provides information about their combined effects. Previous models addressed this question for pairs of translation inhibitors by combining single-drug dose–response curves with antibiotic transport, ribosome binding and the affected stage of translation [71, 88]. Here, this framework was extended to combinations targeting both transcription and translation.
Rifampicin and chloramphenicol produced opposing allocation responses and interacted antagonistically, whereas the ribosome-allocation responses to rifampicin and kasugamycin were less opposing and their interaction was closer to additive.

The generalized growth law-based model reproduced this difference using the allocation slopes of the individual antibiotics. The interaction therefore depended not only on the molecular targets of the drugs but also on how the cell redistributed its resources in response to each perturbation.
The proteome measurements showed a similar distinction. Under combined treatment, most protein abundances remained between the corresponding single-drug states. The transition was close to linear for rifampicin–kasugamycin but more switch-like for rifampicin–chloramphenicol. Thus, the proteome state under combined treatment was related to the states established by the individual drugs [126].
The experiments in chapter 3 asked whether this predictability is maintained when the physiological state changes. Nutrient conditions substantially altered single-drug susceptibility and dose–response shapes, while most interaction types remained relatively stable. Pairwise interactions were therefore more robust to changes in growth environment than the responses to the individual drugs. Properties that remain unchanged between nutrient conditions, such as the molecular targets and the affected stages of translation, may help explain why many interactions remained stable [71]. The nutrient-dependent exceptions show that these properties are not sufficient in every physiological state.
An important next test is whether the interactions between transcription and translation inhibitors are similarly robust across nutrient conditions. The experimental approach used in chapter 3 could be extended to combinations such as rifampicin–chloramphenicol and rifampicin–kasugamycin. This would test whether the contrasting interactions observed here remain stable when the drug-free physiological state changes.
If these interactions remain stable across defined nutrient conditions, the next question is whether this also holds in more complex environments. Nutrient and oxygen availability vary between infection environments and can affect both antibiotic susceptibility and drug interactions [80, 127, 128]. Interactions that change little across different nutrient conditions may be more likely to remain robust when the growth environment changes, whereas strongly condition-dependent interactions may be more sensitive to the local physiological state.
This robustness may also depend on the bacterial background. The same antibiotic combinations can behave differently between species and strains, including clinical isolates [81, 82, 129]. For clinical application, stability across nutrient conditions does not imply stability across different bacterial backgrounds. Resistance background and the infection environment become important when interaction measurements are transferred from laboratory to treatment settings [130].

6.3 What limits the predictive power of resource-allocation models?

The clearest limits of descriptions based on growth rate and proteome allocation emerged during dynamic growth transitions and membrane-protein overexpression. During the diauxic shift, GFP reporter profiles and protein abundance were related but followed different temporal dynamics (chapter 4). During membrane-protein overexpression, a finite global proteome budget was not sufficient to explain the strong growth defect (chapter 5). In both cases, proteome allocation remained informative but did not describe the full response.

The diauxic-shift experiments show one limitation of applying steady-state relationships during changing growth conditions. Under steady growth, promoter activity can be quantitatively related to protein concentration [19]. During the diauxic shift, expression changes continuously while proteins produced earlier remain present and are gradually diluted or degraded. Resource allocation during such transitions can also differ from that observed during steady growth [131]. The comparison between GFP reporters and proteomics also reflects differences between the two measurements. Reporter measurements provide densely sampled dynamics, but weak signals are difficult to quantify and the measured signal is affected by GFP maturation and growth dilution [115, 116]. Proteomics measures protein abundance but only at selected sampled time points. The two approaches therefore provide complementary information about the same transition.

Membrane-protein overexpression revealed a different type of constraint. Cytosolic overexpression was broadly consistent with a finite global proteome budget, whereas membrane proteins caused a much steeper growth defect [59, 132]. In chapter 5, this cost was linked to displacement of endogenous membrane proteins rather than saturation of the Sec pathway. Growth collapsed after only a small fraction of the membrane proteome was displaced. This indicates that membrane capacity imposes an additional constraint beyond global proteome allocation.

For the diauxic shift, denser measurements of promoter activity and protein abundance would help determine how quickly changes in gene expression are reflected in the proteome. High-throughput proteomics would allow more time points to be measured during the transition [133]. For membrane-protein overexpression, proteomics of membrane fractions and the total proteome across increasing expression levels could identify which endogenous membrane proteins are most affected as growth approaches collapse.

Growth rate and proteome allocation remain useful coarse-grained descriptions, but their predictive power depends on the perturbation. Dynamic growth requires information about the timing of expression changes, while membrane-protein overexpression introduces a compartment-specific constraint. Examining where these

frameworks reach their limits may therefore help uncover additional physiological mechanisms and guide the development of more complete descriptions of bacterial growth.

A Supplementary Information

A.1 Supplementary Information for chapter 2

The following supplementary material is shown from the supplementary information of the preprint [95] and provides the detailed derivation of the extended growth law-based model.

Supplementary Text

Extension of the growth law-based model of bacterial growth

This supplementary note describes an extension of the existing bacterial growth model based on growth laws [1–4], which we use to examine the effects of drug-specific ribosome responses on antibiotic susceptibility (Fig. S4) and drug interactions (Fig. 3). We extend the existing framework for ribosome-targeting antibiotics [2, 4] by allowing the ribosome–growth relation to vary among antibiotics. This difference is implemented via the phenomenological ribosome-response parameter θ, which captures different ribosome reallocation responses caused by antibiotic perturbations (Fig. 1). In the single-drug case, changes in θ primarily rescale susceptibility through an effective ribosome range Δr_θ (Fig. S4A). In the two-drug case, one drug alters the physiological background in which the second drug acts, making susceptibility background-dependent and generating non-additive drug interactions (Fig. 3).

Mathematical model for individual translation inhibitors

In line with previous models of microbial resource reallocation [1–4], we assume that growth is determined by the unbound ribosome pool r_u, which is related to the growth rate by the nutrient growth law

$$r_\mathrm{u}(\lambda) = r_\mathrm{min} + \frac{\lambda}{\kappa_\mathrm{t}}. \tag{1}$$

Here, λ is the growth rate under the considered condition, r_min is the inactive non-growth-associated ribosome concentration and κ_t is the translational capacity. The drug-free growth rate in the same nutrient background is denoted by λ_0. Since no ribosomes are drug-bound in the drug-free state, the total ribosome concentration at this reference point is

$$r_0 \equiv r_\mathrm{tot}(\lambda_0) = r_\mathrm{min} + \frac{\lambda_0}{\kappa_\mathrm{t}}. \tag{2}$$

The total ribosome concentration is $r_\mathrm{tot} = r_\mathrm{u} + r_\mathrm{b}$, where r_b is the drug-bound ribosome concentration. The quantity r_0 denotes the total ribosome concentration in the drug-free reference state.

Following [2], the dynamics of antibiotics inhibiting translation are described by transport across the cell envelope and reversible binding to ribosomes. Drug transport into the cell is written as the flux

$$J(a_{\mathrm{ex}}, a) = p_{\mathrm{in}} a_{\mathrm{ex}} - p_{\mathrm{out}} a, \tag{3}$$

where a_{ex} and a denote external and intracellular free drug concentrations, respectively. The parameters p_{in} and p_{out} describe effective influx and efflux permeabilities.
Drug binding to the growth-associated unbound ribosome pool is described by the net binding flux

$$f(r_{\mathrm{u}}, r_{\mathrm{b}}, a) = k_{\mathrm{on}} a \left(r_{\mathrm{u}} - r_{\mathrm{min}}\right) - k_{\mathrm{off}} r_{\mathrm{b}}, \tag{4}$$

where k_{on} and k_{off} are the binding and unbinding rates, respectively. The term $r_{\mathrm{u}} - r_{\mathrm{min}}$ represents the growth-associated unbound ribosome pool available for productive translation and drug binding. We assume that inactive ribosomes are not part of the ribosome pool accessible to the drug. In the model, r_{min} represents a ribosome fraction that does not contribute to productive translation. Changes in r_{min} between drugs are not explicitly represented.
We take dilution, drug transport and drug binding into account: The complete dynamical system reads:

$$\frac{\mathrm{d}a}{\mathrm{d}t} = -\lambda a - f(r_{\mathrm{u}}, r_{\mathrm{b}}, a) + J(a_{\mathrm{ex}}, a), \tag{5}$$

$$\frac{\mathrm{d}r_{\mathrm{u}}}{\mathrm{d}t} = -\lambda r_{\mathrm{u}} + s(\lambda) - f(r_{\mathrm{u}}, r_{\mathrm{b}}, a), \tag{6}$$

$$\frac{\mathrm{d}r_{\mathrm{b}}}{\mathrm{d}t} = -\lambda r_{\mathrm{b}} + f(r_{\mathrm{u}}, r_{\mathrm{b}}, a). \tag{7}$$

$s(\lambda)$ denotes the ribosome synthesis term. At steady state during balanced exponential growth, all time derivatives vanish and ribosome synthesis is given by $s(\lambda) = \lambda(r_{\mathrm{u}} + r_{\mathrm{b}})$.
With this sign convention, f is defined as the net flux into the drug-bound ribosome pool. A positive value of f means that free intracellular drug a and unbound ribosomes r_{u} are consumed, while drug-bound ribosomes r_{b} are produced. The binding flux therefore enters with a negative sign in the equations for a and r_{u} and with a positive sign in the equation for r_{b}.
A full derivation of the steady-state solution can be found in [2]. We summarize the main steps relevant for the generalized model.
Starting from the steady-state condition for bound ribosomes, Eq. (7) gives

$$0 = -\lambda r_{\mathrm{b}} + f. \tag{8}$$

Combining this relation with the binding flux in Eq. (4) gives

$$\left(\lambda + k_{\mathrm{off}}\right) r_{\mathrm{b}} = k_{\mathrm{on}} a \left(r_{\mathrm{u}} - r_{\mathrm{min}}\right). \tag{9}$$

Using the nutrient growth law in Eq. (1), the steady-state amount of drug-bound ribosomes becomes

$$r_{\mathrm{b}} = \frac{k_{\mathrm{on}} a \lambda}{\kappa_{\mathrm{t}} \left(\lambda + k_{\mathrm{off}}\right)}. \tag{10}$$

Substituting Eq. (10) into the steady-state drug balance, Eq. (5), gives

$$0 = -\left(\lambda + p_{\mathrm{out}}\right) a - \lambda r_{\mathrm{b}} + p_{\mathrm{in}} a_{\mathrm{ex}}. \tag{11}$$

Using Eq. (10), this can be written as

$$p_{\mathrm{in}} a_{\mathrm{ex}} = a \left[p_{\mathrm{out}} + \lambda + \frac{k_{\mathrm{on}} \lambda^2}{\kappa_{\mathrm{t}} \left(\lambda + k_{\mathrm{off}}\right)} \right]. \tag{12}$$

Thus, the intracellular drug concentration is

$$a = \frac{p_{\mathrm{in}} a_{\mathrm{ex}}}{p_{\mathrm{out}} + \lambda + \dfrac{k_{\mathrm{on}} \lambda^2}{\kappa_{\mathrm{t}} \left(\lambda + k_{\mathrm{off}}\right)}}. \tag{13}$$

To connect the drug-transport part of the model with the physiological ribosome balance, we first express the drug-bound ribosome concentration in terms of the external drug concentration and the growth rate. Substituting Eq. (13) into Eq. (10) gives

$$r_{\mathrm{b}}(a_{\mathrm{ex}}, \lambda) = \frac{k_{\mathrm{on}} p_{\mathrm{in}} a_{\mathrm{ex}} \lambda}{\kappa_{\mathrm{t}} \left(\lambda + k_{\mathrm{off}}\right) \left(p_{\mathrm{out}} + \lambda\right) + k_{\mathrm{on}} \lambda^2}. \tag{14}$$

This gives the kinetic expression for the amount of drug-bound ribosomes. In the next step, the same quantity is related to ribosome synthesis and growth through the steady-state ribosome balance.
The steady-state condition for unbound ribosomes, Eq. (6), is

$$0 = -\lambda r_{\mathrm{u}} + s(\lambda) - f. \tag{15}$$

Using Eq. (8), this becomes

$$s(\lambda) = \lambda \left(r_{\mathrm{u}} + r_{\mathrm{b}}\right) = \lambda r_{\mathrm{tot}}. \tag{16}$$

Equivalently,

$$s(\lambda) - \lambda r_{\mathrm{u}} = \lambda r_{\mathrm{b}}. \tag{17}$$

Using Eq. (1), this results in

$$s(\lambda) - \lambda r_{\mathrm{min}} - \frac{\lambda^2}{\kappa_{\mathrm{t}}} = \lambda r_{\mathrm{b}}. \tag{18}$$

Combining Eq. (18) with Eqs. (10) and (13) yields the compact steady-state identity

$$\left[s(\lambda) - \lambda r_{\mathrm{min}} - \frac{\lambda^2}{\kappa_{\mathrm{t}}} \right] D(\lambda) = k_{\mathrm{on}} p_{\mathrm{in}} a_{\mathrm{ex}} \lambda^2, \tag{19}$$

with

$$D(\lambda) = \kappa_t \left(\lambda + k_{off}\right)\left(p_{out} + \lambda\right) + k_{on}\lambda^2. \tag{20}$$

This equation forms the starting point for the generalized model. The kinetic contribution $D(\lambda)$, which contains transport and binding parameters, is separated from the physiological closure $s(\lambda)$, which describes how ribosome synthesis and proteome allocation change with growth rate. Drug kinetics and drug-induced proteome reorganization can be varied independently.

Generalized ribosome response for individual drugs

The established model assumes that total ribosome content increases linearly as the growth rate decreases due to translation inhibition [2]. More generally, different antibiotics induce distinct ribosome responses. While chloramphenicol treatment leads to strong compensatory ribosome upregulation, other perturbations, such as kasugamycin treatment or transcription limitation with rifampicin, produce substantially weaker or even opposite ribosome responses (Fig. 1). To account for these differences, we generalize the ribosome–growth relationship by introducing the phenomenological ribosome-response parameter θ:

$$r_{tot}(\lambda;\theta) = r_0 + \theta s_G \left(\lambda - \lambda_0\right). \tag{21}$$

Here, r_0 and λ_0 denote the drug-free reference state defined in Eq. (2). All generalized ribosome-response relations are required to pass through the same drug-free reference point (λ_0, r_0). This ensures that changing θ changes the response to inhibition, but not the drug-free baseline.
The slope s_G is defined as the slope between the drug-free point (λ_0, r_0) and the maximally inhibited ribosome state $r_{max} = r_{min} + \Delta r$, for chloramphenicol-like translation inhibition, as originally described [2],

$$\begin{aligned} s_G &= \frac{r_{max} - r_0}{0 - \lambda_0} \\ &= \frac{(r_{min} + \Delta r) - (r_{min} + \lambda_0/\kappa_t)}{-\lambda_0} \\ &= \frac{1}{\kappa_t} - \frac{\Delta r}{\lambda_0}. \end{aligned} \tag{22}$$

Setting $\theta = 1$ recovers the previously reported response [2]. Varying θ alters the strength and direction of the ribosome reallocation response while preserving the same drug-free reference point (λ_0, r_0). Here, $\theta = 1$ corresponds to the established ribosome increase of the second growth law, $0 < \theta < 1$ corresponds to a weaker increase, $\theta \approx 0$ corresponds to little or no drug-induced change in total ribosome content and $\theta < 0$ corresponds to a decrease in ribosome concentration in response to a drug.
Using Eq. (16), the synthesis term for the generalized closure is

$$s(\lambda) = \lambda r_{tot}(\lambda;\theta) = \lambda\left[r_0 + \theta s_G(\lambda - \lambda_0)\right]. \tag{23}$$

The physiological part of the steady-state identity is

$$B(\lambda) := s(\lambda) - \lambda r_{\min} - \frac{\lambda^2}{\kappa_t}. \tag{24}$$

Substituting Eq. (23) and applying $r_0 - r_{\min} = \lambda_0/\kappa_t$ yields

$$\begin{aligned} B(\lambda) &= \lambda r_0 + \theta s_G \lambda(\lambda - \lambda_0) - \lambda r_{\min} - \frac{\lambda^2}{\kappa_t} \\ &= \frac{\lambda\lambda_0}{\kappa_t} - \frac{\lambda^2}{\kappa_t} + \theta s_G \lambda(\lambda - \lambda_0) \\ &= \left(\frac{1}{\kappa_t} - \theta s_G\right) \lambda(\lambda_0 - \lambda). \end{aligned} \tag{25}$$

This motivates defining the effective ribosome range

$$\Delta r_\theta = \lambda_0 \left(\frac{1}{\kappa_t} - \theta s_G\right). \tag{26}$$

With this definition, Eq. (25) can be written as

$$B(\lambda) = \frac{\Delta r_\theta}{\lambda_0} \lambda(\lambda_0 - \lambda). \tag{27}$$

Substituting Eq. (27) into the general steady-state identity gives

$$\frac{\Delta r_\theta}{\lambda_0} \lambda(\lambda_0 - \lambda) D(\lambda) = k_{on} p_{in} a_{ex} \lambda^2. \tag{28}$$

For $\lambda > 0$, this becomes

$$(\lambda_0 - \lambda) D(\lambda) = \frac{k_{on} p_{in} a_{ex} \lambda_0}{\Delta r_\theta} \lambda. \tag{29}$$

Thus, the response parameter θ enters through the effective ribosome range Δr_θ, while the kinetic denominator $D(\lambda)$ remains unchanged.
At half-maximal growth, $\lambda = \lambda_0/2$, Eq. (29) gives

$$\mathrm{IC}_{50,\theta} = \frac{\Delta r_\theta}{k_{on} p_{in} \lambda_0} D\left(\frac{\lambda_0}{2}\right). \tag{30}$$

Relative to the previously reported case,

$$\mathrm{IC}_{50,\theta} = \mathrm{IC}_{50,G} \frac{\Delta r_\theta}{\Delta r}. \tag{31}$$

This shows that changing θ shifts susceptibility through proteome reorganization, while changes in dose-response shape require altered kinetic parameters, such as drug binding, unbinding, or transport. The generalized model remains physically meaningful only if

$$\Delta r_\theta > 0. \tag{32}$$

Strongly negative values of θ can violate this condition and lead to nonphysical solutions.

Generalized ribosome response for combinations of two drugs

Next, we extend the model to a drug combination setting, in which one drug modifies the physiological background and the other drug acts within this altered state. We use a reduced model for this conditional response. In the main orientation used below, drug X defines the background and drug Y is evaluated in this background. Rifampicin is an example of drug X. It is represented through its single-drug growth response and is not assumed to follow the same ribosome-binding kinetics as the translation inhibitors in the one-drug model. We represent the physiological state induced by the background drug by its growth rate and ribosome state. Other drug-induced changes in cellular physiology are not modeled separately.
The single-drug growth rate in the background generated by drug X is written as

$$\lambda_0(c_{\mathrm{X}}) = \lambda_{00} g_{\mathrm{X}}(c_{\mathrm{X}}), \qquad g_{\mathrm{X}}(0) = 1. \tag{33}$$

Here, c_{X} is the concentration of the background drug, λ_{00} is the growth rate in the absence of both drugs and $g_{\mathrm{X}}(c_{\mathrm{X}})$ is the normalized single-drug growth response of drug X.
We approximate the corresponding background ribosome level using the nutrient growth-law relation,

$$r_0(c_{\mathrm{X}}) = r_{\min} + \frac{\lambda_0(c_{\mathrm{X}})}{\kappa_{\mathrm{t}}}. \tag{34}$$

This is a modeling assumption for the X-only background state. It does not imply that the complete two-drug response follows the nutrient growth-law line. The corresponding background-dependent slope is

$$s_{\mathrm{G}}(c_{\mathrm{X}}) = \frac{1}{\kappa_{\mathrm{t}}} - \frac{\Delta r}{\lambda_0(c_{\mathrm{X}})}. \tag{35}$$

The effect of drug Y is evaluated within this X-dependent physiological state according to

$$r_{\mathrm{tot}}\left(\lambda; c_{\mathrm{X}}, \theta_{\mathrm{Y}}\right) = r_0(c_{\mathrm{X}}) + \theta_{\mathrm{Y}} s_{\mathrm{G}}(c_{\mathrm{X}}) \left[\lambda - \lambda_0(c_{\mathrm{X}})\right]. \tag{36}$$

Here, θ_{Y} is the ribosome-response parameter of the drug whose response is evaluated in the background. In this reduced model, θ_{Y} is treated as a drug-specific constant with respect to the background concentration c_{X}. This assumption could fail if the response class of drug Y changes strongly across different X-dependent backgrounds.
The effective susceptibility of drug Y therefore depends on the background through the scale $\lambda_0(c_{\mathrm{X}})/\Delta r_{\theta,\mathrm{Y|X}}(c_{\mathrm{X}})$. The effective ribosome range associated with the response to drug Y is

$$\Delta r_{\theta,\mathrm{Y|X}}(c_{\mathrm{X}}) = \lambda_0(c_{\mathrm{X}}) \left[\frac{1}{\kappa_{\mathrm{t}}} - \theta_{\mathrm{Y}} s_{\mathrm{G}}(c_{\mathrm{X}})\right]. \tag{37}$$

Using Eq. (35), this can be written as

$$\begin{aligned}\Delta r_{\theta,\mathrm{Y}|\mathrm{X}}(c_\mathrm{X}) &= \lambda_0(c_\mathrm{X})\left[\frac{1}{\kappa_\mathrm{t}} - \theta_\mathrm{Y}\left(\frac{1}{\kappa_\mathrm{t}} - \frac{\Delta r}{\lambda_0(c_\mathrm{X})}\right)\right] \\ &= (1-\theta_\mathrm{Y})\frac{\lambda_0(c_\mathrm{X})}{\kappa_\mathrm{t}} + \theta_\mathrm{Y}\Delta r.\end{aligned} \tag{38}$$

The same construction can be written after exchanging the two drugs. Drug Y then defines the background and drug X acts in this background. This gives

$$\Delta r_{\theta,\mathrm{X}|\mathrm{Y}}(c_\mathrm{Y}) = (1-\theta_\mathrm{X})\frac{\lambda_0(c_\mathrm{Y})}{\kappa_\mathrm{t}} + \theta_\mathrm{X}\Delta r. \tag{39}$$

The algebra has the same form after exchanging X and Y, but the response parameter belongs to the drug evaluated in the background. The $Y|X$ direction depends on θ_Y, while the $X|Y$ direction depends on θ_X. The two conditional descriptions need not give the same response.

We continue with the $X \to Y$ orientation, where drug X defines the background and drug Y is evaluated in this background. In the one-drug case, Δr_θ is constant for a given response class. In the two-drug case, the physiological background created by drug X changes the effective susceptibility scale of drug Y across the c_X-axis. Each fixed concentration of drug X defines a different effective one-dimensional dose-response curve for drug Y. These conditional dose-response curves form a two-dimensional response surface for the combination of the two drugs (Fig. 3).

The simple background closure in Eq. (34) assumes that the background ribosome level lies on the nutrient growth-law line. If the background drug changes ribosome allocation independently of this line, the background state could be written more generally as

$$R_\mathrm{X}(c_\mathrm{X}) = r_\mathrm{min} + \frac{\lambda_0(c_\mathrm{X})}{\kappa_\mathrm{t}} + \varepsilon_\mathrm{X}(c_\mathrm{X}), \tag{40}$$

where $\varepsilon_\mathrm{X}(c_\mathrm{X})$ describes the deviation of the X-only background from the nutrient growth-law line. The reduced model used here corresponds to the special case $\varepsilon_\mathrm{X}(c_\mathrm{X}) = 0$. This becomes important when the background perturbation is rifampicin-like rather than nutrient-like.

For each fixed background concentration c_X, the response to drug Y follows the same form as Eq. (29):

$$\left[\lambda_0(c_\mathrm{X}) - \lambda\right] D_\mathrm{Y}(\lambda) = \frac{k_{\mathrm{on,Y}} p_{\mathrm{in,Y}} c_\mathrm{Y} \lambda_0(c_\mathrm{X})}{\Delta r_{\theta,\mathrm{Y}|\mathrm{X}}(c_\mathrm{X})}\lambda, \tag{41}$$

with

$$D_\mathrm{Y}(\lambda) = \kappa_\mathrm{t}\left(\lambda + k_{\mathrm{off,Y}}\right)\left(p_{\mathrm{out,Y}} + \lambda\right) + k_{\mathrm{on,Y}}\lambda^2. \tag{42}$$

Here, c_Y is the external concentration of drug Y and $k_{\mathrm{on,Y}}$, $k_{\mathrm{off,Y}}$, $p_{\mathrm{in,Y}}$ and $p_{\mathrm{out,Y}}$ are the kinetic parameters of drug Y.

Changes in the effective susceptibility scale

$$\lambda_0(c_{\mathrm{X}})/\Delta r_{\theta,\mathrm{Y|X}}(c_{\mathrm{X}})$$

with the background concentration c_{X} can contribute to curvature of the drug interaction surface. Part of this dependence comes from changes in the effective ribosome range. Differentiating Eq. (37) with respect to c_{X} gives

$$\frac{\mathrm{d}\Delta r_{\theta,\mathrm{Y|X}}(c_{\mathrm{X}})}{\mathrm{d}c_{\mathrm{X}}} = \lambda_0'(c_{\mathrm{X}})\left[\frac{1}{\kappa_{\mathrm{t}}} - \theta_{\mathrm{Y}} s_{\mathrm{G}}(c_{\mathrm{X}})\right] - \lambda_0(c_{\mathrm{X}})\theta_{\mathrm{Y}} s_{\mathrm{G}}'(c_{\mathrm{X}}). \tag{43}$$

The first term reflects the change in background growth rate caused by drug X. The second term reflects the change in the growth-law slope and is weighted by the proteome-response class θ_{Y}.
Using the expanded expression in Eq. (38), the $Y|X$ susceptibility scale can be written as

$$S_{\mathrm{Y|X}}(c_{\mathrm{X}}) = \frac{\lambda_0(c_{\mathrm{X}})}{\Delta r_{\theta,\mathrm{Y|X}}(c_{\mathrm{X}})} = \frac{\lambda_0(c_{\mathrm{X}})}{(1-\theta_{\mathrm{Y}})\lambda_0(c_{\mathrm{X}})/\kappa_{\mathrm{t}} + \theta_{\mathrm{Y}}\Delta r}. \tag{44}$$

The two limiting cases illustrate how this background dependence changes with θ_{Y}. For $\theta_{\mathrm{Y}} = 1$, corresponding to a strong compensatory ribosome response, the effective ribosome range becomes

$$\Delta r_{\theta,\mathrm{Y|X}}(c_{\mathrm{X}}) = \Delta r, \tag{45}$$

Therefore

$$S_{\mathrm{Y|X}}(c_{\mathrm{X}}) = \frac{\lambda_0(c_{\mathrm{X}})}{\Delta r}. \tag{46}$$

Thus, for $\theta_{\mathrm{Y}} = 1$, the susceptibility scale remains directly proportional to the background growth rate $\lambda_0(c_{\mathrm{X}})$.
For $\theta_{\mathrm{Y}} = 0$, corresponding to little or no additional drug-induced ribosome reallocation by drug Y, the effective ribosome range becomes

$$\Delta r_{\theta,\mathrm{Y|X}}(c_{\mathrm{X}}) = \frac{\lambda_0(c_{\mathrm{X}})}{\kappa_{\mathrm{t}}}, \tag{47}$$

and therefore

$$S_{\mathrm{Y|X}}(c_{\mathrm{X}}) = \frac{\lambda_0(c_{\mathrm{X}})}{\lambda_0(c_{\mathrm{X}})/\kappa_{\mathrm{t}}} = \kappa_{\mathrm{t}}. \tag{48}$$

Thus, for $\theta_{\mathrm{Y}} = 0$, the explicit $\lambda_0(c_{\mathrm{X}})$ factor cancels from the $Y|X$ susceptibility scale. The response of drug Y therefore no longer depends on the background growth rate through this term.
The same cancellation argument applies after exchanging the drugs. In the $X|Y$ direction, the corresponding susceptibility scale is

$$S_{\mathrm{X|Y}}(c_{\mathrm{Y}}) = \frac{\lambda_0(c_{\mathrm{Y}})}{\Delta r_{\theta,\mathrm{X|Y}}(c_{\mathrm{Y}})}. \tag{49}$$

The analogous cancellation occurs only if $\theta_{\mathrm{X}} = 0$:

$$\Delta r_{\theta,\mathrm{X}|\mathrm{Y}}(c_{\mathrm{Y}}) = \frac{\lambda_0(c_{\mathrm{Y}})}{\kappa_{\mathrm{t}}} \quad \Rightarrow \quad S_{\mathrm{X}|\mathrm{Y}}(c_{\mathrm{Y}}) = \kappa_{\mathrm{t}}. \tag{50}$$

A value of $\theta_{\mathrm{Y}} = 0$ does not by itself imply that the conditional $Y|X$ response is additive. It only removes one source of background-growth dependence in this direction. After exchanging the drugs, the corresponding result depends on θ_{X}.

Drug-drug growth surface

A two-drug growth surface can be written as

$$\lambda = F(c_{\mathrm{X}}, c_{\mathrm{Y}}). \tag{51}$$

An isobole is a contour of equal growth,

$$F(c_{\mathrm{X}}, c_{\mathrm{Y}}) = \lambda^*. \tag{52}$$

Implicit differentiation along this contour gives

$$\frac{\mathrm{d}c_{\mathrm{Y}}}{\mathrm{d}c_{\mathrm{X}}} = -\frac{\partial F/\partial c_{\mathrm{X}}}{\partial F/\partial c_{\mathrm{Y}}}. \tag{53}$$

An isobole is curved when this ratio changes along the contour. In this reduced model, Eq. (53) describes the geometry of isobole curvature but does not provide a closed-form condition for additivity. The growth surface itself is obtained from the conditional dose-response equation, Eq. (41).
One source of curvature is the background-dependent susceptibility scale $S_{\mathrm{Y}|\mathrm{X}}(c_{\mathrm{X}})$. For $\theta_{\mathrm{Y}} = 1$, this scale remains proportional to the background growth rate $\lambda_0(c_{\mathrm{X}})$. For $\theta_{\mathrm{Y}} = 0$, the explicit $\lambda_0(c_{\mathrm{X}})$ factor cancels from this scale. This reduces one source of background dependence in the $Y|X$ direction.
This result applies to the $Y|X$ direction. In the exchanged $X|Y$ direction, the corresponding cancellation requires $\theta_{\mathrm{X}} = 0$. Thus, the two conditional descriptions need not give the same response.
For rifampicin–chloramphenicol, the model should therefore be interpreted phenomenologically. Rifampicin is used as drug X, which creates a transcription-limited background through $\lambda_0(c_{\mathrm{X}})$, while chloramphenicol acts as drug Y and is represented by a strong ribosome-upregulation response, $\theta_{\mathrm{Y}} \approx 1$. For rifampicin–kasugamycin, kasugamycin has a weaker ribosome reallocation response, so $\theta_{\mathrm{Y}} \approx 0$ is a plausible phenomenological description. In this reduced model, the kasugamycin response can therefore depend less strongly on the background than the chloramphenicol response.
Because the two drugs have different roles in this model, the response may depend on treatment order. The state generated by drug X before adding drug Y may differ from the state generated when the order is reversed. This could be tested experimentally by treating cells first with one drug and then with the other. The present steady-state model does not describe these time-dependent effects.

References

1. Scott, M. & Hwa, T. Bacterial growth laws and their applications. en. *Current Opinion in Biotechnology* **22,** 559–565 (Aug. 2011).
2. Greulich, P., Scott, M., Evans, M. R. & Allen, R. J. Growth-dependent bacterial susceptibility to ribosome-targeting antibiotics. en. *Molecular Systems Biology* **11,** MSB145949 (Mar. 2015).
3. Kavčič, B., Tkačik, G. & Bollenbach, T. Mechanisms of drug interactions between translation-inhibiting antibiotics. en. *Nature Communications* **11,** 4013 (Aug. 2020).
4. Kavčič, B., Tkačik, G. & Bollenbach, T. Minimal biophysical model of combined antibiotic action. en. *PLOS Computational Biology* **17** (ed Grilli, J.) e1008529 (Jan. 2021).

A.2 Supplementary Information for chapter 3

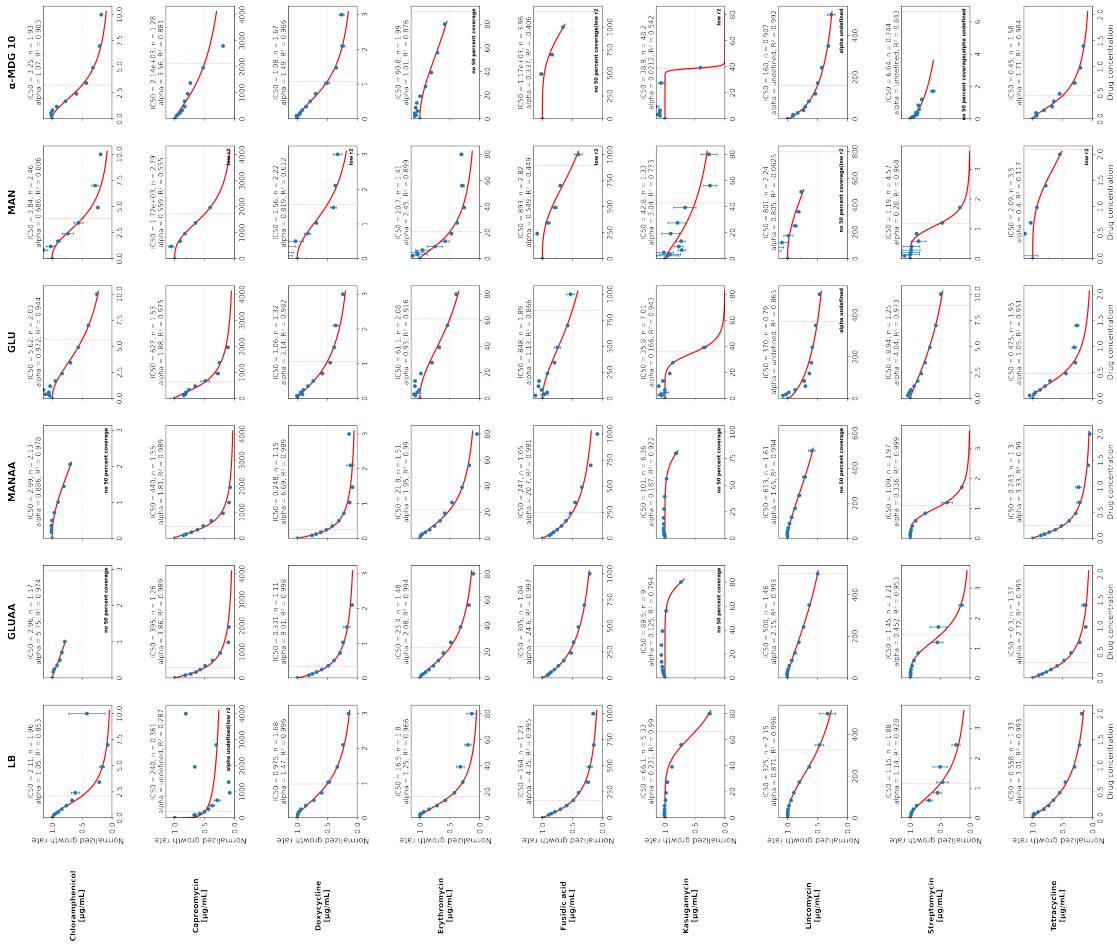


Figure A.1: **Complete single-drug fits.** Columns correspond to LB, GLUAA, MANAA, GLU, MAN and α-MG-10; rows correspond to the translation inhibitors. Blue points and error bars show the normalized growth data and red curves show fits of eq. (3.1). The horizontal dotted line marks $y = 0.5$ and the vertical dotted line marks the fitted IC_{50}.

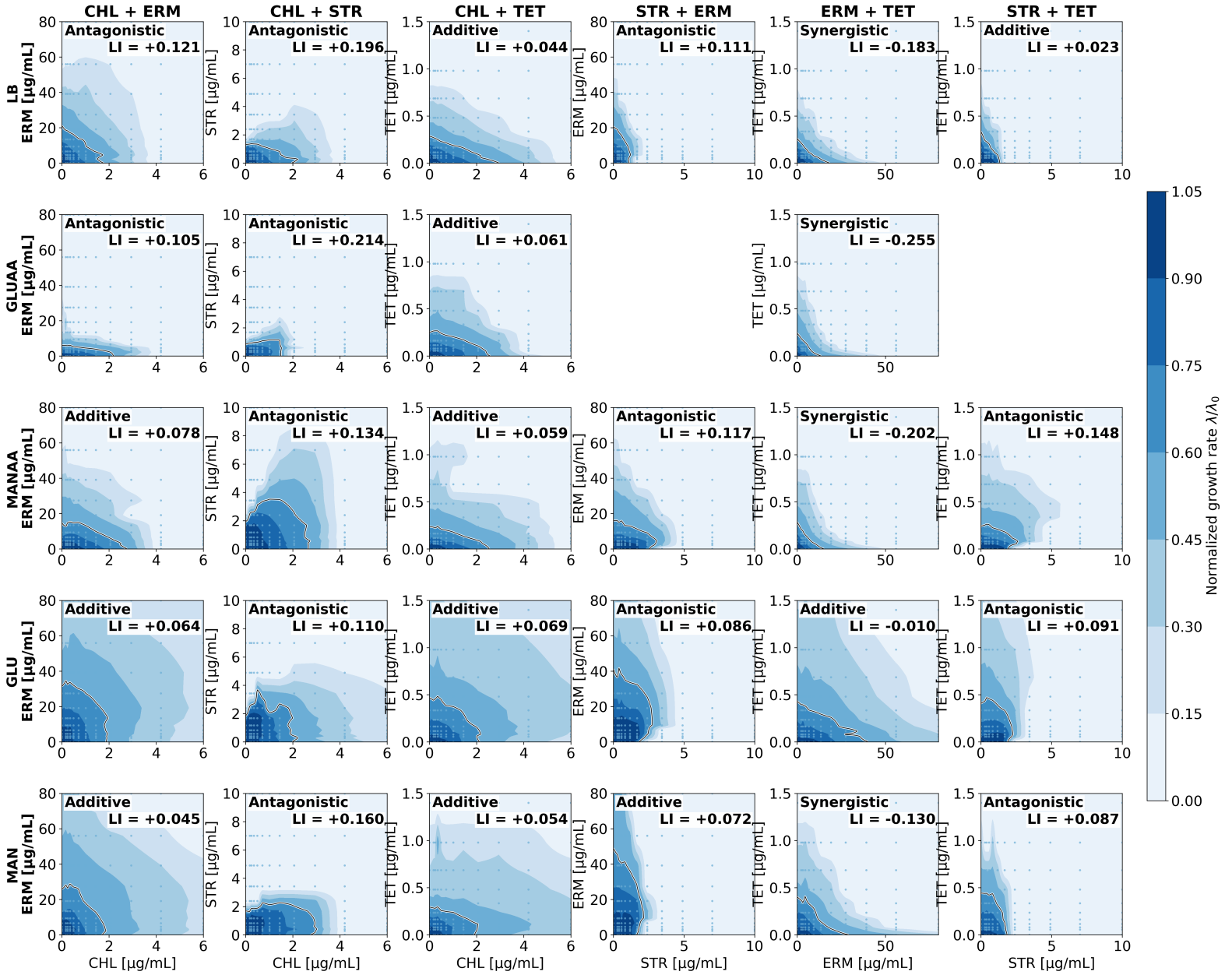


Figure A.2: **Complete measured two-drug growth surfaces.** Rows correspond to LB, GLUAA, MANAA, GLU and MAN, while columns correspond to CHL–ERM, CHL–STR, CHL–TET, STR–ERM, ERM–TET and STR–TET. Colors indicate growth normalized to the drug-free growth rate. The solid contour marks the 50% growth isobole.

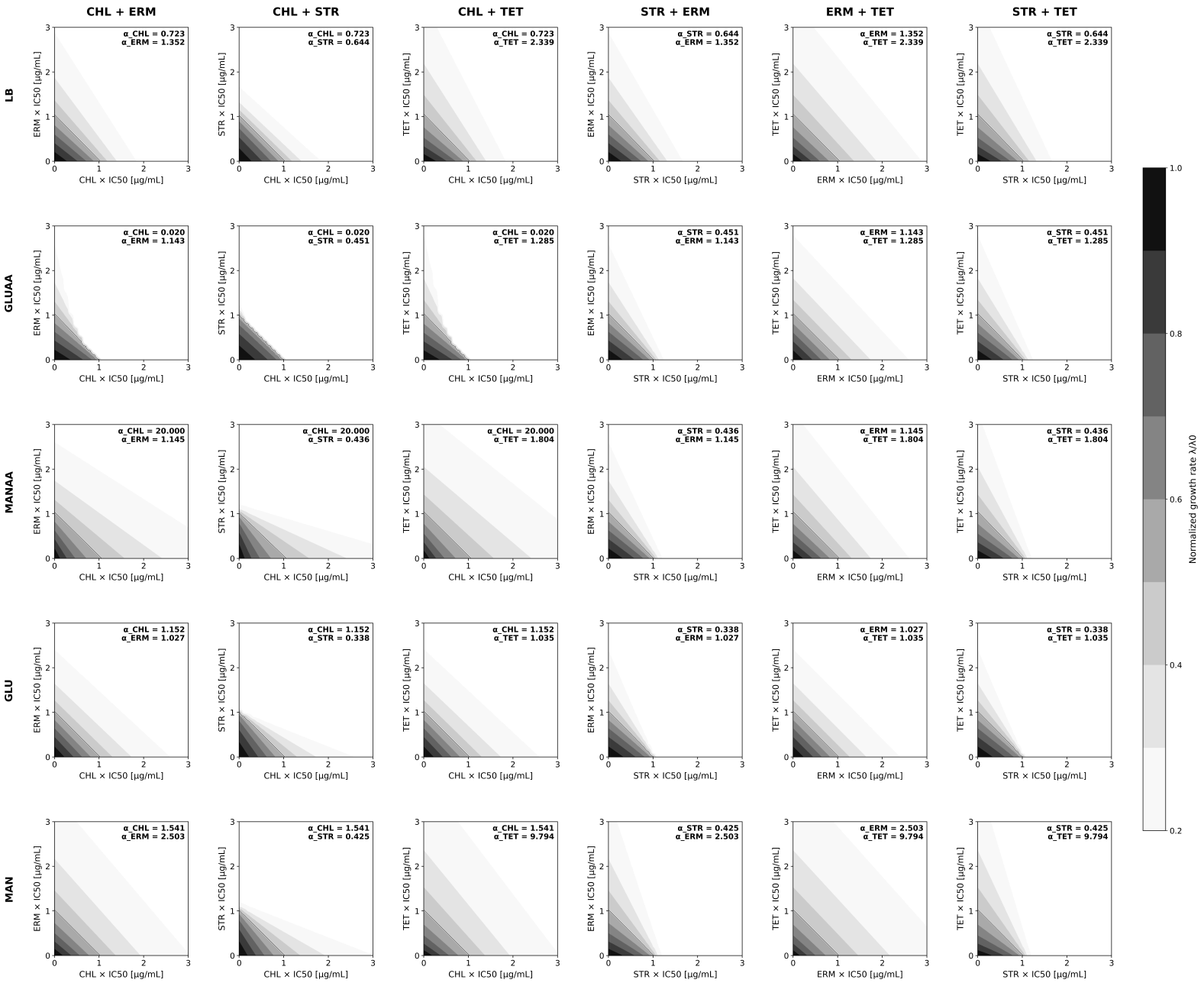


Figure A.3: **Complete competitive-binding model predictions.** Rows correspond to LB, GLUAA, MANAA, GLU and MAN, while columns correspond to CHL–ERM, CHL–STR, CHL–TET, STR–ERM, ERM–TET and STR–TET. Drug concentrations are normalized by the corresponding IC_{50} values. Gray levels indicate predicted growth normalized to the drug-free growth rate, λ/λ_0. Panel annotations show the fitted single-drug α values used for each prediction.

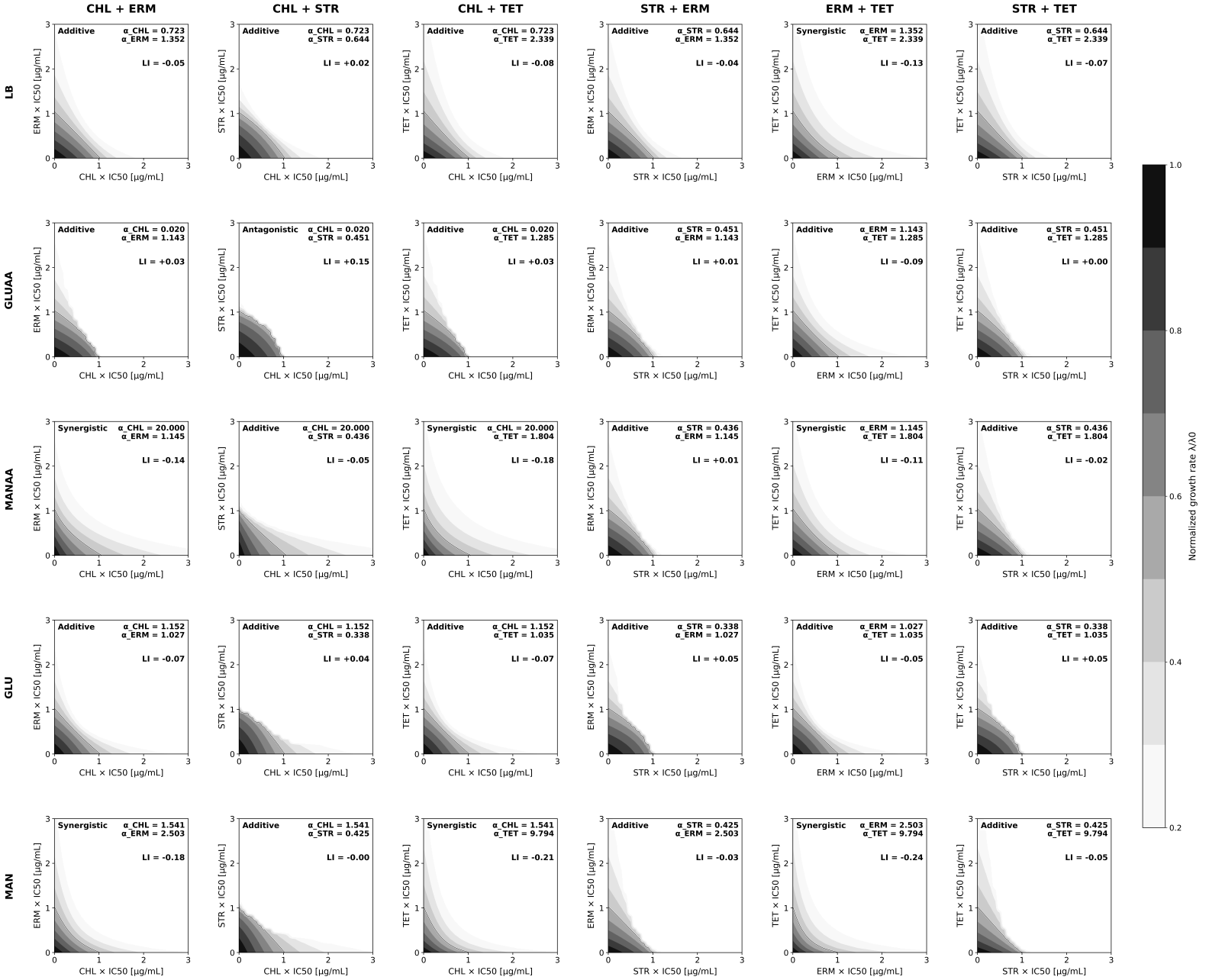


Figure A.4: **Complete independent-binding model predictions.** Rows correspond to LB, GLUAA, MANAA, GLU and MAN, while columns correspond to CHL–ERM, CHL–STR, CHL–TET, STR–ERM, ERM–TET and STR–TET. Drug concentrations are normalized by the corresponding IC_{50} values. Gray levels indicate predicted growth normalized to the drug-free growth rate, λ/λ_0. Panel annotations show the fitted single-drug α values, the predicted Loewe interaction score and the corresponding interaction class.

List of Figures

1.1 Bacterial growth in batch culture and during serial dilution. . . . 3
1.2 Schematic of gene expression in bacteria. 4
1.3 Schematic of bacterial transcription. 6
1.4 Schematic of bacterial translation. 8
1.5 Schematic of bacterial membrane protein biogenesis. 12
1.6 Drug interactions defined by Loewe additivity. 17
1.7 Proteome partitioning and ribosome-centered bacterial growth laws. 21
1.8 Molecular mechanisms underlying changes in translational capacity. 24
1.9 Growth law-based model of translation inhibition. 26
1.10 Prediction of interactions between two translation inhibitors. . . . 27

3.1 Drug-free growth rates across nutrient conditions 82
3.2 Single-drug growth law fits 83
3.3 Growth law relation and nutrient-dependent susceptibility changes 84
3.4 Representative measured two-drug interactions 85
3.5 Drug interaction scores across nutrient conditions 86
3.6 Nutrient-dependent changes in drug interactions 87
3.7 Representative model interactions 88
3.8 Measured and predicted drug interaction scores 89

4.1 Experimental setup for comparing GFP reporter dynamics and protein abundance during the diauxic shift. 96
4.2 Characterization of GFP reporter and proteomics measurements during the diauxic shift. 99
4.3 Individual GFP profiles of *galS* and *dps*. 100
4.4 Genome-wide comparison of maximum-normalized GFP reporter and protein abundance dynamics. 101
4.5 Representative maximum-normalized GFP reporter and protein abundance profiles. 102
4.6 Comparison of GFP-derived pseudo mass fractions and proteomics-derived protein mass fractions. 104

A.1 Complete single-drug fits 129
A.2 Complete measured two-drug growth surfaces 130
A.3 Complete competitive-binding model predictions 131

A.4 Complete independent-binding model predictions 132

List of Tables

1.1 Antibiotics investigated in this thesis. 15

Bibliography

[1] Matthew Scott, Carl W. Gunderson, Eduard M. Mateescu, Zhongge Zhang, and Terence Hwa. Interdependence of Cell Growth and Gene Expression: Origins and Consequences. *Science*, 330(6007):1099–1102, November 2010. ISSN 0036-8075, 1095-9203. doi: 10.1126/science.1192588. URL `https://www.science.org/doi/10.1126/science.1192588`.

[2] Matthew Scott and Terence Hwa. Bacterial growth laws and their applications. *Current Opinion in Biotechnology*, 22(4):559–565, August 2011. ISSN 09581669. doi: 10.1016/j.copbio.2011.04.014. URL `https://linkinghub.elsevier.com/retrieve/pii/S0958166911000772`.

[3] Matteo Mori, Zhongge Zhang, Amir Banaei-Esfahani, Jean-Benoît Lalanne, Hiroyuki Okano, Ben C Collins, Alexander Schmidt, Olga T Schubert, Deok-Sun Lee, Gene-Wei Li, Ruedi Aebersold, Terence Hwa, and Christina Ludwig. From coarse to fine: the absolute Escherichia coli proteome under diverse growth conditions. *Molecular Systems Biology*, 17(5):MSB20209536, May 2021. ISSN 1744-4292. doi: 10.15252/msb.20209536. URL `https://link.springer.com/10.15252/msb.20209536`.

[4] Gene-Wei Li, David Burkhardt, Carol Gross, and Jonathan S. Weissman. Quantifying Absolute Protein Synthesis Rates Reveals Principles Underlying Allocation of Cellular Resources. *Cell*, 157(3):624–635, April 2014. ISSN 00928674. doi: 10.1016/j.cell.2014.02.033. URL `https://linkinghub.elsevier.com/retrieve/pii/S0092867414002323`.

[5] Sheng Hui, Josh M Silverman, Stephen S Chen, David W Erickson, Markus Basan, Jilong Wang, Terence Hwa, and James R Williamson. Quantitative proteomic analysis reveals a simple strategy of global resource allocation in bacteria. *Molecular Systems Biology*, 11(2):MSB145697, February 2015. ISSN 1744-4292. doi: 10.15252/msb.20145697. URL `https://link.springer.com/10.15252/msb.20145697`.

[6] S Andreas Angermayr, Tin Yau Pang, Guillaume Chevereau, Karin Mitosch, Martin J Lercher, and Tobias Bollenbach. Growth-mediated negative feedback shapes quantitative antibiotic response. *Molecular Systems Biology*, 18(9):

MSB202110490, September 2022. ISSN 1744-4292. doi: 10.15252/msb.202110490. URL https://link.springer.com/10.15252/msb.202110490.

[7] M. Schaechter, O. Maaløe, and N. O. Kjeldgaard. Dependency on Medium and Temperature of Cell Size and Chemical Composition during Balanced Growth of Salmonella typhimurium. *Journal of General Microbiology*, 19(3):592–606, December 1958. ISSN 0022-1287. doi: 10.1099/00221287-19-3-592. URL https://www.microbiologyresearch.org/content/journal/micro/10.1099/00221287-19-3-592.

[8] Rossana Droghetti, Mattia Corigliano, Ludovico Calabrese, Philippe Fuchs, Abhishek Vaidyanathan, Johannes Keisers, Gabriele Micali, Marco Cosentino Lagomarsino, and Luca Ciandrini. Hands-On Growth Laws Theory Cookbook. *PRX Life*, 4(1):012001, March 2026. ISSN 2835-8279. doi: 10.1103/x33x-srz4. URL https://link.aps.org/doi/10.1103/x33x-srz4.

[9] Susana Matamouros, Thomas Gensch, Martin Cerff, Christian C. Sachs, Iman Abdollahzadeh, Johnny Hendriks, Lucas Horst, Niklas Tenhaef, Julia Tenhaef, Stephan Noack, Michaela Graf, Ralf Takors, Katharina Nöh, and Michael Bott. Growth-rate dependency of ribosome abundance and translation elongation rate in Corynebacterium glutamicum differs from that in Escherichia coli. *Nature Communications*, 14(1):5611, September 2023. ISSN 2041-1723. doi: 10.1038/s41467-023-41176-y. URL https://www.nature.com/articles/s41467-023-41176-y.

[10] Arthur L. Koch. Turbidity measurements of bacterial cultures in some available commercial instruments. *Analytical Biochemistry*, 38(1):252–259, November 1970. ISSN 00032697. doi: 10.1016/0003-2697(70)90174-0. URL https://linkinghub.elsevier.com/retrieve/pii/0003269770901740.

[11] Keiran Stevenson, Alexander F. McVey, Ivan B. N. Clark, Peter S. Swain, and Teuta Pilizota. General calibration of microbial growth in microplate readers. *Scientific Reports*, 6(1):38828, December 2016. ISSN 2045-2322. doi: 10.1038/srep38828. URL https://www.nature.com/articles/srep38828.

[12] Jacques Monod. The Growth of Bacterial Cultures. *Annual Review of Microbiology*, 3:371–394, 1949. doi: 10.1146/annurev.mi.03.100149.002103.

[13] Allan Campbell. SYNCHRONIZATION OF CELL DIVISION. *Bacteriological Reviews*, 21(4):263–272, December 1957. ISSN 0005-3678. doi: 10.1128/br.21.4.263-272.1957. URL https://pmc.ncbi.nlm.nih.gov/articles/PMC180914/.

[14] A. L. Koch. The adaptive responses of Escherichia coli to a feast and famine existence. *Advances in Microbial Physiology*, 6:147–217, 1971. ISSN 0065-2911. doi: 10.1016/s0065-2911(08)60069-7.

[15] H. Bremer and G. Churchward. An examination of the Cooper-Helmstetter theory of DNA replication in bacteria and its underlying assumptions. *Journal of Theoretical Biology*, 69(4):645–654, December 1977. ISSN 00225193. doi: 10.1016/0022-5193(77)90373-3. URL https://linkinghub.elsevier.com/retrieve/pii/0022519377903733.

[16] Hans Bremer and Patrick P. Dennis. Modulation of Chemical Composition and Other Parameters of the Cell at Different Exponential Growth Rates. *EcoSal Plus*, 3(1):10.1128/ecosal.5.2.3, January 2008. ISSN 2324-6200. doi: 10.1128/ecosal.5.2.3. URL https://journals.asm.org/doi/10.1128/ecosal.5.2.3.

[17] Patrick P. Dennis and Hans Bremer. Macromolecular Composition During Steady-State Growth of *Escherichia coli* B/r. *Journal of Bacteriology*, 119 (1):270–281, July 1974. ISSN 0021-9193, 1098-5530. doi: 10.1128/jb.119.1.270-281.1974. URL https://journals.asm.org/doi/10.1128/jb.119.1.270-281.1974.

[18] Stefan Klumpp, Zhongge Zhang, and Terence Hwa. Growth Rate-Dependent Global Effects on Gene Expression in Bacteria. *Cell*, 139(7):1366–1375, December 2009. ISSN 00928674. doi: 10.1016/j.cell.2009.12.001. URL https://linkinghub.elsevier.com/retrieve/pii/S0092867409015050.

[19] Rohan Balakrishnan, Matteo Mori, Igor Segota, Zhongge Zhang, Ruedi Aebersold, Christina Ludwig, and Terence Hwa. Principles of gene regulation quantitatively connect DNA to RNA and proteins in bacteria. *Science*, 378(6624):eabk2066, December 2022. ISSN 0036-8075, 1095-9203. doi: 10.1126/science.abk2066. URL https://www.science.org/doi/10.1126/science.abk2066.

[20] Francis Crick. Central Dogma of Molecular Biology. *Nature*, 227(5258): 561–563, 1970. doi: 10.1038/227561a0.

[21] Sukanya Iyer, Dai Le, Bo Ryoung Park, and Minsu Kim. Distinct mechanisms coordinate transcription and translation under carbon and nitrogen starvation in Escherichia coli. *Nature Microbiology*, 3(6):741–748, June 2018. ISSN 2058-5276. doi: 10.1038/s41564-018-0161-3. URL https://doi.org/10.1038/s41564-018-0161-3.

[22] Qing Zhang, Elisa Brambilla, Rui Li, Hualin Shi, Marco Cosentino Lagomarsino, and Bianca Sclavi. A Decrease in Transcription Capacity Limits Growth Rate upon Translation Inhibition. *mSystems*, 5(5):e00575–20, October 2020. ISSN 2379-5077. doi: 10.1128/mSystems.00575-20. URL https://journals.asm.org/doi/10.1128/mSystems.00575-20.

[23] Ludovico Calabrese, Luca Ciandrini, and Marco Cosentino Lagomarsino. How total mRNA influences cell growth. *Proceedings of the National Academy of Sciences*, 121(21):e2400679121, May 2024. ISSN 0027-8424, 1091-6490. doi: 10.1073/pnas.2400679121. URL https://pnas.org/doi/10.1073/pnas.2400679121.

[24] Mikel Irastortza-Olaziregi and Orna Amster-Choder. Coupled Transcription-Translation in Prokaryotes: An Old Couple With New Surprises. *Frontiers in Microbiology*, 11:624830, January 2021. ISSN 1664-302X. doi: 10.3389/fmicb.2020.624830. URL https://www.frontiersin.org/articles/10.3389/fmicb.2020.624830/full.

[25] Marina V. Rodnina. Translation in Prokaryotes. *Cold Spring Harbor Perspectives in Biology*, 10(9):a032664, September 2018. ISSN 1943-0264. doi: 10.1101/cshperspect.a032664. URL http://cshperspectives.cshlp.org/lookup/doi/10.1101/cshperspect.a032664.

[26] Manlu Zhu and Xiongfeng Dai. Growth suppression by altered (p)ppGpp levels results from non-optimal resource allocation in Escherichia coli. *Nucleic Acids Research*, 47(9):4684–4693, May 2019. ISSN 0305-1048, 1362-4962. doi: 10.1093/nar/gkz211. URL https://academic.oup.com/nar/article/47/9/4684/5420536.

[27] Andrey Feklístov, Brian D. Sharon, Seth A. Darst, and Carol A. Gross. Bacterial Sigma Factors: A Historical, Structural, and Genomic Perspective. *Annual Review of Microbiology*, 68(1):357–376, September 2014. ISSN 0066-4227, 1545-3251. doi: 10.1146/annurev-micro-092412-155737. URL https://www.annualreviews.org/doi/10.1146/annurev-micro-092412-155737.

[28] Gregor M. Blaha and Joseph T. Wade. Transcription-Translation Coupling in Bacteria. *Annual Review of Genetics*, 56(1):187–205, November 2022. ISSN 0066-4197, 1545-2948. doi: 10.1146/annurev-genet-072220-033342. URL https://www.annualreviews.org/doi/10.1146/annurev-genet-072220-033342.

[29] Sergei Borukhov, Valery Sagitov, and Alex Goldfarb. Transcript cleavage factors from E. coli. *Cell*, 72(3):459–466, February 1993. ISSN 00928674.

doi: 10.1016/0092-8674(93)90121-6. URL https://linkinghub.elsevier.com/retrieve/pii/0092867493901216.

[30] Oleg Laptenko, Jookyung Lee, Ivan Lomakin, and Sergei Borukhov. Transcript cleavage factors GreA and GreB act as transient catalytic components of RNA polymerase. *The EMBO Journal*, 22(23):6322–6334, December 2003. ISSN 0261-4189, 1460-2075. doi: 10.1093/emboj/cdg610. URL https://link.springer.com/10.1093/emboj/cdg610.

[31] Vasili Hauryliuk, Gemma C. Atkinson, Katsuhiko S. Murakami, Tanel Tenson, and Kenn Gerdes. Recent functional insights into the role of (p)ppGpp in bacterial physiology. *Nature Reviews Microbiology*, 13(5):298–309, May 2015. ISSN 1740-1526, 1740-1534. doi: 10.1038/nrmicro3448. URL https://www.nature.com/articles/nrmicro3448.

[32] Sophie E. Irving, Naznin R. Choudhury, and Rebecca M. Corrigan. The stringent response and physiological roles of (pp)pGpp in bacteria. *Nature Reviews Microbiology*, 19(4):256–271, April 2021. ISSN 1740-1526, 1740-1534. doi: 10.1038/s41579-020-00470-y. URL https://www.nature.com/articles/s41579-020-00470-y.

[33] Katarzyna Potrykus and Michael Cashel. (p)ppGpp: Still Magical? *Annual Review of Microbiology*, 62(1):35–51, October 2008. ISSN 0066-4227, 1545-3251. doi: 10.1146/annurev.micro.62.081307.162903. URL https://www.annualreviews.org/doi/10.1146/annurev.micro.62.081307.162903.

[34] W. S. Yarnell and J. W. Roberts. Mechanism of Intrinsic Transcription Termination and Antitermination. *Science*, 284(5414):611–615, April 1999. ISSN 0036-8075, 1095-9203. doi: 10.1126/science.284.5414.611. URL https://www.science.org/doi/10.1126/science.284.5414.611.

[35] John P Richardson. Rho-dependent termination and ATPases in transcript termination. *Biochimica et Biophysica Acta (BBA) - Gene Structure and Expression*, 1577(2):251–260, September 2002. ISSN 01674781. doi: 10.1016/S0167-4781(02)00456-6. URL https://linkinghub.elsevier.com/retrieve/pii/S0167478102004566.

[36] Sergey Proshkin, A. Rachid Rahmouni, Alexander Mironov, and Evgeny Nudler. Cooperation Between Translating Ribosomes and RNA Polymerase in Transcription Elongation. *Science*, 328(5977):504–508, April 2010. ISSN 0036-8075, 1095-9203. doi: 10.1126/science.1184939. URL https://www.science.org/doi/10.1126/science.1184939.

[37] Björn M. Burmann, Kristian Schweimer, Xiao Luo, Markus C. Wahl, Barbara L. Stitt, Max E. Gottesman, and Paul Rösch. A NusE:NusG Complex Links Transcription and Translation. *Science*, 328(5977):501–504, April 2010. ISSN 0036-8075, 1095-9203. doi: 10.1126/science.1184953. URL `https://www.science.org/doi/10.1126/science.1184953`.

[38] Scott C. Blanchard, Barry S. Cooperman, and Daniel N. Wilson. Probing Translation with Small-Molecule Inhibitors. *Chemistry & Biology*, 17(6):633–645, June 2010. ISSN 10745521. doi: 10.1016/j.chembiol.2010.06.003. URL `https://linkinghub.elsevier.com/retrieve/pii/S1074552110002048`.

[39] Daniel N. Wilson. Ribosome-targeting antibiotics and mechanisms of bacterial resistance. *Nature Reviews Microbiology*, 12(1):35–48, January 2014. ISSN 1740-1526, 1740-1534. doi: 10.1038/nrmicro3155. URL `https://www.nature.com/articles/nrmicro3155`.

[40] J. Shine and L. Dalgarno. The 3-Terminal Sequence of *Escherichia coli* 16S Ribosomal RNA: Complementarity to Nonsense Triplets and Ribosome Binding Sites. *Proceedings of the National Academy of Sciences*, 71(4):1342–1346, April 1974. ISSN 0027-8424, 1091-6490. doi: 10.1073/pnas.71.4.1342. URL `https://pnas.org/doi/full/10.1073/pnas.71.4.1342`.

[41] Nenad Ban, Poul Nissen, Jeffrey Hansen, Peter B. Moore, and Thomas A. Steitz. The Complete Atomic Structure of the Large Ribosomal Subunit at 2.4 Å Resolution. *Science*, 289(5481):905–920, 2000. doi: 10.1126/science.289.5481.905.

[42] Xiongfeng Dai, Manlu Zhu, Mya Warren, Rohan Balakrishnan, Vadim Patsalo, Hiroyuki Okano, James R. Williamson, Kurt Fredrick, Yi-Ping Wang, and Terence Hwa. Reduction of translating ribosomes enables Escherichia coli to maintain elongation rates during slow growth. *Nature Microbiology*, 2(2):16231, December 2016. ISSN 2058-5276. doi: 10.1038/nmicrobiol.2016.231. URL `https://www.nature.com/articles/nmicrobiol2016231`.

[43] Chenhao Wu, Rohan Balakrishnan, Nathan Braniff, Matteo Mori, Gabriel Manzanarez, Zhongge Zhang, and Terence Hwa. Cellular perception of growth rate and the mechanistic origin of bacterial growth law. *Proceedings of the National Academy of Sciences*, 119(20):e2201585119, May 2022. ISSN 0027-8424, 1091-6490. doi: 10.1073/pnas.2201585119. URL `https://pnas.org/doi/full/10.1073/pnas.2201585119`.

[44] Frank Peske, Andreas Savelsbergh, Vladimir I. Katunin, Marina V. Rodnina, and Wolfgang Wintermeyer. Conformational Changes of the Small Ribosomal Subunit During Elongation Factor G-dependent tRNA–mRNA Translocation. *Journal of Molecular Biology*, 343(5):1183–1194, November 2004. ISSN 00222836. doi: 10.1016/j.jmb.2004.08.097. URL https://linkinghub.elsevier.com/retrieve/pii/S0022283604011088.

[45] Matthew Scott, Stefan Klumpp, Eduard M Mateescu, and Terence Hwa. Emergence of robust growth laws from optimal regulation of ribosome synthesis. *Molecular Systems Biology*, 10(8):MSB145379, August 2014. ISSN 1744-4292. doi: 10.15252/msb.20145379. URL https://link.springer.com/10.15252/msb.20145379.

[46] Andrea Ripamonti, Milan Lacassin, Rossana Droghetti, Gregory Bokinsky, and Marco Cosentino Lagomarsino. Transcriptional competition biases the effects of second messengers in *Escherichia coli*. *Cell Systems*, 17(6):101609, 2026. doi: 10.1016/j.cels.2026.101609.

[47] R. Kohler, R. A. Mooney, D. J. Mills, R. Landick, and P. Cramer. Architecture of a transcribing-translating expressome. *Science*, 356(6334):194–197, April 2017. ISSN 0036-8075, 1095-9203. doi: 10.1126/science.aal3059. URL https://www.science.org/doi/10.1126/science.aal3059.

[48] Chengyuan Wang, Vadim Molodtsov, Emre Firlar, Jason T. Kaelber, Gregor Blaha, Min Su, and Richard H. Ebright. Structural basis of transcription-translation coupling. *Science*, 369(6509):1359–1365, September 2020. ISSN 0036-8075, 1095-9203. doi: 10.1126/science.abb5317. URL https://www.science.org/doi/10.1126/science.abb5317.

[49] Nusrat Shahin Qureshi and Olivier Duss. Tracking transcription–translation coupling in real time. *Nature*, 637(8045):487–495, January 2025. ISSN 0028-0836, 1476-4687. doi: 10.1038/s41586-024-08308-w. URL https://www.nature.com/articles/s41586-024-08308-w.

[50] F. Ulrich Hartl, Andreas Bracher, and Manajit Hayer-Hartl. Molecular chaperones in protein folding and proteostasis. *Nature*, 475(7356):324–332, July 2011. ISSN 0028-0836, 1476-4687. doi: 10.1038/nature10317. URL https://www.nature.com/articles/nature10317.

[51] David Balchin, Manajit Hayer-Hartl, and F. Ulrich Hartl. In vivo aspects of protein folding and quality control. *Science*, 353(6294):aac4354, July 2016. doi: 10.1126/science.aac4354. URL https://www.science.org/doi/10.1126/science.aac4354.

[52] Ross E. Dalbey, Peng Wang, and Andreas Kuhn. Assembly of Bacterial Inner Membrane Proteins. *Annual Review of Biochemistry*, 80 (1):161–187, July 2011. ISSN 0066-4154, 1545-4509. doi: 10.1146/annurev-biochem-060409-092524. URL https://www.annualreviews.org/doi/10.1146/annurev-biochem-060409-092524.

[53] Evan Mercier, Xiaolin Wang, Lena A. K. Bögeholz, Wolfgang Wintermeyer, and Marina V. Rodnina. Cotranslational Biogenesis of Membrane Proteins in Bacteria. *Frontiers in Molecular Biosciences*, 9:871121, April 2022. ISSN 2296-889X. doi: 10.3389/fmolb.2022.871121. URL https://www.frontiersin.org/articles/10.3389/fmolb.2022.871121/full.

[54] Andreas Kuhn and Dorothee Kiefer. Membrane protein insertase Y id C in bacteria and archaea. *Molecular Microbiology*, 103(4):590–594, February 2017. ISSN 0950-382X, 1365-2958. doi: 10.1111/mmi.13586. URL https://onlinelibrary.wiley.com/doi/10.1111/mmi.13586.

[55] Daniel O. Daley, Mikaela Rapp, Erik Granseth, Karin Melén, David Drew, and Gunnar Von Heijne. Global Topology Analysis of the *Escherichia coli* Inner Membrane Proteome. *Science*, 308(5726):1321–1323, May 2005. ISSN 0036-8075, 1095-9203. doi: 10.1126/science.1109730. URL https://www.science.org/doi/10.1126/science.1109730.

[56] Joen Luirink, Gunnar von Heijne, Edith Houben, and Jan-Willem de Gier. Biogenesis of Inner Membrane Proteins in Escherichia coli. *Annual Review of Microbiology*, 59:329–355, 2005. doi: 10.1146/annurev.micro.59.030804.121246.

[57] John P. Overington, Bissan Al-Lazikani, and Andrew L. Hopkins. How many drug targets are there? *Nature Reviews Drug Discovery*, 5(12):993–996, December 2006. ISSN 1474-1776, 1474-1784. doi: 10.1038/nrd2199. URL https://www.nature.com/articles/nrd2199.

[58] Hiroshi Nikaido. Antibiotic Resistance Caused by Gram-Negative Multidrug Efflux Pumps. *Clinical Infectious Diseases*, 27(s1):S32–S41, August 1998. ISSN 1058-4838, 1537-6591. doi: 10.1086/514920. URL https://academic.oup.com/cid/article-lookup/doi/10.1086/514920.

[59] Samuel Wagner, Louise Baars, A. Jimmy Ytterberg, Anja Klussmeier, Claudia S. Wagner, Olof Nord, Per-Åke Nygren, Klaas J. van Wijk, and Jan-Willem de Gier. Consequences of Membrane Protein Overexpression in

Escherichia coli. *Molecular & Cellular Proteomics*, 6(9):1527–1550, 2007. doi: 10.1074/mcp.M600431-MCP200.

[60] Samuel Wagner, Mirjam M. Klepsch, Susan Schlegel, Ansgar Appel, Roger Draheim, Michael Tarry, Martin Högbom, Klaas J. Van Wijk, Dirk J. Slotboom, Jan O. Persson, and Jan-Willem De Gier. Tuning *Escherichia coli* for membrane protein overexpression. *Proceedings of the National Academy of Sciences*, 105(38):14371–14376, September 2008. ISSN 0027-8424, 1091-6490. doi: 10.1073/pnas.0804090105. URL https://pnas.org/doi/full/10.1073/pnas.0804090105.

[61] Elizabeth A. Campbell, Nataliya Korzheva, Arkady Mustaev, Katsuhiko Murakami, Satish Nair, Alex Goldfarb, and Seth A. Darst. Structural Mechanism for Rifampicin Inhibition of Bacterial RNA Polymerase. *Cell*, 104(6):901–912, March 2001. ISSN 00928674. doi: 10.1016/S0092-8674(01)00286-0. URL https://linkinghub.elsevier.com/retrieve/pii/S0092867401002860.

[62] Philip Greulich, Matthew Scott, Martin R Evans, and Rosalind J Allen. Growth-dependent bacterial susceptibility to ribosome-targeting antibiotics. *Molecular Systems Biology*, 11(3):MSB145949, March 2015. ISSN 1744-4292. doi: 10.15252/msb.20145949. URL https://link.springer.com/10.15252/msb.20145949.

[63] J. Barrett Deris, Minsu Kim, Zhongge Zhang, Hiroyuki Okano, Rutger Hermsen, Alexander Groisman, and Terence Hwa. The Innate Growth Bistability and Fitness Landscapes of Antibiotic-Resistant Bacteria. *Science*, 342(6162):1237435, November 2013. ISSN 0036-8075, 1095-9203. doi: 10.1126/science.1237435. URL https://www.science.org/doi/10.1126/science.1237435.

[64] Guido Hartmann, Karl Otto Honikel, Fritz Knüsel, and Jakob Nüesch. The specific inhibition of the DNA-directed RNA synthesis by rifamycin. *Biochimica et Biophysica Acta (BBA) - Nucleic Acids and Protein Synthesis*, 145(3):843–844, October 1967. ISSN 00052787. doi: 10.1016/0005-2787(67)90147-5. URL https://linkinghub.elsevier.com/retrieve/pii/0005278767901475.

[65] Antoni Zwiefka, Harold Kohn, and William R. Widger. Transcription termination factor rho: The site of bicyclomycin inhibition in Escherichia coli. *Biochemistry*, 32(14):3564–3570, April 1993. ISSN 0006-2960, 1520-4995. doi: 10.1021/bi00065a007. URL https://pubs.acs.org/doi/abs/10.1021/bi00065a007.

[66] Vitaly Epshtein, Dipak Dutta, Joseph Wade, and Evgeny Nudler. An allosteric mechanism of Rho-dependent transcription termination. *Nature*, 463(7278):245–249, January 2010. ISSN 0028-0836, 1476-4687. doi: 10.1038/nature08669. URL https://www.nature.com/articles/nature08669.

[67] Beth P Goldstein. Resistance to rifampicin: a review. *The Journal of Antibiotics*, 67(9):625–630, September 2014. ISSN 0021-8820, 1881-1469. doi: 10.1038/ja.2014.107. URL https://www.nature.com/articles/ja2014107.

[68] Mike Tyers and Gerard D. Wright. Drug combinations: a strategy to extend the life of antibiotics in the 21st century. *Nature Reviews Microbiology*, 17(3):141–155, March 2019. ISSN 1740-1526, 1740-1534. doi: 10.1038/s41579-018-0141-x. URL https://www.nature.com/articles/s41579-018-0141-x.

[69] Tobias Bollenbach. Antimicrobial interactions: mechanisms and implications for drug discovery and resistance evolution. *Current Opinion in Microbiology*, 27:1–9, October 2015. ISSN 13695274. doi: 10.1016/j.mib.2015.05.008. URL https://linkinghub.elsevier.com/retrieve/pii/S1369527415000594.

[70] Jinzhong Lin, Dejian Zhou, Thomas A. Steitz, Yury S. Polikanov, and Matthieu G. Gagnon. Ribosome-Targeting Antibiotics: Modes of Action, Mechanisms of Resistance, and Implications for Drug Design. *Annual Review of Biochemistry*, 87:451–478, 2018. ISSN 1545-4509. doi: 10.1146/annurev-biochem-062917-011942. URL https://www.annualreviews.org/content/journals/10.1146/annurev-biochem-062917-011942.

[71] Bor Kavčič, Gašper Tkačik, and Tobias Bollenbach. Mechanisms of drug interactions between translation-inhibiting antibiotics. *Nature Communications*, 11(1):4013, August 2020. ISSN 2041-1723. doi: 10.1038/s41467-020-17734-z. URL https://www.nature.com/articles/s41467-020-17734-z.

[72] Jack A. Dunkle, Liqun Xiong, Alexander S. Mankin, and Jamie H. D. Cate. Structures of the *Escherichia coli* ribosome with antibiotics bound near the peptidyl transferase center explain spectra of drug action. *Proceedings of the National Academy of Sciences*, 107(40):17152–17157, October 2010. ISSN 0027-8424, 1091-6490. doi: 10.1073/pnas.1007988107. URL https://pnas.org/doi/full/10.1073/pnas.1007988107.

[73] Krishna Kannan, Nora Vázquez-Laslop, and Alexander S. Mankin. Selective Protein Synthesis by Ribosomes with a Drug-Obstructed Exit Tunnel. *Cell*, 151(3):508–520, October 2012. ISSN 00928674. doi: 10.1016/

j.cell.2012.09.018. URL https://linkinghub.elsevier.com/retrieve/pii/S0092867412011257.

[74] Nora Vázquez-Laslop and Alexander S. Mankin. How Macrolide Antibiotics Work. *Trends in Biochemical Sciences*, 43(9):668–684, September 2018. ISSN 09680004. doi: 10.1016/j.tibs.2018.06.011. URL https://linkinghub.elsevier.com/retrieve/pii/S0968000418301282.

[75] Frank Schluenzen, Chie Takemoto, Daniel N Wilson, Tatsuya Kaminishi, Joerg M Harms, Kyoko Hanawa-Suetsugu, Witold Szaflarski, Masahito Kawazoe, Mikako Shirouzu, Knud H Nierhaus, Shigeyuki Yokoyama, and Paola Fucini. The antibiotic kasugamycin mimics mRNA nucleotides to destabilize tRNA binding and inhibit canonical translation initiation. *Nature Structural & Molecular Biology*, 13(10):871–878, October 2006. ISSN 1545-9993, 1545-9985. doi: 10.1038/nsmb1145. URL https://www.nature.com/articles/nsmb1145.

[76] J Davies and B D Davis. Misreading of Ribonucleic Acid Code Words Induced by Aminoglycoside Antibiotics. *Journal of Biological Chemistry*, 243(12):3312–3316, June 1968. ISSN 00219258. doi: 10.1016/S0021-9258(18)93308-9. URL https://linkinghub.elsevier.com/retrieve/pii/S0021925818933089.

[77] Thomas R. Tritton. Ribosome-tetracycline interactions. *Biochemistry*, 16(18):4133–4138, September 1977. ISSN 0006-2960, 1520-4995. doi: 10.1021/bi00637a029. URL https://pubs.acs.org/doi/abs/10.1021/bi00637a029.

[78] Robin E. Stanley, Gregor Blaha, Robert L. Grodzicki, Michael D. Strickler, and Thomas A. Steitz. The structures of the anti-tuberculosis antibiotics viomycin and capreomycin bound to the 70S ribosome. *Nature Structural & Molecular Biology*, 17(3):289–293, March 2010. ISSN 1545-9985. doi: 10.1038/nsmb.1755.

[79] Andreas Savelsbergh, Marina V. Rodnina, and Wolfgang Wintermeyer. Distinct functions of elongation factor G in ribosome recycling and translocation. *RNA*, 15(5):772–780, May 2009. ISSN 1469-9001. doi: 10.1261/rna.1592509.

[80] Roderich Roemhild, Tobias Bollenbach, and Dan I. Andersson. The physiology and genetics of bacterial responses to antibiotic combinations. *Nature Reviews Microbiology*, 20(8):478–490, August 2022. ISSN 1740-1526, 1740-1534. doi: 10.1038/s41579-022-00700-5. URL https://www.nature.com/articles/s41579-022-00700-5.

[81] Ana Rita Brochado, Anja Telzerow, Jacob Bobonis, Manuel Banzhaf, André Mateus, Joel Selkrig, Emily Huth, Stefan Bassler, Jordi Zamarreño Beas, Matylda Zietek, Natalie Ng, Sunniva Foerster, Benjamin Ezraty, Béatrice Py, Frédéric Barras, Mikhail M. Savitski, Peer Bork, Stephan Göttig, and Athanasios Typas. Species-specific activity of antibacterial drug combinations. *Nature*, 559(7713):259–263, July 2018. ISSN 0028-0836, 1476-4687. doi: 10.1038/s41586-018-0278-9. URL `https://www.nature.com/articles/s41586-018-0278-9`.

[82] Pamela Yeh, Ariane I Tschumi, and Roy Kishony. Functional classification of drugs by properties of their pairwise interactions. *Nature Genetics*, 38(4): 489–494, April 2006. ISSN 1061-4036, 1546-1718. doi: 10.1038/ng1755. URL `https://www.nature.com/articles/ng1755`.

[83] F. C. Odds. Synergy, antagonism, and what the chequerboard puts between them. *Journal of Antimicrobial Chemotherapy*, 52(1):1–1, June 2003. ISSN 1460-2091. doi: 10.1093/jac/dkg301. URL `https://academic.oup.com/jac/article-lookup/doi/10.1093/jac/dkg301`.

[84] Jean-Baptiste Michel, Pamela J. Yeh, Remy Chait, Robert C. Moellering, and Roy Kishony. Drug interactions modulate the potential for evolution of resistance. *Proceedings of the National Academy of Sciences*, 105(39): 14918–14923, September 2008. doi: 10.1073/pnas.0800944105. URL `https://www.pnas.org/doi/abs/10.1073/pnas.0800944105`.

[85] Nikos Fatsis-Kavalopoulos, Roderich Roemhild, Po-Cheng Tang, Johan Kreuger, and Dan I. Andersson. CombiANT: Antibiotic interaction testing made easy. *PLOS Biology*, 18(9):e3000856, September 2020. ISSN 1545-7885. doi: 10.1371/journal.pbio.3000856. URL `https://dx.plos.org/10.1371/journal.pbio.3000856`.

[86] Tobias Bollenbach, Selwyn Quan, Remy Chait, and Roy Kishony. Nonoptimal Microbial Response to Antibiotics Underlies Suppressive Drug Interactions. *Cell*, 139(4):707–718, November 2009. ISSN 00928674. doi: 10.1016/j.cell.2009.10.025. URL `https://linkinghub.elsevier.com/retrieve/pii/S0092867409013154`.

[87] S. Loewe. Die quantitativen Probleme der Pharmakologie. *Ergebnisse der Physiologie*, 27(1):47–187, December 1928. ISSN 0303-4240, 1617-5786. doi: 10.1007/BF02322290. URL `http://link.springer.com/10.1007/BF02322290`.

[88] Bor Kavčič, Gašper Tkačik, and Tobias Bollenbach. Minimal biophysical model of combined antibiotic action. *PLOS Computational Biology*, 17(1): e1008529, January 2021. ISSN 1553-7358. doi: 10.1371/journal.pcbi.1008529. URL https://dx.plos.org/10.1371/journal.pcbi.1008529.

[89] Manlu Zhu, Matteo Mori, Terence Hwa, and Xiongfeng Dai. Distantly related bacteria share a rigid proteome allocation strategy with flexible enzyme kinetics. *Proceedings of the National Academy of Sciences*, 122(18): e2427091122, May 2025. ISSN 0027-8424, 1091-6490. doi: 10.1073/pnas.2427091122. URL https://pnas.org/doi/10.1073/pnas.2427091122.

[90] Ryan Thiermann, Jin Yang, Aniket Zodage, Fukang She, Danny K. Fung, Taylor Rytlewski, Farshad Abdollah-Nia, Fangzhou Xiao, John T. Sauls, Sarah Cox, Zulfar Ghulam-Jelani, Victoria Castillo, Quinn A. Paulsen, David M. Stevenson, Daniel Amador-Noguez, James R. Williamson, Jue D. Wang, and Suckjoon Jun. Decoupling of global metabolic flux and proteome partitioning in bacteria. *Science*, 392(6804):eaeb6410, June 2026. ISSN 0036-8075, 1095-9203. doi: 10.1126/science.aeb6410. URL https://www.science.org/doi/10.1126/science.aeb6410.

[91] Markus Basan, Sheng Hui, Hiroyuki Okano, Zhongge Zhang, Yang Shen, James R. Williamson, and Terence Hwa. Overflow metabolism in Escherichia coli results from efficient proteome allocation. *Nature*, 528(7580):99–104, December 2015. ISSN 0028-0836, 1476-4687. doi: 10.1038/nature15765. URL https://www.nature.com/articles/nature15765.

[92] Frederick C. Neidhardt and Boris Magasanik. Studies on the role of ribonucleic acid in the growth of bacteria. *Biochimica et Biophysica Acta*, 42:99–116, January 1960. ISSN 00063002. doi: 10.1016/0006-3002(60)90757-5. URL https://linkinghub.elsevier.com/retrieve/pii/0006300260907575.

[93] Julia Hughes and Graham Mellows. Inhibition of Isoleucyl-Transfer Ribonucleic Acid Synthetase in Escherichia coli by Pseudomonic Acid. *Biochemical Journal*, 176(1):305–318, 1978. doi: 10.1042/bj1760305.

[94] Daniel S. Eaton, Carlos Sánchez, Luis Gutiérrez-López, Jacob Q. Shenker, Youlian Goulev, Brianna R. Watson, Véronique Henriot, Ethan C. Garner, Quincey A. Justman, Jeffrey R. Moffitt, and Johan Paulsson. Essentialome-Wide Multigenerational Imaging Reveals Mechanistic Origins of Cell Growth Laws, June 2025. URL http://biorxiv.org/lookup/doi/10.1101/2025.06.10.658525.

[95] Natawan Gadjisade, Matteo Mori, and Tobias Bollenbach. A generalized growth law for translation- and transcription-targeting antibiotics captures drug interactions. *bioRxiv*, 2026. doi: 10.64898/2026.08.21.746212.

[96] Johan Elf, Karin Nilsson, Tanel Tenson, and Måns Ehrenberg. Bistable Bacterial Growth Rate in Response to Antibiotics with Low Membrane Permeability. *Physical Review Letters*, 97(25):258104, December 2006. ISSN 0031-9007, 1079-7114. doi: 10.1103/PhysRevLett.97.258104. URL `https://link.aps.org/doi/10.1103/PhysRevLett.97.258104`.

[97] Emiko Y. Rosenberg, Dzwokai Ma, and Hiroshi Nikaido. AcrD of Escherichia coli Is an Aminoglycoside Efflux Pump. *Journal of Bacteriology*, 182(6):1754–1756, March 2000. ISSN 0021-9193. doi: 10.1128/jb.182.6.1754-1756.2000. URL `https://pmc.ncbi.nlm.nih.gov/articles/PMC94475/`.

[98] Yuichi Taniguchi, Paul J. Choi, Gene-Wei Li, Huiyi Chen, Mohan Babu, Jeremy Hearn, Andrew Emili, and X. Sunney Xie. Quantifying *E. coli* Proteome and Transcriptome with Single-Molecule Sensitivity in Single Cells. *Science*, 329(5991):533–538, July 2010. ISSN 0036-8075, 1095-9203. doi: 10.1126/science.1188308. URL `https://www.science.org/doi/10.1126/science.1188308`.

[99] Christine Vogel and Edward M. Marcotte. Insights into the regulation of protein abundance from proteomic and transcriptomic analyses. *Nature Reviews Genetics*, 13(4):227–232, April 2012. ISSN 1471-0056, 1471-0064. doi: 10.1038/nrg3185. URL `https://www.nature.com/articles/nrg3185`.

[100] Yansheng Liu, Andreas Beyer, and Ruedi Aebersold. On the Dependency of Cellular Protein Levels on mRNA Abundance. *Cell*, 165(3):535–550, April 2016. ISSN 00928674. doi: 10.1016/j.cell.2016.03.014. URL `https://linkinghub.elsevier.com/retrieve/pii/S0092867416302707`.

[101] Orawan Borirak, Matthew D. Rolfe, Leo J. de Koning, Huub C. J. Hoefsloot, Martijn Bekker, Henk L. Dekker, Winfried Roseboom, Jeffrey Green, Chris G. de Koster, and Klaas J. Hellingwerf. Time-series analysis of the transcriptome and proteome of *Escherichia coli* upon glucose repression. *Biochimica et Biophysica Acta (BBA) - Proteins and Proteomics*, 1854(10, Part A):1269–1279, October 2015. ISSN 1570-9639. doi: 10.1016/j.bbapap.2015.05.017. URL `https://www.sciencedirect.com/science/article/pii/S157096391500165X`.

[102] Ido Golding, Johan Paulsson, Scott M. Zawilski, and Edward C. Cox. Real-time kinetics of gene activity in individual bacteria. *Cell*, 123(6):1025–1036, December 2005. ISSN 0092-8674. doi: 10.1016/j.cell.2005.09.031.

[103] S. Kalir, J. McClure, K. Pabbaraju, C. Southward, M. Ronen, S. Leibler, M. G. Surette, and U. Alon. Ordering Genes in a Flagella Pathway by Analysis of Expression Kinetics from Living Bacteria. *Science*, 292(5524):2080–2083, June 2001. ISSN 0036-8075, 1095-9203. doi: 10.1126/science.1058758. URL `https://www.science.org/doi/10.1126/science.1058758`.

[104] Michal Ronen, Revital Rosenberg, Boris I. Shraiman, and Uri Alon. Assigning numbers to the arrows: Parameterizing a gene regulation network by using accurate expression kinetics. *Proceedings of the National Academy of Sciences of the United States of America*, 99(16):10555–10560, August 2002. ISSN 0027-8424. doi: 10.1073/pnas.152046799. URL `https://pmc.ncbi.nlm.nih.gov/articles/PMC124972/`.

[105] Alon Zaslaver, Shai Kaplan, Anat Bren, Adrian Jinich, Avi Mayo, Erez Dekel, Uri Alon, and Shalev Itzkovitz. Invariant Distribution of Promoter Activities in Escherichia coli. *PLoS Computational Biology*, 5(10):e1000545, October 2009. ISSN 1553-7358. doi: 10.1371/journal.pcbi.1000545. URL `https://dx.plos.org/10.1371/journal.pcbi.1000545`.

[106] Leeat Keren, Ora Zackay, Maya Lotan-Pompan, Uri Barenholz, Erez Dekel, Vered Sasson, Guy Aidelberg, Anat Bren, Danny Zeevi, Adina Weinberger, Uri Alon, Ron Milo, and Eran Segal. Promoters maintain their relative activity levels under different growth conditions. *Molecular Systems Biology*, 9(1):MSB201359, October 2013. ISSN 1744-4292. doi: 10.1038/msb.2013.59. URL `https://doi.org/10.1038/msb.2013.59`.

[107] François Jacob and Jacques Monod. Genetic regulatory mechanisms in the synthesis of proteins. *Journal of Molecular Biology*, 3(3):318–356, 1961. doi: 10.1016/S0022-2836(61)80072-7.

[108] Alon Zaslaver, Anat Bren, Michal Ronen, Shalev Itzkovitz, Ilya Kikoin, Seagull Shavit, Wolfram Liebermeister, Michael G Surette, and Uri Alon. A comprehensive library of fluorescent transcriptional reporters for Escherichia coli. *Nature Methods*, 3(8):623–628, August 2006. ISSN 1548-7091, 1548-7105. doi: 10.1038/nmeth895. URL `https://www.nature.com/articles/nmeth895`.

[109] Dong-Eun Chang, Darren J. Smalley, and Tyrrell Conway. Gene expression profiling of Escherichia coli growth transitions: an expanded stringent response model. *Molecular Microbiology*, 45(2):289–306, 2002. ISSN 1365-2958. doi: 10.1046/j.1365-2958.2002.03001.x. URL `https://onlinelibrary.wiley.com/doi/abs/10.1046/j.1365-2958.2002.03001.x`.

[110] Matthew F. Traxler, Dong-Eun Chang, and Tyrrell Conway. Guanosine 3',5'-bispyrophosphate coordinates global gene expression during glucose-lactose diauxie in Escherichia coli. *Proceedings of the National Academy of Sciences of the United States of America*, 103(7):2374–2379, February 2006. ISSN 0027-8424. doi: 10.1073/pnas.0510995103.

[111] Ekaterina Mostovenko, André M Deelder, and Magnus Palmblad. Protein expression dynamics during Escherichia Coli glucose-lactose diauxie. *BMC Microbiology*, 11:126, June 2011. ISSN 1471-2180. doi: 10.1186/1471-2180-11-126. URL `https://pmc.ncbi.nlm.nih.gov/articles/PMC3121593/`.

[112] S. Mangan, S. Itzkovitz, A. Zaslaver, and U. Alon. The Incoherent Feed-forward Loop Accelerates the Response-time of the gal System of Escherichia coli. *Journal of Molecular Biology*, 356(5):1073–1081, March 2006. ISSN 00222836. doi: 10.1016/j.jmb.2005.12.003. URL `https://linkinghub.elsevier.com/retrieve/pii/S0022283605015573`.

[113] Ingrid M. Keseler, Amanda Mackie, Alberto Santos-Zavaleta, Richard Billington, César Bonavides-Martínez, Ron Caspi, Carol Fulcher, Socorro Gama-Castro, Anamika Kothari, Markus Krummenacker, Mario Latendresse, Luis Muñiz-Rascado, Quang Ong, Suzanne Paley, Martin Peralta-Gil, Pallavi Subhraveti, David A. Velázquez-Ramírez, Daniel Weaver, Julio Collado-Vides, Ian Paulsen, and Peter D. Karp. The EcoCyc database: reflecting new knowledge about *Escherichia coli* K-12. *Nucleic Acids Research*, 45(D1):D543–D550, January 2017. ISSN 0305-1048, 1362-4962. doi: 10.1093/nar/gkw1003. URL `https://academic.oup.com/nar/article-lookup/doi/10.1093/nar/gkw1003`.

[114] Sudha Nair and Steven E. Finkel. Dps Protects Cells against Multiple Stresses during Stationary Phase. *Journal of Bacteriology*, 186(13):4192–4198, July 2004. ISSN 0021-9193, 1098-5530. doi: 10.1128/JB.186.13.4192-4198.2004. URL `https://journals.asm.org/doi/10.1128/JB.186.13.4192-4198.2004`.

[115] Johan H. J. Leveau and Steven E. Lindow. Predictive and Interpretive Simulation of Green Fluorescent Protein Expression in Reporter Bacteria. *Journal of Bacteriology*, 183(23):6752–6762, December 2001. ISSN 0021-9193, 1098-5530. doi: 10.1128/JB.183.23.6752-6762.2001. URL `https://journals.asm.org/doi/10.1128/JB.183.23.6752-6762.2001`.

[116] Enrique Balleza, J Mark Kim, and Philippe Cluzel. Systematic characterization of maturation time of fluorescent proteins in living cells. *Nature*

Methods, 15(1):47–51, January 2018. ISSN 1548-7091, 1548-7105. doi: 10.1038/nmeth.4509. URL https://www.nature.com/articles/nmeth.4509.

[117] Alexander Schmidt, Karl Kochanowski, Silke Vedelaar, Erik Ahrné, Benjamin Volkmer, Luciano Callipo, Kèvin Knoops, Manuel Bauer, Ruedi Aebersold, and Matthias Heinemann. The quantitative and condition-dependent Escherichia coli proteome. *Nature Biotechnology*, 34(1):104–110, January 2016. ISSN 1087-0156, 1546-1696. doi: 10.1038/nbt.3418. URL https://www.nature.com/articles/nbt.3418.

[118] Nobuyuki Otsu. A Threshold Selection Method from Gray-Level Histograms. *IEEE Transactions on Systems, Man, and Cybernetics*, 9(1):62–66, January 1979. ISSN 0018-9472, 2168-2909. doi: 10.1109/TSMC.1979.4310076. URL http://ieeexplore.ieee.org/document/4310076/.

[119] Janina Müller, Natawan Gadjisade, S. Andreas Angermayr, Gerrit Ansmann, and Tobias Bollenbach. Ultrasensitive fitness costs arise from membrane proteome displacement under protein overexpression. *Cell Systems*, 17(10): 101709, 2026. doi: 10.1016/j.cels.2026.101709.

[120] Katarzyna Potrykus, Helen Murphy, Nadège Philippe, and Michael Cashel. ppGpp is the major source of growth rate control in *E. coli*. *Environmental Microbiology*, 13(3):563–575, March 2011. ISSN 1462-2912, 1462-2920. doi: 10.1111/j.1462-2920.2010.02357.x. URL https://sfamjournals.onlinelibrary.wiley.com/doi/10.1111/j.1462-2920.2010.02357.x.

[121] Benjamin Volkmer and Matthias Heinemann. Condition-Dependent Cell Volume and Concentration of Escherichia coli to Facilitate Data Conversion for Systems Biology Modeling. *PLoS ONE*, 6(7):e23126, July 2011. ISSN 1932-6203. doi: 10.1371/journal.pone.0023126. URL https://pmc.ncbi.nlm.nih.gov/articles/PMC3146540/.

[122] Markus Basan, Manlu Zhu, Xiongfeng Dai, Mya Warren, Daniel Sévin, Yi-Ping Wang, and Terence Hwa. Inflating bacterial cells by increased protein synthesis. *Molecular Systems Biology*, 11(10):MSB156178, October 2015. ISSN 1744-4292. doi: 10.15252/msb.20156178. URL https://link.springer.com/10.15252/msb.20156178.

[123] Stephen Vadia, Jessica L. Tse, Rafael Lucena, Zhizhou Yang, Douglas R. Kellogg, Jue D. Wang, and Petra Anne Levin. Fatty Acid Availability Sets Cell Envelope Capacity and Dictates Microbial Cell Size. *Current Biology*, 27(12):1757–1767.e5, June 2017. ISSN 09609822. doi: 10.1016/

j.cub.2017.05.076. URL https://linkinghub.elsevier.com/retrieve/pii/S0960982217306425.

[124] Adrien Ducret, Ellen M. Quardokus, and Yves V. Brun. MicrobeJ, a tool for high throughput bacterial cell detection and quantitative analysis. *Nature microbiology*, 1(7):16077, June 2016. ISSN 2058-5276. doi: 10.1038/nmicrobiol.2016.77. URL https://pmc.ncbi.nlm.nih.gov/articles/PMC5010025/.

[125] Kevin J. Cutler, Carsen Stringer, Teresa W. Lo, Luca Rappez, Nicholas Stroustrup, S. Brook Peterson, Paul A. Wiggins, and Joseph D. Mougous. Omnipose: a high-precision morphology-independent solution for bacterial cell segmentation. *Nature Methods*, 19(11):1438–1448, November 2022. ISSN 1548-7105. doi: 10.1038/s41592-022-01639-4. URL https://www.nature.com/articles/s41592-022-01639-4.

[126] Tobias Bollenbach and Roy Kishony. Resolution of Gene Regulatory Conflicts Caused by Combinations of Antibiotics. *Molecular Cell*, 42(4):413–425, May 2011. ISSN 10972765. doi: 10.1016/j.molcel.2011.04.016. URL https://linkinghub.elsevier.com/retrieve/pii/S1097276511003200.

[127] L Radlinski and BP Conlon. Antibiotic efficacy in the complex infection environment. *Current opinion in microbiology*, 42:19–24, April 2018. ISSN 1369-5274. doi: 10.1016/j.mib.2017.09.007. URL https://pmc.ncbi.nlm.nih.gov/articles/PMC5889345/.

[128] Kathleen P. Davis. Critical role of growth medium for detecting drug interactions in Gram-negative bacteria that model in vivo responses. URL https://journals.asm.org/doi/epub/10.1128/mbio.00159-24.

[129] Nikos Fatsis-Kavalopoulos, Lex Roelofs, and Dan I. Andersson. Potential risks of treating bacterial infections with a combination of -lactam and aminoglycoside antibiotics: A systematic quantification of antibiotic interactions in E. coli blood stream infection isolates. *EBioMedicine*, 78:103979, April 2022. ISSN 2352-3964. doi: 10.1016/j.ebiom.2022.103979.

[130] Kathleen Davis, Talia Greenstein, Roberto Viau Colindres, and Bree B. Aldridge. Leveraging Laboratory and Clinical Studies to Design Effective Antibiotic Combination Therapy. *Current opinion in microbiology*, 64:68–75, December 2021. ISSN 1369-5274. doi: 10.1016/j.mib.2021.09.006. URL https://pmc.ncbi.nlm.nih.gov/articles/PMC8671129/.

[131] Rohan Balakrishnan, Roshali T. de Silva, Terence Hwa, and Jonas Cremer. Suboptimal resource allocation in changing environments constrains response

and growth in bacteria. *Molecular Systems Biology*, 17(12):MSB202110597, December 2021. ISSN 1744-4292. doi: 10.15252/msb.202110597. URL https://doi.org/10.15252/msb.202110597.

[132] Francesca Gubellini, Grégory Verdon, Nathan K. Karpowich, Jon D. Luff, Grégory Boël, Nils Gauthier, Samuel K. Handelman, Sarah E. Ades, and John F. Hunt. Physiological Response to Membrane Protein Overexpression in E. coli. *Molecular & Cellular Proteomics : MCP*, 10(10):M111.007930, October 2011. ISSN 1535-9476. doi: 10.1074/mcp.M111.007930. URL https://pmc.ncbi.nlm.nih.gov/articles/PMC3205863/.

[133] Christoph B. Messner, Vadim Demichev, Nic Bloomfield, Jason S. L. Yu, Matthew White, Marco Kreidl, Anna-Sophia Egger, Anja Freiwald, Gordana Ivosev, Fras Wasim, Aleksej Zelezniak, Linda Jürgens, Norbert Suttorp, Leif Erik Sander, Florian Kurth, Kathryn S. Lilley, Michael Mülleder, Stephen Tate, and Markus Ralser. Ultra-fast proteomics with Scanning SWATH. *Nature biotechnology*, 39(7):846–854, July 2021. ISSN 1087-0156. doi: 10.1038/s41587-021-00860-4. URL https://pmc.ncbi.nlm.nih.gov/articles/PMC7611254/.